CHARACTERIZATION OF DEFORMATION DEFECTS IN METALLIC GLASSES AND METALLIC GLASS COMPOSITES: FROM EXPERIMENT TO COMPUTER MODELING

SHEN YING

Ph.D

The Hong Kong Polytechnic University

2013

The Hong Kong Polytechnic University

Department of Mechanical Engineering

CHARACTERIZATION OF DEFORMATION DEFECTS IN METALLIC GLASSES AND METALLIC GLASS COMPOSITES: FROM EXPERIMENT TO COMPUTER MODELING

Shen Ying

A thesis submitted in partial fulfillment of the requirements for the
degree of Doctor of Philosophy
March 2012

CERTIFICATE OF ORIGINALITY

I hereby declare that this thesis is my own work and that, to the best of my knowledge and belief, it reproduces no material previously published or written, nor material that has been accepted for the award of any other degree or diploma, except where due acknowledgement has been made in the text.

___________________________________ (Signed)

_____________SHEN Ying___________(Name of student)

Abstract

With its excellent mechanical properties, metallic glass has great potential to be used as structural materials for engineering application. However, shear deformation confined in the localized narrow shear zones in bulk metallic glasses (BMGs) always leads to catastrophic failure, which results in little overall plasticity and low ductility and limits their further engineering applications in a broad area. To overcome this drawback, it is necessary to deeply understand the deformation mechanism in these amorphous alloys. However, because of the difficulty of direct characterization of fundamental deformation units, the defects, and their responses to shear deformation in the metallic glass, the deformation mechanisms in BMGs are not fully understood yet.

To deeply interpret the deformation mechanisms in metallic glasses, it is necessary to understand the internal atomic structures of defects and their properties under thermal or/and mechanical stimulation. In metallic glasses, atoms are disorderly organized to form an amorphous structure without crystalline lattices. Due to the rapid quenching from liquid state, structural heterogeneity would be inevitably introduced into the amorphous matrix. Some local atomic units can be weaker or sparser than their surrounding matrix, which can be considered as defects in metallic glasses.

As loose atomic units, the defects can be the sources for atomic rearrangements under thermal stimulation. We focus on the characterization of as-synthesized defects generated from rapid quenching and on their roles in structural relaxation. We use

dynamic mechanical analysis (DMA) to measure the internal friction Q^{-1} of metallic glass, which is scaled as $Q^{-1} \sim \omega^{-n}$, where ω is the testing frequency. The reversible and irreversible structural relaxations in metallic glass are characterized, through the index n. It is found a maximum index n is associated with reversible β relaxation, and the index n at glass transition temperature is a universal value of around 0.25-0.28. Chemical short range ordering (CSRO) and topological short range ordering (TSRO) are used to interpret such scaling.

We then characterize the defects which response to shear deformation and define them as deformation defects. Based on our experimental studies, annihilation or creation of the deformation defects is found to be a process of first-order structural transition. The activation energy E_f for such transition and the surface energy of these defects are characterized. Besides, important parameters such as the size of the deformation defects and activation energy for plastic flow are also obtained, which are all crucial parameters for computational modeling of shear banding in metallic glass. Evidences from the experiments show that local plastic deformation of metallic glasses is associated with the structural change of deformation defects, which is a first-order phase transformation.

Based on the experimental study, phase field modeling with the parameters obtained from internal friction studies is applied to characterize the macroscopic mechanical properties of the metallic glasses and their composites. Systematic study on the shear banding, crack initiation and propagation in BMGs and fiber-reinforced BMG composites is carried out with phase field modeling. The fracture toughness and the modes of failure obtained from the simulation are consistent with experiments, suggesting the successful application of the phase-field approach on the understanding of shear banding and fracture processes in BMGs and BMG composites. The enhanced fracture toughness of the composite is found to relate with the bonding conditions between the BMG and the reinforcements and shear band can be initialized from their interface, and the relationship is quantitatively determined in the phase field modeling.

From the simulation study it is found that secondary shear band can be generated from the integration of two attracting shear bands. What we observe from the modeling of shear band multiplication and the generation of secondary shear bands is remarkable for the enhancement of the plasticity and fracture toughness of the BMG composites. The mechanical properties of BMGs and BMG composites are thus successfully connected with the characteristics of microscopic deformation defects.

List of Publications

1. G. P. Zheng and **Y. Shen**, Simulation of shear banding and crack propagation in bulk metallic glass matrix composites, *Journal of Alloys and Compounds*, Vol.509S (2011) S136-S140
2. **Y. Shen**, X.C. Zheng and G. P. Zheng, Mechanical Properties and Crystallization Behaviors of Microstructured Co-Fe-P Amorphous Alloys, *Metallurgical and Materials Transactions A* , Vol.42 (2011) 211-218
3. G. P. Zheng and **Y. Shen**, Multi-scale modeling of shear banding in iron-based metallic glasses, *Journal of Alloys and Compounds*, Vol.504 (2010) S56-S59
4. **Y. Shen** and G. P. Zheng, Modeling of shear band multiplication and interaction in metallic glass matrix composites, *Scripta Materialia*, Vol.63 (2010) 181-184
5. G. P. Zheng and **Y. Shen**, Simulation of crack propagation in fiber-reinforced bulk metallic glasses, *International Journal of Solids and Structures*, Vol.47 (2010) 320-329

Acknowledgement

I would like to express my sincere gratitude to my supervisor Dr. Guangping Zheng, who supported and encouraged me to search for knowledge and understanding in my four-year PhD studies.

I am also like to give my great thanks to Mr. Yeung in the Materials Research Center of the Hong Kong Polytechnic University, Dr. Qing Wang from Shanghai University, Prof. Yang Bai from University of Science and Technology Beijing, and Dr. Ye Jianchao from Lawrence Livermore National Laboratory, who have helped me on my research road.

Finally, I would like to thank my great families and all my best friends for the tremendous support and encouragement during four-year PhD studies. Without you, the journey here would have been more difficult and less rewarding.

Table of Contents

List of tables

List of figures

1. Introduction

1.1 Metallic glass

The first metallic glass, Au-Si amorphous alloy, was discovered in 1959 by Klement *et al.* (Klement, Willens et al. 1960) using splat quenching. Metallic glass is different from crystalline metals since its atoms are disorderly organized to form an amorphous structure due to rapid quenching from liquid metal. Because there are no crystalline lattices in the metallic glass, grains and grain boundaries do not exist in metallic glass. For the crystalline metals, sizes of grain and features of grain boundary determine their mechanical properties; and these properties would be highly improved by refining the grains. As ultimate grain refinement is done, crystalline lattices would disappear and amorphous matrix will be kept in the metallic material, then metallic glass is formed. The difference between mechanical properties of metallic glasses and crystalline metals could be just due to the disappear of crystalline lattices, or disappear of atomic long range order.

Through rapid quenching, typically with a rate of 10^5-10^6 K/s (Klement, Willens et al. 1960), geometry of metallic glass is restricted to ribbons in the early age, since the cooling rate roughly scales with the inverse square of sample thickness (dT/dt = thickness^{-2}) (Xu, Lohwongwatana et al. 2004). However, researchers have never stopped to search metal glasses with different components which would possibly reduce the critical cooling rate required for glass forming, or to create bulk metallic glasses with desirable size to the largest possible extent. Thus, glass forming ability (GFA) of metallic glass is of great important.

1.2 Glass forming ability

As mentioned above, quenching from the melting temperature (T_m) to a temperature below the glass transition temperature (T_g) in considerable speed, alloys would avoid crystallization and nucleation and they will be frozen as metallic glasses. Glass forming ability is a very crucial factor related the origins of glass formation and fundamentally important for designing new BMGs (Lu and Liu 2002). Normally, this factor is evaluated by critical cooling rate (R_c), which is the minimum cooling rate required to prevent crystal nucleation and growth and keep the alloy in amorphous nature (Sheng 2005). As extremely high cooling rate is required for metallic glass forming without crystallization, the sample size is highly restricted. Therefore, in order to create metallic glass in larger size, some factors should be carefully controlled, for example, atomic size mismatch (Lu, Liu et al. 2004). This compositional complexity can introduce barriers to hinder the rearrangement of different atoms into long-ordered crystalline phase and keep the alloy in a disordered glassy state. With this approach, the critical cooling rate for obtaining glassy sample would decrease to a practical level, leading to possibility of fabricating BMG in large size.

The first piece of BMG, Pd-Au-Si alloy, was created by Chen and Turnbull (Chen and Turnbull 1969) in 1969, and the thickness of the sample is around 1 mm. Since then, numerous types of BMGs with good GFA have been found. (1) Mg-based BMG. Inoue and Masumoto *et al.* (Inoue, Nakamura et al. 1992) reported $Mg_{65}Cu_{25}Y_{10}$ with good GFA to form BMG with size ranging from 1 to 7 mm. More recently, $Mg_{65}Cu_{7.5}Ni_{7.5}Ag_{5}Zn_{5}Y_{5}Gd_{5}$ BMG with significantly improved diameter of 14 mm was reported (Park, Kyeong et al. 2007). (2) Pd-based BMG. Nishiyama and Inoue reported that $Pd_{40}Cu_{30}Ni_{10}P_{20}$ exhibits very low critical cooling rate R_c~0.1 K/s which makes the sample's size as large as 72 mm (Nishiyama and Inoue 1997). Furthermore, they found that it is possible to make $Pd_{30}Pt_{17.5}Cu_{32.5}P_{20}$ BMGs with size of 50 mm, and its critical cooling rate for glass formation can reach 0.050-0.067 K/s (Nishiyama, Takenaka et al. 2006). (3) Zr-based BMG. For $Zr_{41.2}Ti_{13.8}Cu1_{2.5}Ni_{10}Be_{22.5}$, also known as Vitreloy 1, a cooling rate of 1.4 K/s could make its size to be as large as 25 mm (Waniuk, Schroers et al. 2001; Waniuk, Schroers et al. 2003). (4) Ti-based BMG. Park and Kim reported 10 mm $Ti_{40}Zr_{21}Cu_{10}Ni_{9}Be_{20}$ BMG can be fabricated with Cu-mold injection casting method (Park and Kim 2005). (5) Fe-based BMG. Because the high cooling rate is required, some Fe-based metallic glass is in the shape of ribbon or foil, like widely used Fe-Si-B in the transformer. However, large size Fe-based BMG is able to be fabricated by carefully adjusting the components. It was found by Ponnambalam *et al.* (Ponnambalam, Poon et al. 2004) that the maximum diameter of Fe–Cr–Mo–(Y/Ln)– C–B BMG can reach 12 mm by casting. During the past decades advance has also been made in fabricating bulk glassy alloys including Pt- (Schroers and Johnson 2004), Cu- (Zhang, Zhang et al. 2003) and Au-based (Schroers, Lohwongwatana et al. 2005) metallic glasses.

1.3 Mechanical properties

1.3.1 Strength

The mechanical strength τ_Y of metallic glasses can be more than 1.5 GPa. Even 5 GPa can be achieved for some BMGs under compression. Although large elastic strain of 2% can be reached, there is nearly no macroscopic plastic strain for most BMGs under tension.

The theoretical shear strength τ_Y for dislocation in crystals can be expressed as $\tau_Y \approx G/5$, where G is the shear modulus (Kelly and Macmillan 1986). But for metallic glasses, yielding stress $\sigma_Y = 0.02E$ are observed in experiment, where E is the Young's Modulus (Lu and Ravichandran 2003). By examining elastic constants and compressive yield strength of 30 metallic glasses in room temperature, Johnson and Samwer summarized an average shear limit $\gamma_c = 0.0267 \pm 0.0020$, where $\tau_c = \gamma_c G$ is the maximum resolved shear stress at yielding of the unstressed glass (Johnson and Samwer 2005). For individual metallic glass, the shear stress limit depends on T/T_g:

$$\tau_c(T) = G\left[\gamma_{c0} - \gamma_{c1}\left(\frac{T}{T_g}\right)^{2/3}\right], \tag{1.1}$$

where γ_{c0} and γ_{c1} are fitting constants, which are approximately universal constants with the values of 0.036 $\pm$0.002 and 0.016 $\pm$0.002, respectively.

Recently Liu *et al*. (Liu, Liu et al. 2009) suggested the relationship of the yield strength τ_c with the glass transition temperature T_g and molar volume V of metallic glass as:

$$\tau_y = 3R\frac{(T_g - RT)}{\gamma_0 V}, \tag{1.2}$$

where R is the gas constant, T is room temperature, γ_0 is the critical local shear strain leading to destabilization of local shearing events. They believed the linearity between yield strength and glass transition temperature unambiguously indicates that the elastic destabilization of metallic glasses driven by external forces is equivalent to the glass transition induced by thermal energy. It is the local geometrical frustrations and defects in the disordered solids that govern the strength of BMGs.

1.3.2 Fracture behavior

Fracture toughness is a property which describes the ability of a material to resist fracture, and is one of the most important properties of material for structural applications. This value is determined by the intrinsic energy management mechanisms available to release stress concentrations at crack tips. Material is brittle if strain energy concentrated in a small region ahead of the crack tip; on the contrary, material is tough if it has the ability to dissipate the energy through various processes. Most of metallic glasses are brittle due to its strain softening and lacking of barriers for intrinsic crack propagation. The high stress concentration at crack tips leads to quick and catastrophe failure of metallic glasses. The low fracture toughness prevents the amorphous alloys to be applied as structural materials. Besides, any structural change of metallic glasses, *e.g.* relaxation, would affect its toughness greatly, which introduces uncertainty for their practical application. Therefore, the fracture behavior of metallic glasses is a critical issue. The discovery of alloys with larger GFA makes it possible to form bulk metallic glasses in a larger size rather than films and foils, which enables the fracture behaviors to be measured (Peker and Johnson 1993).

During the fracture, significant energy would be released, which heats up the fracture surface, making the material surface fluid-like. Due to the inhomogeneous flow, the morphology of fracture surface exhibits large vein patterns for ductile fracture and small and fine vein patterns for brittle fracture in metallic glasses. Xi *et al*. (Xi, Zhao et al. 2005) indicated that plastic zone size r_p, which is related with fracture toughness K_C, can be measured from the fracture surface, and their relations can be described as:

$$r_P = \frac{1}{6\pi}\left(\frac{K_C}{\sigma_y}\right)^2, \qquad (1.3)$$

where σ_y is the yield strength. The plane strain fracture energy Q_c, as a function of plastic zone size for a variety of metallic glasses can be expressed as:

$$Q_c = \frac{K_c^2}{E(1-v)^2}, \tag{1.4}$$

where E is the Young's modulus, v is the Poisson's ratio. Xi *et al.* concluded that fracture toughness of metallic glasses does not only depend on plastic zone size, but also depend on the micromechanism of fracture. While recent discovery by Raghavan *et al.* (Raghavan, Murali et al. 2006) suggested that toughness is a parameter which is sensitive to free-volume content in the metallic glasses: toughness decreases proportionally with free volumes. Similar results were reported by other researchers, indicating that toughness decreases after annealing which induces structural relaxation (Murali and Ramamurty 2005).

Gilbert *et al.* (Gilbert, Ritchie et al. 1997) found that BMG $Zr_{41.2}Ti_{13.8}Cu_{12.5}Ni_{10}Be_{22.5}$ has the fracture toughness of K_{IC} = 55 MPa m$^{1/2}$, which is comparable with that of a high-strength steel or aluminum alloy. However, partial or full crystallization, *e.g.,* through annealing exposure at 633 K or above, was found to result in more than 50 times' reduction in fracture toughness, which is comparable with silica glass. However Lowhaphandu and Lewandowski (Lowhaphandu and Lewandowski 1998) reported a much lower K_{IC} = 19 MPa m$^{1/2}$ in fatigue pre-cracked specimens, which indicates toughness value measured is highly sensitive to the notch root radius where plastic deformation (shear banding) and crack branching happen. Schroers and Johnson (Schroers and Johnson 2004) reported $Pt_{57.5}Cu_{14.7}Ni_{5.3}P_{22.5}$ bulk metallic glass has very high fracture toughness, approximately 80 MPa $m^{1/2}$. They suggested that the large plasticity is indicated by a high Poisson ratio of 0.42, which promotes multiple shear bands formation and extension instead of crack propagation.

1.3.3 Ductility

Lacking of work-hardening, most metallic glasses are brittle and show little significant macroscopic ductility. In metallic glasses, plastic deformation locates in the narrow shear bands where shear strain can be more than 100%. It is believed that in shear band there is a critical shear displacement Δu^* which distinguishes the fracture initiations in metallic glasses, and its value depends on the components and structures of the alloy as well as the loading conditions. Δu^* is tens of microns (Ravichandran and Molinari 2005). Plastic strain in shear band would grow rapidly as shear band propagates without any constrain. Therefore monolithic metallic glasses seldom show global ductility, especially they are deformed in tension. For searching of metallic glasses with remarkable ductility, one of the possible methods is to restrain the shear displacement in each shear bands under the critical value Δu^*. Therefore, instead of one major shear band propagation, multiple shear bands should be initialized to sustain the plastic deformation. Then the onset of fracture may be delayed and significant global ductility could be realized.

One of the approaches to restrain shear strain revolution in the shear bands is the geometrical constraints. It is found that under uniaxial compression test, specimens with low aspect ratios can achieve larger plastic strains (Zhang, Zhang et al. 2005; Bei, Xie et al. 2006). For monolithic metallic glass samples with dimensions of the order of 100 nm, large tensile ductility in the range of 23-45% is observed (Guo, Yan et al. 2007). However, highly restrictive configuration of geometry limits the application of metallic glasses as structure materials. Another method to constrain the shear bands is by producing laminated metal-metallic glass composites (Leng and Courtney 1989; Underhill-Lee and Wolfenden 1992; Park, Lim et al. 2006). In the thin metallic glass layers, catastrophic shear band propagation is restricted and formation of multiple shear band is promoted, which makes macroscopic plastic deformation possible.

On the other hand, metallic glass foams are fabricated to achieve macroscopic ductility. Brothers and Dunand (Brothers and Dunand 2005) prepared metallic glass foams $Zr_{57}Nb_5Cu_{15.4}Ni_{12.6}Al_{10}$, where 78% porosity exists. During compression, these foams show a strain of approximately 50%, with the sample remaining intact after unloading. Wada *et al*. (Wada, Kinaka et al. 2006) fabricated the porous bulk glassy alloys $Pd_{42.5}Cu_{30}Ni_{7.5}P_{20}$ with porosities of over 41%, which shows very high compressive deformability. They suggested high plasticity of the porous bulk glassy alloys is dominated by the stress concentration factor around pores, which can be controlled by the pore geometry.

Although most of the metallic glasses are brittle, there are some amorphous alloys that show significant ability of plastic deformation. Lewandowski *et al*. (Lewandowski, Wang et al. 2005) linked fracture toughness of metallic glasses with their elastic properties: if the ratio of shear modulus G and bulk modulus B, G/B, is smaller than 0.41, the metallic glasses are rated to be tough. The metallic glasses are brittle if their G/B are larger than 0.43. A low value of G implies weak resistance to plastic deformation in shear, while a high value of B implies strong resistance to the dilatation required for mode I crack propagation. Schroers and Johnson (Schroers and Johnson 2004) studied the same issue using Poisson's ratio as a parameters. For $Pt_{57.5}Cu_{14.7}Ni_{5.3}P_{22.5}$ with large Poisson's ratio of $v = 0.42$, large plastic strains in compression and bending were discovered combining with large fracture toughness. It is found that larger v enhances the formation of multiply shear bands. More shear bands sustaining the loading strain decreases the probability that shear displacement Δu in a single shear band reaches the critical value Δu^*. Therefore macroscopic plastic strain to failure can be achieved. By appropriately choosing components, it is possible to design metallic glasses with appropriate elastic constants to reach significant plasticity (Wang 2006). For example, by the appropriate choice of compositions of ZrCuNiAl BMGs, super plasticity of 160% is achieved at room temperature (Liu, Wang et al. 2007). Liu *et al.* proposed that glass matrix as hard regions surrounded by soft regions in the metallic glasses, enabling the glasses to possess plastic deformation. Since BMGs are very sensitive to their compositions, any minor deviations in content (< 1 atomic%) can substantially change the plasticity of the BMGs (Liu, Wang et al.

2007).

Besides, the plasticity of BMGs can be improved by introduction of residual stress or free volumes. Zhang *et al*. (Zhang, Wang et al. 2006) demonstrated that introducing compressive surface stresses in a bulk metallic glass leads to increased plasticity in bending and compression. The compressive stress on the surface facilities the onset of plastic flow, reducing the likelihood of surface cracking, and inducing more uniform deformation by a high population of pre-existing shear bands. Chen *et al*. (Chen, Setyawan et al. 2008) reported the improvement of plasticity in $Cu_{45}Zr_{48}Al_7$ monolithic BMG under compression is caused by a large amount of randomly distributed free volumes from solidification under a high cooling rate.

1.4 Deformation Behavior

The plastic deformation of metallic glasses on the macroscopic scales is essentially associated with defects under the accumulation of local shear stresses. There are homogenous deformation and inhomogeneous deformation events in BMGs, depending upon the temperature, the applied strain rate and the loading conditions.

1.4.1 Homogenous deformation

Homogeneous deformation of metallic glass typically happens at temperature above

$0.7T_g$. Under different strain rates and temperatures, there are two features of the homogeneous deformation: Steady-state flow and non-steady-state flow.

In a steady-state condition, there is a balance between structural disordering and ordering, which is manifested as defect creation and annihilation. Local-stress introduced atomic jumps or shear transformation zone (STZ) activation creates defects via dilatation; at the same time, defects are annihilated through relaxation. The activation of defect is described as:

$$\dot{s} = v_0 \cdot \exp(-\frac{Q-\tau V}{kT}), \quad (1.5)$$

where $\dot{s}$ is the rate of event when the applied shear stress is τ, k is the Boltzmann constant, T is the temperature, Q is the characteristic activation energy for the process and V is the activation volume of defect. The attempt frequency v_0 is essentially the frequency of the fundamental mode vibration along the reaction pathway, and should be of the order of the Debye frequency for a sufficiently local process (Schuh, Hufnagel et al. 2007). Lu *et al.* (Lu, Ravichandran et al. 2003) used this theory to character the homogeneous deformation of $Zr_{41.2}Ti1_{3.8}Cu_{12.5}Ni_{10}Be_{22.5}$, and obtained the activation energy of 4.6 eV and activation volume $V = 7.5 \times 10^{-29}$ m^3.

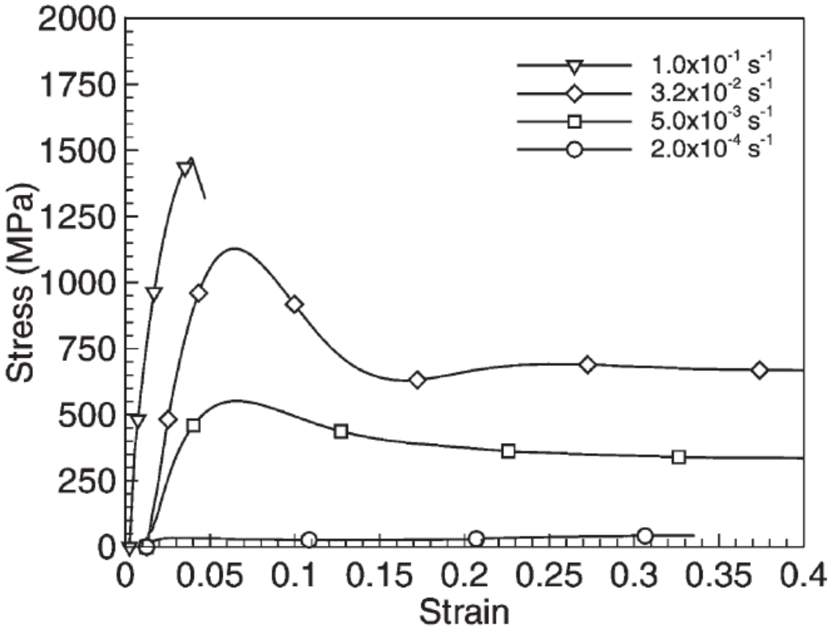

Figure 1.1 Effect of strain rate on the uniaxial stress-strain behavior of Vitreloy 1 at temperature T = 643 K and strain rates of 1.0×10^{-1}, 3.2×10^{-2}, 5.0×10^{-3} and 2.0×10^{-4} s^{-1} (Lu, Ravichandran et al. 2003; Schuh and Lund 2003).

Instead of a balance between defect creation and annihilation, defects in metallic glass can increase or decrease. Plastic deformation would result in defect creation which is sometimes temporarily stronger than the defect annihilation process. Thus stress overshoot can be seen on the stress-strain curve of homogeneous deformation, as shown in Figure 1.1. When the rate of defect annihilation resulted from diffusive relaxation matches the rate of defect creation, a steady-state flow is eventually achieved.

1.4.2 Inhomogeneous deformation and shear banding

Under high strain rate and low temperature, deformation in metallic glass is localized through the formation of rapid propagating shear bands which accommodates displacements. Although homogeneous flow is well modeled using straightforward statistical flow-rate theory, inhomogeneous flow in metallic glasses is a tough issue and not fully understood to date. Because mechanical properties such as strength, ductility and toughness are directly related to the formation and operation of shear bands, it is necessary to study this localized deformation mechanism.

Shear localization or shear band formation is generally thought to be directly caused by strain softening. When strain increases, the material would be softer and allows continuing localized deformation in higher rates due to the decrease of viscosity of the glass (Yoo, Park et al. 2009). Many possible reasons for this phenomenon have been proposed, including local production of free volumes due to flow dilatation, the local evolution of structural order due to the STZ operations, redistribution of internal stresses associated with STZ operations, and local heating (Schuh, Hufnagel et al. 2007). All these possible mechanisms are always considered to be companied by a local structure change of metallic glass.

Direct structural characterization of shear bands is a significant challenge, because of its nano-scale size. Several research groups have successfully characterized metallic glass specimens heavily deformed at low temperature using scattering techniques, and found structural disordering in the samples (Koba, Milman et al. 1994), which can be removed through annealing (Guoan, Cowlam et al. 1984). Transmission electron microscopy (TEM) is another method to characterize the shear band. The shear band thickness is observed to be 10 - 100 nm (Pekarskaya, Kim et al. 2001; Li, Spaepen et al. 2002; Jiang and Atzmon 2003). But this observation is limited to specimen as foils or thin films under bending or in-situ tension. Spaepen suggested the localized shear flow is related to the creation of free volumes (Spaepen 1977). It is found that inhomogeneous deformation would cause 0.1 - 0.2% decrease of its density (Cahn, Pratten et al. 1983; Nasu, Nagaoka et al. 1989). Cahn (Cahn, Pratten et al. 1983) approximated that dilatation inside the shear bands would be quite large (>10%) if deformation only happens in the shear bands, which results in quite high strain energy density in the shear bands. The free volumes increase in inhomogeneous deformation is verified by DSC measurements (Kanungo, Lambert et al. 2003; Cao, Li et al. 2005). This volume dilatation is also determined by positron annihilation and high-resolution TEM (Li, Wang et al. 2002; Suh, Dauskardt et al. 2003; Wright, Hufnagel et al. 2003).

Temperature could rise in the shear band due to local adiabatic heating, which leads to a great decrease in the viscosity of the metallic glass (Leamy, Wang et al. 1972). Infrared measurements clearly show temperature rises related to shear banding, however the temperature rise in the rapidly operated and nano-sized shear band is far beyond the spatial and temporal resolution (10 μm and 10 μs, respectively) of these techniques (Yang, Liaw et al. 2004; Spaepen 2006). Lewandowski and Greer (Lewandowski and Greer 2005) studied this issue by observing the melting of thin layers of tin coating on metallic glasses. Based on the fact that the width of the hot zone is larger than that of shear band measured in the electron microscope, Spaepen (Spaepen 2006) stated that the local heating can not be the origin of the shear localization, but a secondary effect which remains important to the evolution of the material in the bands, such as the nucleation of small crystals.

The crystallization in the shear band due to localized heating is a considerable debate as well. Demetriou and Johnson (Demetriou and Johnson 2004) stated that increasing temperatures as driving force for nucleation alone is not sufficient to explain the crystallization event. Crystallization can not happen if there are no pre-existing nuclei or no time for nucleation during the rapid heating by shear banding. Evidences are found to support this idea. For instances, Jiang and Atzmon (Jiang and Atzmon 2003) discovered that nanocrystals formation only locates inside the shear bands that are caused by compression, but no inside those caused by tension. They suggested the strain state rather than heating plays a major role in the formation of crystals. There is one of the other evidences that low loading rates, which would bring little increase of temperature, could introduce nanocrystals in shear bands during nano-indentation as well (Kim, Choi et al. 2002). One other explanation of this crystallization in shear band is the disruption of short range order due to localized shear flow (Chen, He et al. 1994).

1.5 Defects in crystalline solids

In contrast to those in amorphous material like metallic glass, atoms or molecules in crystalline solid are periodically arranged in three dimensions and the lattice in the crystalline solid exhibits lone-range order (Callister and Rethwisch 2007). Examples of crystalline solids are metals, diamond, ice and silicon. If the crystalline lattice of the entire sample is continuous and unbroken in all the three dimensions, we call this kind of crystalline materials as single crystalline solid (Bennett 2010). However, perfect pure single crystalline solid in meaningful size is almost impossible to be discovered in nature, and purification in the laboratory would be a difficult and costly process. In general, defect is inevitably introduced into the crystalline solid as an important factor which affects electrical and mechanical properties of real materials (Kallay 2000). These imperfections can exist in the crystalline structure as presence of impurity atoms at normal lattice sites or regions of completely different crystalline phase. Any missing and lacking of atoms or molecules in the prefect pure single crystalline structure or lattice and the irregular alignment of unit cells are called defect in the crystalline solid, which can be classified as three types: point defect, line defect (dislocations), interfacial defect or bulk defect.

1.6 Structural properties and deformation mechanisms in metallic glasses

1.6.1 Atomic structures

The atomic structure of metallic glass is considered as atomic structure of the frozen liquid phase comparing with the crystalline phase. The local icosahedral order is proposed by Frank (Frank 1952), because of its highly close packing and the lack of translational periodicity. However, as numerous approaches are carried out to verify Frank’s idea, it is found that surface effect plays an essential part for this icosahedral structure packing, suggesting that icosahedrons are not necessarily the structural backbones for bulk liquid (Wales 2003).

Bernal have proposed a dense random packing would for structures of metallic glasses, where hard spheres with different radii are considered to be randomly arranged (Bernal 1960; Bernal 1964). This hypothesis as a satisfactory model is only valid for mono-atomic metals and alloys with comparable atomic sizes. For the binary metallic glasses and noble metal-metalloid glasses, this model fails to describe their short-range ordering (SRO) and medium range ordering (MRO) (Gaskell 1978; Gaskell 1979; Gaskell 2005). Later Gaskell proposed a stereochemically defined model, which stipulates the local units (nearest neighbors) in amorphous metal-metalloid alloys to have the same type of structure as their crystalline compounds (Gaskell 1978; Gaskell 1979). However, the lacking of conclusive experimental evidences, especially for metal-metal alloys, has put this general idea under debate. As local nearest neighboring atoms are similar to their equivalent atoms and such similarity does not persist over an appreciable distance, short-range order (SRO) is preferred for local structure of metallic glasses. It is proposed that metallic glasses with higher packing density in their local structure would have higher GFA (Inoue, Negishi et al. 1998). However highly packed face centered cubic (fcc) and hexagonal close-packed (hcp) structures do not dominate the local structures of metallic glass in a supercooled state. As mentioned above, local icosahedral order model is recently considered as possible structural backbones for metallic glasses. This model has been verified by numerous experimental and computational results for some metal-metal alloys (Chen, Inoue et al. 2000; Chen, Dutta et al. 2001; Luo, Sheng et al. 2004). However, only metallic glasses with minor compositions would prefer the formation of icosahedral quasicrystals during annealing at supercooled liquid region (Chen, Inoue et al. 2000). And these metallic glasses are not the best glass formers. Therefore, it is possible that other types of local structure except icosahedral are favorable for glass forming.

Besides the local atomic packing structure like SRO, atomic structures which larger scales ordering were investigated. Micrcle (Miracle 2004) proposed medium-range order (MRO) in metallic glass, in which efficiently packed atomic clusters are retained as local structural clusters. Efficiently packing these sphere-like clusters in fcc or hcp configurations to fill three-dimensional (3D) space generates an extended structure. Because of the existence of internal strain and frustrations, this ordering system consisting of these clusters is limited only in a small dimension, which retains the disordering of metallic glasses in nanoscales. More recently, Sheng *et al*. suggested (Sheng, Luo et al. 2006) an icosahedral fivefold packing model to show the MRO. In this dense packing scheme, no appreciable translational symmetry can be detected in 1-2 nm scale.

1.6.2 Dislocation model

Amorphous phase have been discovered in the high-angle grain boundaries where higher-degree disordering atoms locates (Kawamoto and Ishizaki 1988; Oikawa, Koike et al. 1997; Chen, Sixta et al. 2000). Therefore, in early years, dislocation model was introduced to describe the atomic structure and deformation mechanism of metallic glasses. This concept is originally introduced as a line defect in continuum elastic media, which does not require any periodic lattices (Hirth and Lothe 1982). Gilman (Gilman 1965) proposed that the motions of dislocation lines can be used to describe the shear flow in noncrystalline solid. Although experimental results have proved this model, other investigations suggest the dislocation lines is uncorrelated individual molecular shears. Gilman (Gilman 1973) further proved his dislocation model in metallic glasses where individual molecular shears is negligible. Through experiment, he suggested that dilation at the core of a moving dislocation determines the viscous flow, and applied the free-volume theory to estimate the viscosity coefficient in the dislocation core.

Although dislocation model in metallic glasses has been studied for more than 40 years, it is an open question that whether dislocations can exist stably in metallic glasses. Because in the amorphous structures such as metallic glasses, dislocation with an intense stress field at its center would be relaxed rapidly through configurational rearrangements. Chanudhari *et al.* (Chaudhari, Levi et al. 1979) investigated the stability of edge and screw dislocations in an amorphous Lennard-Jones solid, and found that the screw dislocation can exist stably but the edge dislocation cannot, which would be relaxed. However, another study reported that both edge and screw dislocations can stably exist in the amorphous structure (Shi 1986). Recently, Takeuchi *et al.* (Takeuchi and Edagawa 2011) studied the stability of edge and screw dislocations in a model amorphous structure of $Ni_{33}Y_{67}$ alloy in molecular dynamic (MD) analysis, where the displacement field and the stress field were calculated to examine the stability of the dislocations in the metallic glass model. Their results showed both edge and screw dislocations are not stable in metallic glasses without a significant core-blunting, *i.e.*, there is a large stress-relaxation in the shear front (Takeuchi and Edagawa 2011) . Vereshchagin and Ostrikov (Vereshchagin and Ostrikov 2003) proposed a dislocation model of a polysynthetic shear band to calculate the stress field near parallel shear bands and determine regions of impurity localization near the defects. They believed shear bands can be represented in the form of alternating pores and dislocation chains since stress fields in the adhesion regions are produced by an edge dislocation cluster.

1.6.3 Free-volume model

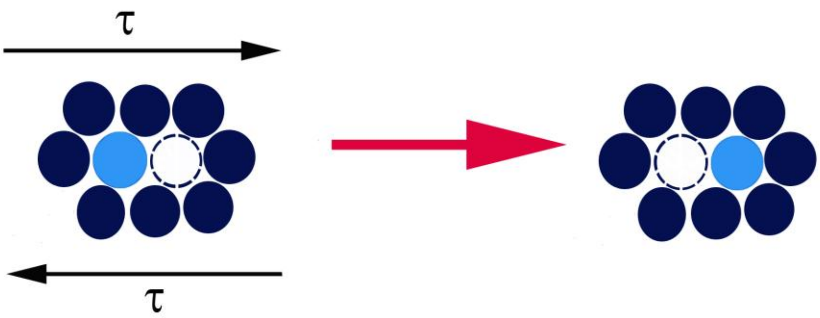

Figure 1.2 A two-dimensional schematic of free volume model in metallic glass. A shear displacement occurs to accommodate an applied shear stress τ, with a lighter atom jumping to empty space nearby (Spaepen 1977; Schuh and Lund 2003).

The widely accepted and also debated free-volume model to describe deformation of metallic glass is proposed by Gilman (Gilman 1975) and Spaepen (Spaepen 1977). In this model, empty space, which is regarded as free volume, exists in the dense atomic clusters (Turnbull and Cohen 1961; Turnbull and Cohen 1970). This free volume facilitates the local atom rearrangements without significant affection on surroundings during relaxation (Spaepen 1977). Therefore, when there is temperature or/and stress stirring, local deformation is more likely to occur at the free volume regions, as shown in Figure 1.2. Spaepen stated that an atom can be squeezed into a spare which is created by local stress. In this model, stress-created nonequilibrium free volumes can be retained at low temperature, at which deformation resistance decreases and shear deformation localizes. This stress concentration region can be regarded as defect for shear deformation.

As a simple explanation for deformation of metallic glasses at low temperature, free volume model is used to qualitatively describe their mechanical properties (Dai, Yan et al. 2005; Yu, Bai et al. 2007; Song and Nieh 2009). However, this model fails to elucidate the atomic rearrangement within shear bands during plastic flow. And it is probably that, instead of single atom, several atoms are involved in the local deformation process, where rearrangement may happen through atomic position exchange without free volume creation.

1.6.4 Shear transformation zone

Instead of single-atom based free-volume model, shear transformation zone (STZ) model is suggested by Argon (Argon 1979) to describe plastic deformation in metallic glasses. In this model, plastic deformation is performed by much larger flow units where internal stress concentrates, making atomic flow easier to occur. As shown in Figure 1.3, STZ, which is a small cluster of randomly close-packed atoms, spontaneously and cooperatively rearranges under the applied shear stress, STZ is a thin disk in the shear transformation direction (Argon 1979; Schuh and Lund 2003).

At the free-volume sites, the nucleation of STZ is likely to happen due to the applied shear stress concentration. The operation of one STZ promotes its surrounding atoms to move along activation paths, resulting in autocatalytic formation of large planar bands, commonly called shear bands, which mainly suspend the plastic deformation of metallic glasses (Schuh and Lund 2003).

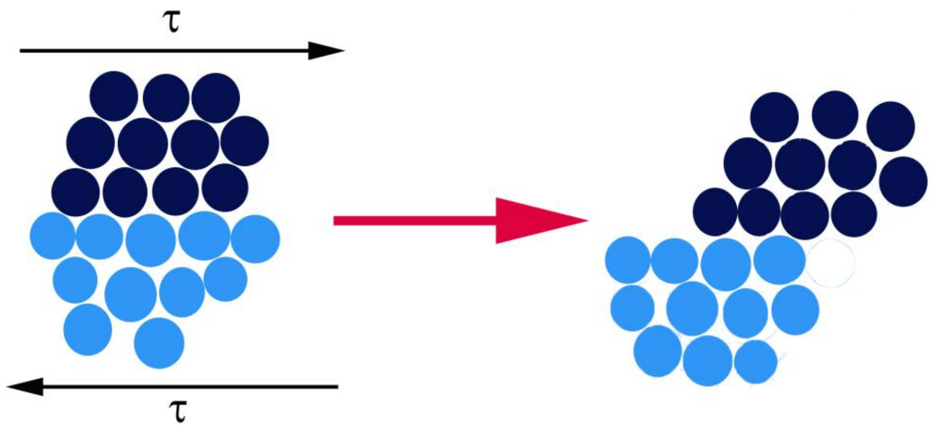

Figure 1.3 A two-dimensional schematic of a shear transformation zone in metallic glass. A shear displacement occurs to accommodate an applied shear stress τ, with the darker upper atoms moving with respect to the lower atoms (Argon 1979; Schuh and Lund 2003).

1.6.5 Cooperative shearing model

It is possible to describe the atomic rearrangement in metallic glass based on the model of potential landscape, since interatomic potential or intermolecular potential is the foundation for structural variations (Stillinger 1995; Malandro and Lacks 1998; Malandro and Lacks 1999). Based on this theory, numerical applications can be carried out to describe relaxation dynamics, glass transition, and plasticity of glasses (Wales 2001). A cooperative shearing model (CSM) is developed by Johnson and Samwer (Johnson and Samwer 2005) from the energy landscape theory and Frenkel scheme for the shear deformation of defect-free crystals. Yield or plastic deformation would happen when the applied shear stress lower the potential energy barrier close to zero. By linking the yielding strength to temperature and strain rate, CSM provides an effective description of plasticity of metallic glasses. The activation rate of STZ can be predicted as well.

1.7 Metallic glass composite

Although metallic glasses do show plastic strain to failure in compression and bending, they are very brittle in tension, with almost no plastic strain to failure. The reason for this difference is that crack initiation occurs almost immediately after the formation of the first shear band in tension without formation of multiple shear bands to sustain the loading, which leads to catastrophic failure of BMGs. To achieve macroscopic plastic deformation in BMGs, extra crystalline phases would be introduced into the BMG matrix or phase separation is created to produce composite to promote the generation of multiple shear bands. The crystalline phase may be obtained in two different ways: (1) ex situ processes, through separately adding crystalline phase during melting; (2) in situ processes, forming crystalline phases during solidification by subsequent processing of the BMG when partial crystallization of the glassy phase occurs. For BMG composite prepared by phase separation, if glass devitrification transformation is avoided during cooling, the supersaturation would allow subsequent spinodal decomposition to occur.

BMG composites based on Cu-, Fe-, Mg-, Ti-, and Zr-based BMGs have been fabricated and tested. The type of reinforcements employed include metal wires such as Cu, Mo, Ta, Ti, W, and steel, ceramic particles such as CeO_2, Cr_2O_3, SiC, TiB, TiB_2, TiC, Y_2O_3, ZrC, ZrN, ZrO_2, carbon nanotubes, diamond, and graphite in the ex-situ processing of BMG composites, and crystalline dendrites in the in-situ processing of BMG composites (Inoue 2010). Significant improvement of the toughness and ductility of BMGs in tension is discovered in some of these attempts.

Besides the mechanical properties of reinforcement, the shape, volume fraction and distribution of reinforcement would affect the mechanical properties of BMG composite. Sun *et al.* (Sun, Chen et al. 2007) discovered that altering the dendritic morphology of the crystalline phase into spherical particles results in the increase of plastic strain from 8.8% to 12%, at the same time improving the yield strength and fracture strength. The better ability for plastic deformation may come from the effects of in-situ formed spherical dendrite on shear band formation and propagation (Schuh, Hufnagel et al. 2007).

Instead of single shear band introduced catastrophic failure in monolithic BMGs, structural inhomogeneities of BMG composites would trigger the formation of multiple shear bands and therefore reduce the risk of catastrophic failure and improve the ductility. There are three possible reasons for this optimization in BMG composite. First, when the reinforcing material is introduced into BMG matrix to form BMG composite, due to different coefficients of thermal expansion of matrix and reinforcements, residual stress is inevitably introduced at the matrix/reinforcement interface. These stresses can reach several hundred MPa, which can significantly affect the mechanical behavior of the BMG composite. Second, due to the difference in elastic modulus, stress would concentrate on the interface of matrix and reinforcement under external loading. Third, additional stress from the plastic mismatch strain between matrix and reinforcement would bring stress concentration on the interface. If the stress concentrated on the interface surpasses the critical value, nucleation of deformation defects would occur to allow shear band to propagate into the matrix.

On the other hand, reinforcements act as barrier to prevent the shear bands from developing into cracks. According to the experimental evidences, the reinforcements can obstruct, block, deflect, divide and absorb shear bands, depending on their sizes and stress concentration around them (Pekarskaya, Kim et al. 2001; Hufnagel, Fan et al. 2002; Xu, Ma et al. 2005). These interactions are found to be much stronger during compressive stresses rather than tensile stresses due to strain softening. Hofmann *et al.* suggested that by introducing inhomogeneity of elastic or plastic material in metallic glass matrix at a microstructural length scale $L<r_p$, ‘microstructural’ stabilization becomes possible in tension. r_p is the plastic zone size described in Eq. (1.3), which is related to a maximum allowable shear offset along the shear band (Hofmann, Suh et al. 2008). Shear bands initiated in plastically soft regions (with lower σ_y or lower shear modulus G) can be efficiently arrested in surrounding regions of higher yield stress or stiffness which limit shear band extension and restrict crack development. Therefore higher toughness and ductility are achieved.

For the BMG composites reinforced by crystalline materials, failure occurs at reduced strength levels with strain softening after yielding compared with monolithic BMG. To overcome such problem, metallic glass composites are fabricated by phase separation which forms spinodal glass matrix with a periodic arrangement of nanoscale clusters, keeping the two amorphous states at the same time. Branagan *et al*. (Branagan, Zhou et al. 2010) reported iron-based BMGs with significant strain hardening, high tensile strengths up to 5GPa, and elongations up to 7%. Ductility could be achieved through shear band blunting, shear band arresting and interaction, and the formation of secondary shear bands.

1.8 Simulation tools for metallic glasses

As mentioned above, TEM observation of shear band is limited to specimens such as foils or thin films under bending or in-situ tension. At the same time, only shear band or crack on the fracture surface can be directly observed by SEM. For the shear bands in bulk metallic glasses, both TEM and SEM are incapable to catch their characteristics, especially to capture their dynamic revolutions such as initiation and propagation. Computer simulations provide unique insights into the deformation processes in metallic glasses. They are usually applied to help understanding the atomic structures in shear bands and the macroscopic distribution of shear bands. Numerical simulation tools, including *ab initio* molecular dynamics (*ab initio* MD), classical molecular dynamics (classical MD) and finite element method (EFM) *etc*. have been applied to investigate shear localization. However, the computer modeling may also have serious limitations, as the time and spatial scales involved are much shorter and smaller than which in the real world.

In *ab initio* MD, the density functional approach has been used to study the structures of metallic glasses (Jakse, Lebacq et al. 2004; Hui, Gao et al. 2008). Due to the limitation in the time (~ ps) and spatial scales (~ 500 atoms), its application on the understanding of shear banding is limited. To overcome these difficulties, classical MD employing empirical potentials was applied to study different types of systems. Classical MD runs much faster than *ab initio* MD by using simpler expressions of inter-atomic potentials, and both its time and size scales are largely extended. Li *et al*. (Li and Li 2006) applied MD simulation to analyze shear bands in CuZr metallic glasses, showing that shear band is indeed a region with a liquid-like structure due to both local heating and free-volume generation. Cheng *et al*. (Cheng, Cao et al. 2009) used MD summations to study binary CuZr metallic glasses. Shear offset associated with a dominant shear band and spread-out shear transformations are observed depending on samples with different cooling rates. They also demonstrated full icosahedral ordering as the key structural feature in the CuZr metallic glasses, controlling not only the G and the G/B (or v) but also the initiation of shear localization and the intrinsic plasticity. For BMG composites, Wang *et al*. (Wang, Li et al. 2007) conducted MD simulations of amorphous CuZr and crystalline Cu nanolaminate systems in tension, which provides crucial information about atomistic movement unavailable from experiments. They found geometric incompatibilities would force dislocation propagation to be disrupted and dissolved by amorphous layers. However, MD simulations of metallic glasses usually focus on binary systems. For trinary or more complex systems, it is difficult to use MD simulation due to the complicated atomic potentials. Moreover, MD simulation would only be performed in the samples with size less than 100 nm (Shimizu, Ogata et al. 2007), which is difficult to investigate the macroscopic mechanical properties such as catastrophic failure of metallic glasses. Besides, its time scale (~ns) is still shorter than that for realistic deformation of BMGs. Therefore, caution must be paid when interpreting the observations in simulations and making connections with realistic BMGs.

For BMGs, especially the BMG composites, finite element method was adopted to simulate their mechanical behaviors. Kim *et al*. (Seop Kim, Kato et al. 2004) presented FEM modeling of overall and local deformation behaviors of the Pd-based

BMG. FEM based on the macroscopic scale continuum mechanics illustrates local inhomogeneous tri-axial stress, which is difficult to be characterized through experiment. FEM is also used for the comprehensive interpretation of the deformation of BMG composite conquering the limitation on neutron diffraction experiments (Lee, Clausen et al. 2005). Although the mechanical behaviors is successfully caught through FEM simulation, some essential information about deformation is lost since the carrier of plastic strain in BMGs is shear band with a size of tens of nanometers. Hence new simulation method based on the atomic deformation mechanisms of BMG should be sought to theoretically explain the formation and propagation of shear bands or cracks in different BMGs and BMG composites. Since experiments of preparing BMG composites would cost a great deal of expenses, simulation work in reasonable scales is a economic way to predict the materials failure or guide the design of new advanced BMG or BMG composite for potential engineering applications.

1.9 Objectives of this thesis

In metallic glasses, atoms are disorderly organized to form an amorphous structure without periodic crystalline lattices. Due to the dense random packing, the local atomic topology would be different from place to place. Some clusters can be considered as defects where the atomic structure is loose comparing with those in other denser regions. Obviously, this structural differentiation is closely related with the rapid quenching which keeps atomic structures as frozen liquid phase. The clusters with loose atomic structure are considered as as-synthesized defects.

As loose atomic units, the as-synthesized defects can be the sources for atomic rearrangements under thermal stimulation. Since the nature of defects as well as structural relaxation events is an essential factor that affects the mechanical properties of metallic glasses, it is necessary to deeply understand the relation between defects and structural relaxation in metallic glasses.

The loose atomic units in metallic glasses also can be the significant sources for plastic deformation under mechanical stimulation. The clusters resulted from plastic deformation with not fully dense atomic structures compared with those of the un-deformed glassy matrix can be considered as deformation defects. To date, the feature of the deformation defects in metallic glasses is still under debate. It is necessary to deeply understand the existing nature of deformation defects in metallic glass and how they work during deformation of metallic glasses, since they are basic deformation units in metallic glasses.

Phase-field simulation tool can effectively assist us to study thermal and mechanical behaviors of metallic glasses. Based on the results from experiments and further analysis, a model can be theoretically set up to describe the deformation behavior of metallic glass. Through the modeling, shear deformation in metallic glasses and metallic glass composites can be illustrated, which can be applied to interpret the formation of shear bands, and further guide the design of advanced BMG composites for potential engineering applications.

The objects of this thesis are to characterize the deformation defects in metallic glasses after various thermal and mechanical treatments by testing the internal friction of these samples, and to model the shear banding in metallic glasses and their composites by phase field modeling with necessary parameters determined from these experiments.

1.10 Organization of this thesis

This thesis consists of six chapters. Following this Introduction Chapter, Chapter 2 will introduce the experimental methods in this study, mainly the internal friction test with dynamic mechanical analysis. After different thermal treatment conditions, different structural and energy configurations of metallic glasses can be manifested on internal fiction described in Chapter 3. An important parameter will be proposed to effectively describe the relation between defects and structural relaxation in metallic glasses. In Chapter 4, dynamic mechanical analysis will be further applied to characterize the deformation defects in the metallic glass. Creation and annihilation of these deformation defects are defined as a phase transition process and important parameters such as activation energy and surface energy will be obtained from these experiments for later computer modeling. In Chapter 5, a phase field modeling will be set up based on the experimental findings and the characteristics of deformation defects to simulate the shear band initialization and propagation in the metallic glass. Different failure types in metallic glass composites will be presented under different reinforcement, boundary and loading conditions. Then based on this modeling we will investigate the interaction among shear bands and the generation of secondary shear band. Finally conclusions will be given in Chapter 6.

2. Experiment method

2.1 Internal friction study on defects in metallic glasses

2.1.1 Dynamic mechanical analysis

Dynamic Mechanical Analysis (DMA) is a technique used to measure the mechanical properties of materials. The most important features of any DMA are how the stress is applied to the sample, and how the resulting strain is measured. We use new generation DMA (TA Q800) in our experiment. The Q800 DMA utilizes state-of-the-art non-contact, linear drive motor technology to provide precise control of the stress. Strain is measured using optical encoder technology that provides unmatched sensitivity and resolution. Along with low friction air bearing technology, the Q800 provides superior performance compared to traditional designs that employ stepper motors, and mechanical springs.

The most common test is applying a dynamic oscillatory test with a sinusoidal stress to the material and a sinusoidal strain is measured as shown on Figure 2.1 (a) and (b). Also measured is the phase difference, δ, between the two sine waves. The phase lag will be zero degree for pure elastic materials and 90 degrees for purely anelastic materials. Most materials including metallic glasses exhibit an intermediate phase difference.

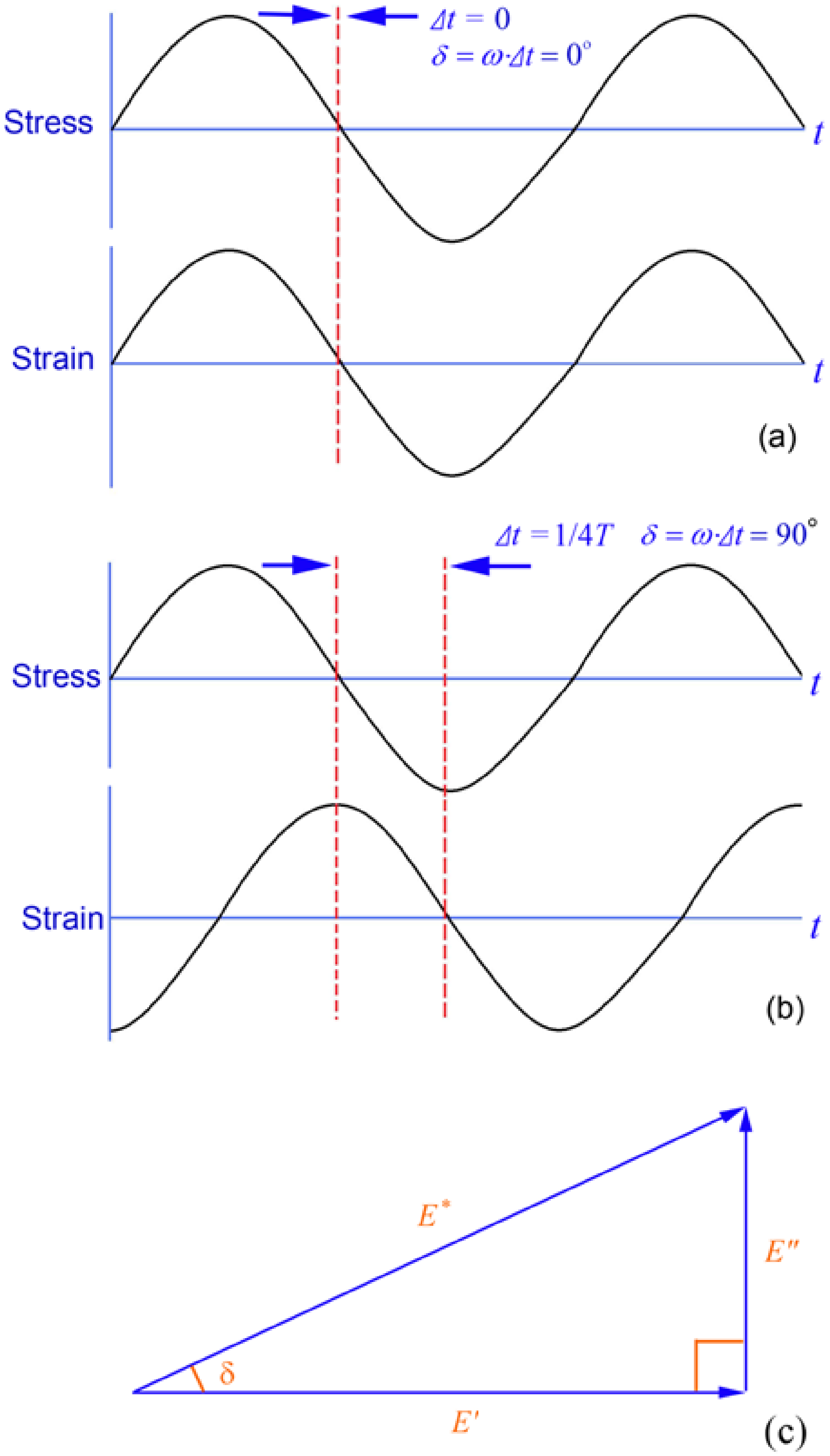

Figure 2.1 (a) Strain vs. stress of pure elastic behavior, (b) Strain vs. stress of pure anelastic behavior, and (c) the phase angle δ in DMA testing.

DMA differs from other mechanical testing devices in two important ways. First, DMA testing focuses on both the elastic and anelastic, or viscous components. Therefore, it is able to obtain the viscous properties of the materials such as viscosity. Second, DMA works primarily in the linear viscoelastic range and is therefore more sensitive to structure than the conventional tensile test devices which work primarily outside the linear viscoelastic range.

2.1.2 Internal fiction measured by DMA

Dynamic Mechanical Analysis (DMA) is used to detect the dynamic mechanical behavior of the sample through mechanically deforming a sample and measuring its response. The loading stress can be applied sinusoidally or, in a constant (or step) fashion, or under a fixed rate and the response to the deformation can be monitored as a function of temperature or time. If deformation strain is small enough and is applied slowly enough, the molecular or atomic arrangements are near its equilibrium site (Mark 2007). Therefore, mechanical response is just a reflection of dynamic processes at the atomic level in the metallic glasses, which bridges the gap between atomic structure of metallic glasses and their mechanical performance. Normally, structural relaxation or transformation in materials is accompanied by a volume change or a shear deformation, which may response to an alternating stress. Therefore, besides the elastic strain created by loading stress, additional strain is introduced by the structural changes. As the phase lag between stress and strain increases, the hysteresis increases, leading to the increase of energy loss measured as internal friction.

Internal friction in DMA test is usually considered as stress-strain hysteresis in the case of cyclic loading, which is a process of mechanical energy dissipation connected with deviations from Hooke’s law. The value of internal friction can also be expressed as

$$Q^{-1} = \Delta W/2\pi W, \tag{2.1}$$

where ΔW is the energy dissipation or lose during one cycle and W is the elastic storage energy W during that cycle. For sinusoidally varying stress

$$\sigma^{*} = \sigma_0 \mathrm{e}^{\mathrm{i}\omega t}\,, \tag{2.2}$$

the corresponding strain can be expressed as

$$\varepsilon^{*} = \varepsilon_0 \mathrm{e}^{\mathrm{i}(\omega t-\delta)} = (\varepsilon' - i\varepsilon'')\mathrm{e}^{\mathrm{i}\omega t}, \tag{2.3}$$

where ω is the circular frequency and δ is the phase angle, or phase shift, between the deformation and response due to the anelastic behavior of the materials. Several essential mechanical parameters in the dynamic deformation can be defined as a function of the circular frequency ω, *i.e.* the complex modulus measuring overall resistance to deformation can be expressed as

$$E^{*}(\omega) = \sigma^{*}/\varepsilon^{*} = E(\omega)e^{i\delta(\omega)} = E'(\omega) - iE''(\omega), \qquad (2.4)$$

where E' is the elastic modulus, or storage modulus, which manifests the ability of the material to store energy; E'' is viscous modulus, or loss modulus, which indicates the ability of the material to dissipate energy lost as heat. All the parameters can be calculated with DMA as illustrated in Figure 2.1 (c). The tangent of the phase angle δ is the ratio of the loss modulus to the storage modulus, $Q^{-1} = \tan \delta = E''/E'$, defined as internal friction, which is a measure of the damping ability of the material. These parameters can be calculated as a function of time, temperature, frequency, or amplitude (stress or strain) depending on the application.

Since any volume change or a shear deformation would introduce phase lag between stress and strain in dynamic mechanical measurement, all the information about structural changes can be detected as variations of internal friction. During the structural relaxation and mechanical deformation, a new energy configuration would be achieved through annihilation, creation, recombination, and redistribution of defects. Because irreversible processes are closely connected to atomic structural variations in the metallic glasses (Yoo, Park et al. 2009), any transformation about defects can be detected through dynamic mechanical analysis and further reflected as the change of internal friction.

In the temperature below T_g, the internal friction would increase exponentially with temperature (Tyagi and Lord Jr 1979). Previous research by Morito and Egami (Morito and Egami 1984) had found that internal friction spectrum would be reversible through cycle heating and annealing at different temperatures, suggesting that sub-T_g structure relaxation is a reversible process. However, more recently, it was found that internal friction was reduced comparing to the previous heating run, when the as-quenched sample was heated with a constant rate to successively increasing temperatures (Khonik, Kitagawa et al. 2000), which demonstrates irreversible structural relaxation in metallic glasses after thermal treatment. Although internal friction is an important measure of structural change in the amorphous material, no relaxation peak about defects can be found in these internal friction tests. This is because strong internal friction peak appears at a temperature close to the onset of crystallization, when sufficient atomic mobility is achieved for the irreversible phase transition from an amorphous state to a crystalline state. Before reaching the maximum value, internal friction will even rise significantly because of the increasing atomic mobility at elevated temperature close to the glass transition temperature, which makes the internal friction variation resulting from the structural relaxation relatively unapparent. To study the change of defects in metallic glasses during structural relaxation, it is necessary to clarify the internal friction variation below T_g.

We use metallic glass ribbons in our experiment. Thin film tension mode is applied in Q800 DMA. In this mode, the sample is placed in tension between two fixed and moveable clamps. In oscillation experiments, a small static force is applied in order to prevent buckling. The clamps feature very simple mounting and because the drive shaft does not rotate, no twist is induced in the sample that can lead to inaccurate data.

2.2 Thermal analysis method

Differential scanning calorimeters (DSC) measures heat flows associated with phase transitions in a material as a function of temperature. Properties measured by DSC include glass transitions, crystallization, and melting etc. A reference is placed in DSC chamber with nearly the same temperature as the sample throughout the experiment, when temperature linearly increases as a function of time. More or less heat will flow into or out of the sample than the reference when phase transformation such as glass transitions, crystallization, and melting occurs, depending on whether the process is exothermic or endothermic.

Thermodynamic properties of metallic glasses used for DMA tests are investigated by TA DSC Q200, and the glass transition temperature T_g and the crystallization temperature T_x are determined as the onset temperatures of these events. Glass transition temperature T_g with extreme slow heating rate can be deduced inversely by extrapolating the relation between T_g and ln $\dot{T}$ (Ichitsubo, Matsubara et al. 2005). ΔT is set to be T_x-T_g with typical heating rate 20 K/min. For metallic glass with much higher liquid temperature T_l, thermogravimetric analyser/ differential scanning calorimeter (Netzch TGA/DSC) is used with typical heating rate of 20 K/min to analyze their thermodynamic properties.

2.3 Conclusion

Because of the its sensitivity, dynamic mechanical analysis is a useful tool to study the internal structural variation of metallic glass, such as glass transition, crystallization and defects relaxation and transformation. Information about defect creation and annihilation can be obtained from the internal friction spectrum, which will be described in Chapter 3 and 4.

3. Internal friction tests

3.1 Introduction

Structural relaxation can be considered as atomic structural variation of condensed matter due to external perturbation. In crystalline materials, this phenomenon is manifested as production, annihilation and rearrangement of defects (Zhou, Liao et al. 2003; Chekhovskoi and Peletsky 2011), which include vacancies, dislocations, grain boundaries, etc. For defects distributed in ideal crystal, their characteristics can be identified and well quantified. For the metallic glasses, as-synthesized samples can be considered in configurational equilibrium, but it is a thermodynamic non-equilibrium state, where unstable atomic clusters (or defects) are distributed in the ideal glass matrix due to the rapid quenching from liquid state. Thus, thermal relaxation would lead to the formation of glass in a lower energy configuration through annihilation of these defects. Structural relaxation in metallic glasses results in changes in both topological and compositional short-range order, through the annihilation, recombination, and redistribution of as-synthesized defects to pursue ideal glassy state (Egami 1981). Therefore, the as-synthesized glass can be considered as a composite of ideal glass and defects. Furthermore, the reversible β and larger scale α relaxation would closely relate with defects as well. As weakly organized units in the ideal-glass matrix, defects in metallic glasses could be the favorite sites for β relaxation. Moreover, glass transition can be achieved by α relaxation, when defects in glasses can be considered as being violently activated, making the whole matrix as weak as supercooled liquid. The characteristics of relaxation of as-synthesized defects would be crucial to the mechanical properties of metallic glasses. Unfortunately, the nature of these structural relaxations involving defects in the metallic glasses is still a challenging and unsolved issue.

In this chapter, we will study the local structural nature and its variation in metallic glasses annealed at temperatures below T_g using dynamic mechanical analysis (DMA). The roles of as-synthesized defects in structural variation will be explored.

3.2 Experimental methods and results

The metallic glass ribbon $Pd_{73}Si_{20}Cr_7$ was chosen for the experiment. The glass transition temperature T_g and crystallization temperature T_x of this sample is below 400 ℃, which is within the operation limit of the DMA equipment.

The metallic glass ribbon $Pd_{73}Si_{20}Cr_7$ with 10 μm in thickness and 700 μm in width was prepared by roller melt-spinning method. The metallic glass ribbons were examined by X-ray diffraction to prove their amorphous structure as shown in Figure 3.1 (a). Isothermal treatment was carried out in vacuum furnace for at least 10 hours. Therefore, stable state of samples could be achieved after sufficient relaxation. The glassy matrix of the annealed sample was verified by X-ray diffraction again after the thermal treatment, as shown in Figure 3.1 (b).

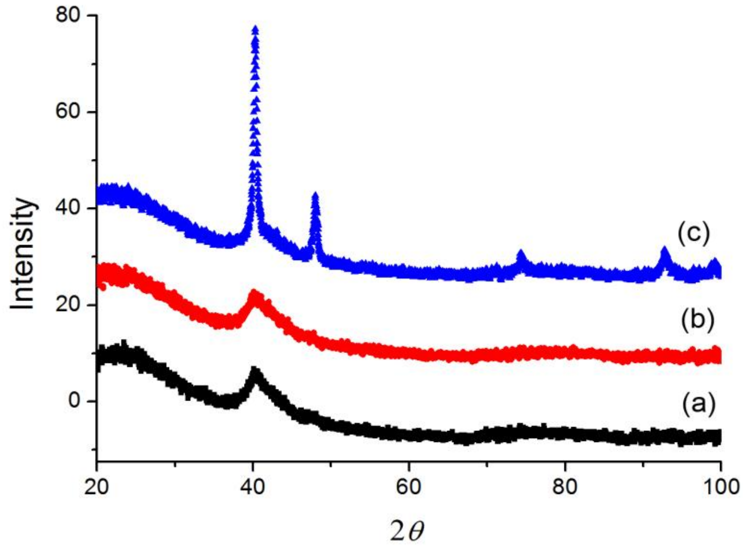

Figure 3.1 XRD patterns of (a) as-synthesized, (b) T_a = 543K and (c) T_a = 553K relaxed $Pd_{73}Si_{20}Cr_7$ glassy alloys.

3.2.1 Internal friction analysis on structural variation

Internal friction measurement of the amorphous ribbons was performed in thin film tension mode. In this mode, the sample is placed in tension between a fixed and moveable clamp. The clamps are suitable for both films and fibers. All the ribbon samples were under tensile deformation with a maximum tensile strain fixed at 0.1% in an Argon-flushed atmosphere. In oscillation experiments, the instruments use a variety of methods for applying a static load to prevent buckling and unnecessary creep. The “force track” mode is set to be 125%, which means the average strain is 25% larger than the amplitude of the applied sinusoidal strain for internal friction measurement, keeping samples in tension condition during the whole testing process.

DMA operates with frequency sweep mode from 0.1 Hz to 4 Hz. In order to study structural variation under different external loading at different temperatures, instead of “force track” mode, different static forces of 3N, 4.5 N, 6 N, 7.5 N, 9 N, 12 N and 15 N are applied to pre-load the samples in different tensile conditions during DMA testing.

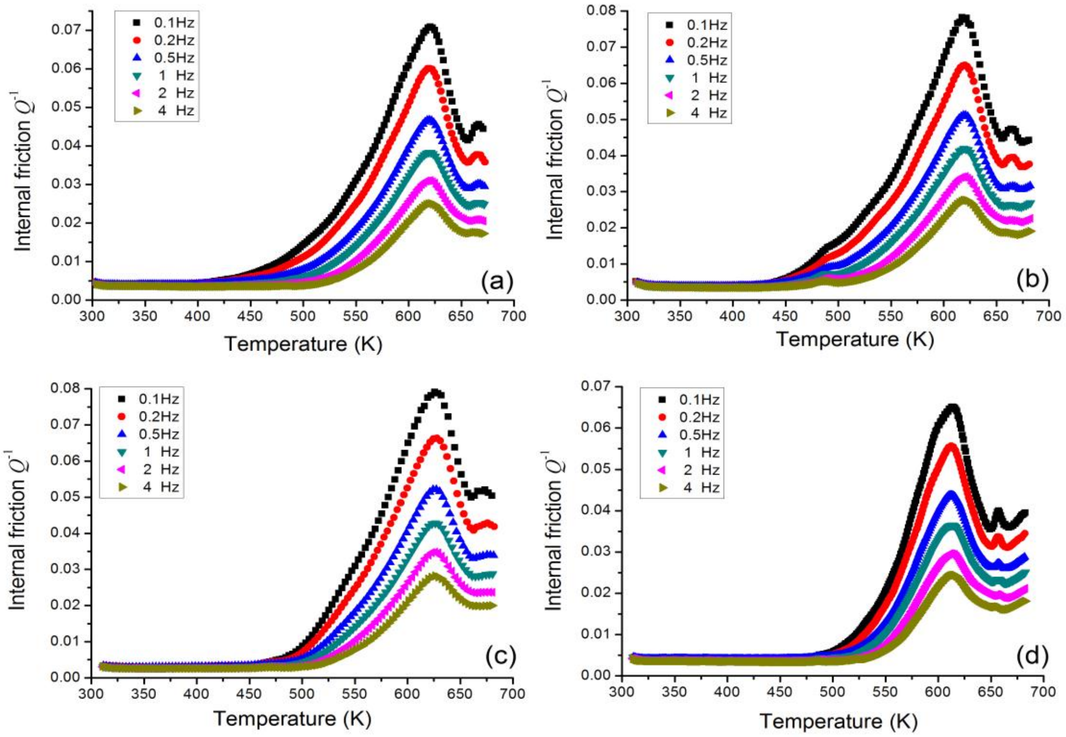

Figure 3.2 Internal friction of (a) as-synthesized $Pd_{73}Si_{20}Cr_7$ and (b)-(d) $Pd_{73}Si_{20}Cr_7$ after structural relaxation at different temperatures T_a = 423K, 473K and 543K, respectively. The heating rate is 0.6K/min for all the tests.

The internal frictions of as-synthesized $Pd_{73}Si_{20}Cr_7$ and $Pd_{73}Si_{20}Cr_7$ after structural relaxation at different temperatures T_a are shown in Figure 3.2. At the same testing frequency, $Pd_{73}Si_{20}Cr_7$ samples annealed at different temperatures T_a show different internal frictions as shown in Figure 3.3. All the peaks of internal frictions in Figure 3.3 consistently locate at 627 K with a heating rate of 0.9K/min. However, sample annealed at higher temperature shows lower internal friction. At temperature below 420 K, internal frictions of all samples nearly overlap. As the temperature increases, the significant increase of internal friction begins at 420, 500 and 520 K for samples with T_a = 373, 473 and 543 K, respectively.

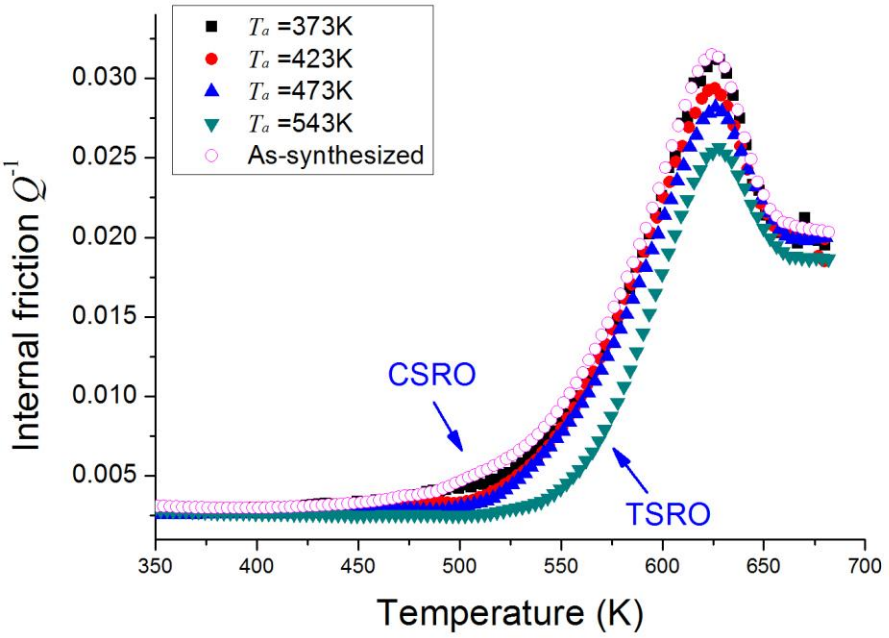

Figure 3.3 The internal friction of $Pd_{73}Si_{20}Cr_7$ samples with different annealing temperatures. The testing frequency is 4 Hz, the heating rate is 0.9 K/min. The variations of internal friction curves at low and high temperatures is related to chemical short range ordering (CSRO) and topological short range ordering (TSRO) as indicated by the arrows, respectively.

Internal frictions of sample under different tensile tresses are shown in Figure 3.4. The internal friction is found to significantly increase at lower temperature under larger loading tensile stress. For the loading stress σ as large as 0.82 GPa or more, samples would fail before the appearance of internal friction peak. More intensive internal friction peak can be detected for the sample under larger tensile stress. Besides, the peak shifts from 608 K to 612 K when the tensile stress increases from

0.31 GPa to 0.62 GPa.

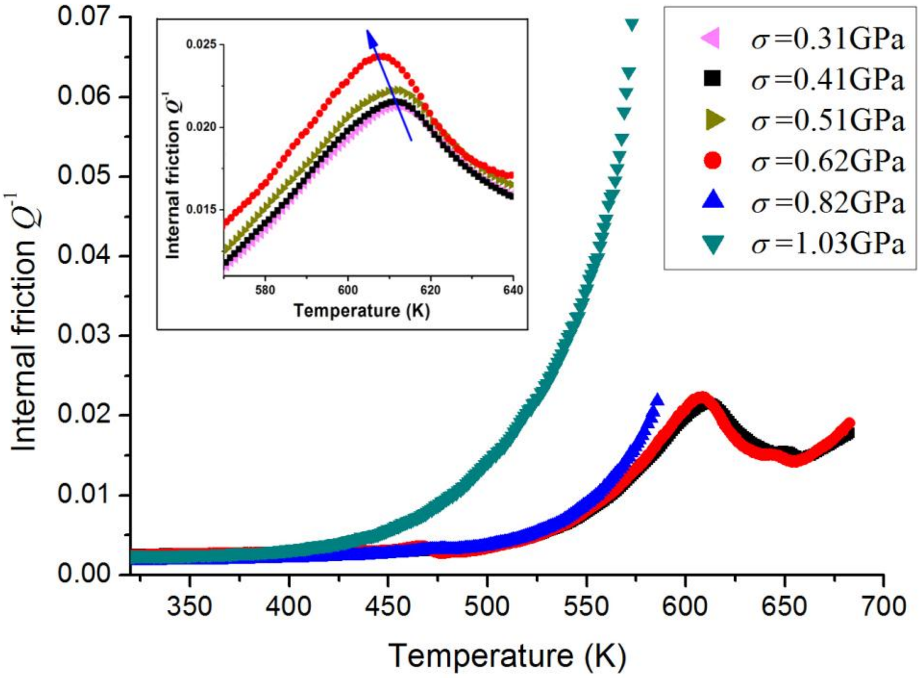

Figure 3.4 Internal friction of $Pd_{73}Si_{20}Cr_7$ samples under different pre-loading stresses. The testing frequency is 4 Hz, the heating rate is 0.3 K/min.

3.2.2 Energy barrier for structural activation

Based on the classical Debye analysis, the internal friction can be described by angular frequency ω and relaxation time τ' as (Nowick 1972):

$$Q^{-1} \approx \frac{\omega\tau'}{1+(\omega\tau')^2}, \quad \tau' = \tau'_0 e^{-\frac{E_a}{k_B T}}, \tag{3.1}$$

where τ'_0 is a constant and K_B is Boltzmann constant. When the temperature approaches glass transition, the relaxation time τ' is large. This equation can be modified as:

$$Q^{-1} \approx (\omega\tau')^{\alpha'}, \tag{3.2}$$

which can be further rewritten as:

$$\ln Q^{-1} = \alpha'(\ln\omega + \ln\tau'_0 - \frac{E_a}{k_B T}) \tag{3.3}$$

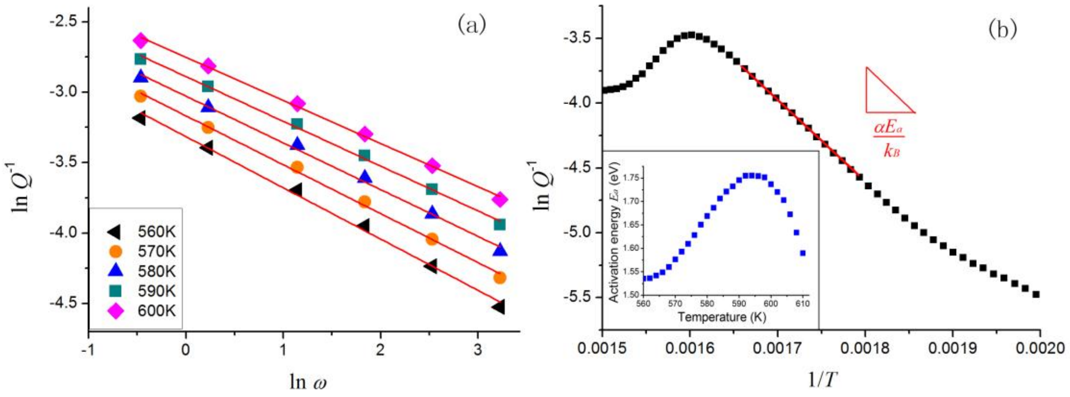

Figure 3.5 (a) The linear relation between lnQ^{-1} and lnω near glass transition; (b) The linear relation between lnQ^{-1} and 1/T near glass transition; (Inset) Activation energy E_a calculated at temperature close to T_g using Eq. (3.3).

As shown in Figure 3.5 (a), linear relation between lnQ^{-1} and lnω can be observed near glass transition (T_g =585 K). The value of coefficient α' in Eq.(3.2) can be obtained by linearly fitting lnQ^{-1} and lnω with fixed temperature. Therefore in Eq.(3.3), the activation energy E_a can be obtained by linearly fitting lnQ^{-1} and 1/T near glass transition temperature with fixed frequency as shown in Figure 3.5 (b). E_a at different temperatures are shown in the insert of Figure 3.5 (b). We would define the temperature, where E_a reaches its maximum value E_0, as the glass transition temperature T_g, since this turning point may represent a great change of the atomic configuration of the glassy matrix. The T_g defined by E_a maximum is found to be consistent with that measured from DSC.

3.2.3 Activation volume of defects

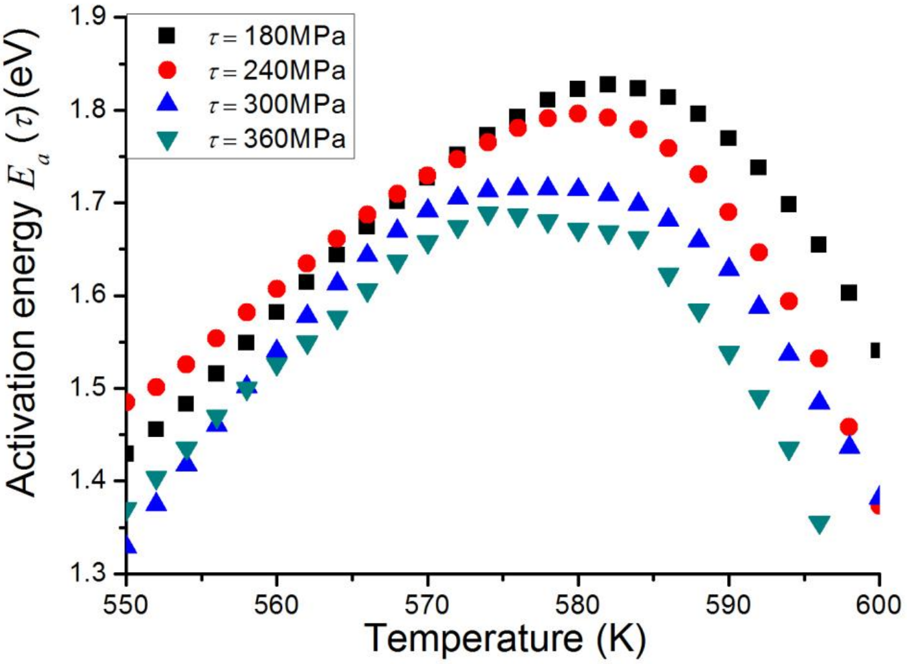

Figure 3.6 The activation energy of as-synthesized $Pd_{73}Si_{20}Cr_7$ samples with different pro-loading tensile stresses. The heating rate is 0.6K/min.

Table 3.1 Characteristics of glass transition of as-synthesized sample under different pro-loading tensile stresses

Shear stress	**180MPa**	**240MPa**	**300MPa**	**360MPa**
E_0 (τ) (eV)	1.83	1.80	1.72	1.69
T_g (K) ($\dot{T}$=0.6K/min)	582	580	579	577

With the same method as described above, the activation energy of samples under different pre-loading stresses can be obtained. Under tensile loading, fracture would happen at elevated temperature during the test. Thus the applied shear stress is restricted to below 360 MPa in the DMA tests. As shown in Figure 3.6, the apparent activation energy $E_0(\tau)$ decreases as tensile stress increases. Simultaneously, the peak temperature of $E_0(\tau)$, which represents glass transition temperature T_g, shifts towards a lower temperature with increasing loading stress. This phenomenon illustrates that the stress would reduce the barrier for activation of local atomic clusters, facilitating the structural activation of glassy alloy (Jin, Wen et al. 2005). According to the transition state theory (Schuh, Hufnagel et al. 2007), the applied tensile stress will assist the relaxation of the cluster of atoms with a volume of V, and the rate of the relaxation under the local shear stress τ can be expressed as

$$v = \alpha v_0 \cdot e^{-E_g / k_B T} \sinh\left(\frac{\tau V}{k_B T}\right), \tag{3.4}$$

where α is a factor related to the shape of the cluster of atoms. If $\tau V >> k_B T$, the rate of relaxation can be rewritten as

$$\nu = \alpha \nu_0 \cdot e^{-(E_g - \tau V)/k_B T} = \alpha \nu_0 e^{-E_0/k_B T} . \tag{3.5}$$

Based on Eq. (3.5), the activation energy $E_g = 1.98$eV is obtained by extrapolating the linear relation between $E_0(\tau)$ and the shear stress τ, as shown in Figure 3.7. The activation volume is thus calculated as $V = 0.135$ nm^3. It should be noted that due to the accuracy limitation of DMA and the influence of environment, the calculated activation energy would tend to be scattering. Therefore, for accurately calculating the defect size, each activation energy value in Figure 3.7 is the result of an average of several experimental tests.

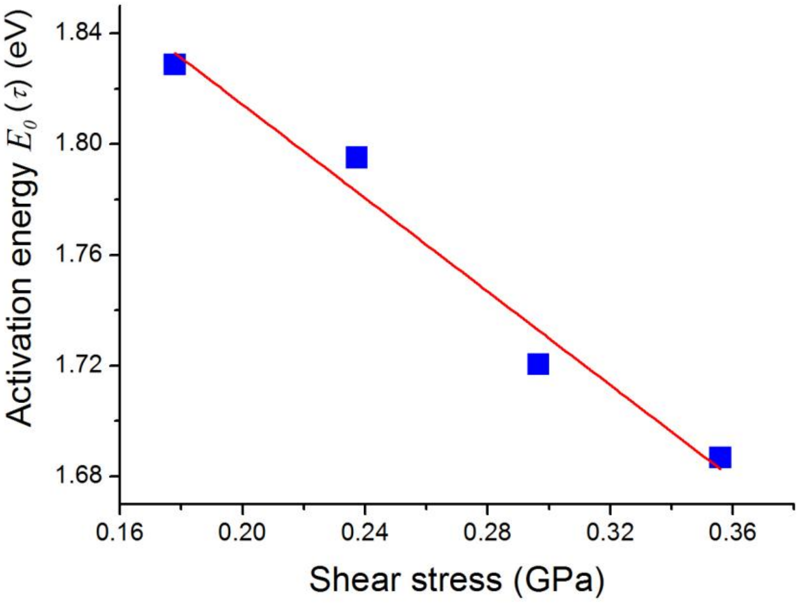

Figure 3.7 Fitting of activation energy $E_0(\tau)$ of as-synthesized samples with different pro-loading tensile stresses.

$Pd_{73}Si_{20}Cr_7$ sample relaxed at 533K for 20 hours is selected as the reference to study the structural activation. As shown in Figure 3.8, with larger shear stress τ, the maximum activation energy $E_0(\tau)$ decreases and the peak shifts towards a lower temperature. The results show that T_g decreases with increasing applied stress. Based on Eq. (3.5), the activation energy $E_g = 2.72$ eV is fitted as a linear function with the shear stress τ as shown in Figure 3.9. The activation volume is thus calculated as $V = 0.145$ nm^3, which is slightly larger than the as-synthesized sample with $V = 0.135$ nm^3.

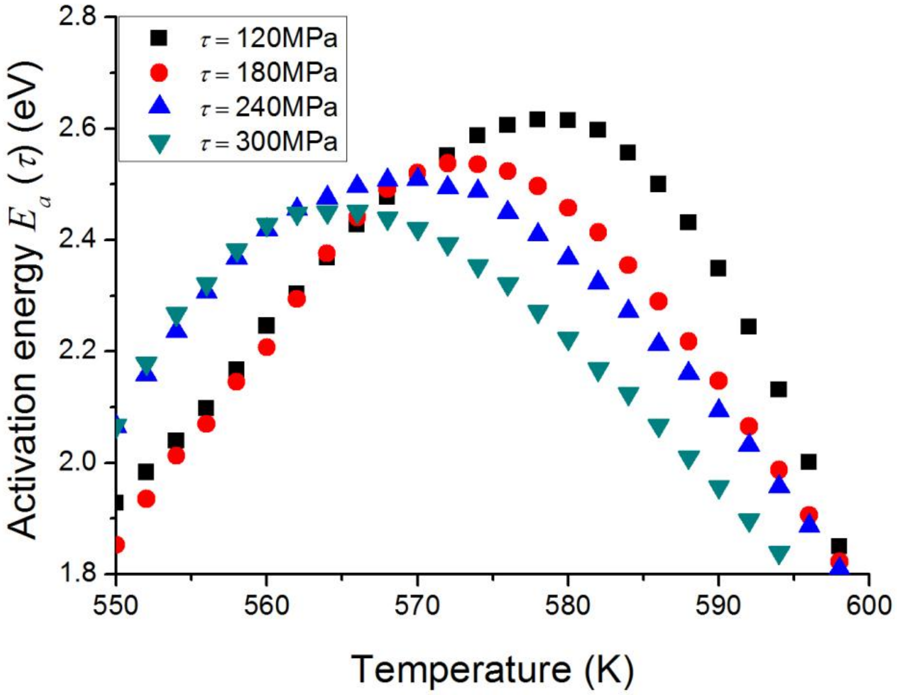

Figure 3.8 The activation energy of $Pd_{73}Si_{20}Cr_7$ samples annealed at T_a = 533 K under different pro-loading tensile stresses. The heating rate is 0.6K/min.

Table 3.2 Characteristics of glass transition of $Pd_{73}Si_{20}Cr_7$ samples after annealing at 533K with different pro-loading tensile stresses ($\dot{T}$=0.6K/min)

Shear stress	**120MPa**	**180MPa**	**240MPa**	**300MPa**
E_0 (τ) (eV)	2.62	2.56	2.51	2.45
T_g (K)	578	573	569	564

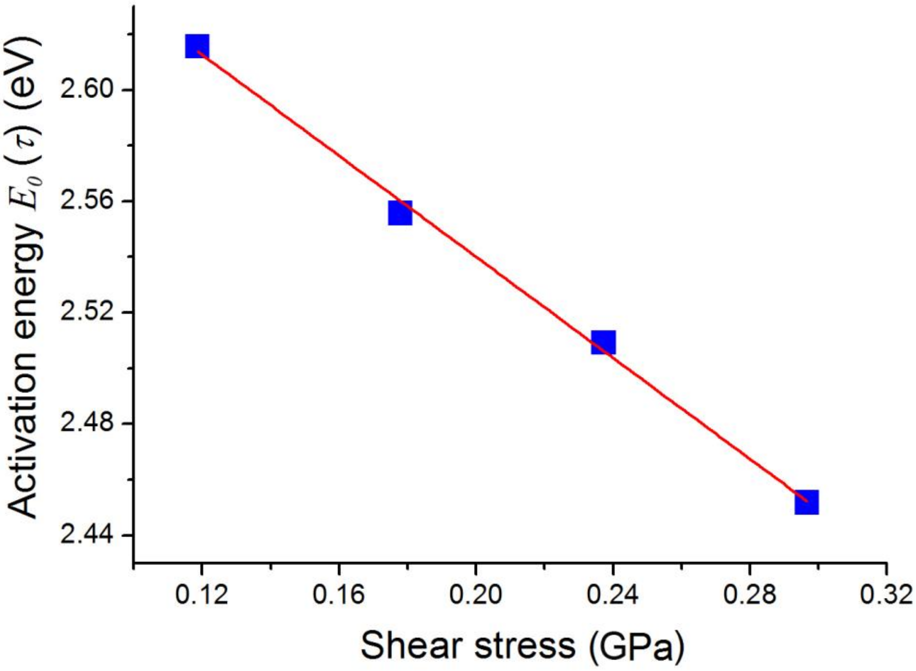

Figure 3.9 Activation energy $E_0(\tau)$ of samples annealed at T_a = 533K with different pro-loading tensile stresses.

3.2.4 Index *n* of internal friction

As described in Chapter 2 internal friction is an important parameter to describe the features of structural variation of materials. For metallic glasses, internal friction is used to illustrate structural relaxation as described in Section 3.2.2 and 3.2.3. However, internal friction is a parameter combining several components during the testing process (Bidaux, Schaller et al. 1989). With strong background from the general matrix of the material, some features of nano-scale structural changes of defects can not be identified in the internal friction. Therefore, a new parameter deduced from the internal friction should be sought to manifest the local structural change with better accuracy.

Some models proposed in previous studies have demonstrated the internal friction at low frequencies scales with dynamic frequency as

$$Q^{-1} \propto \omega^{-1}, \tag{3.6}$$

where $\omega = 2\pi f$, f is the measuring frequency. Although the linear relation between Q^{-1} and $1/f$ is observed in some crystalline materials (Wang and Fang 2001) as well as some bulk metallic glasses (Khonik 2001; Zhang, Zu et al. 2002), Cai *et al.* (Cai, Shang et al. 2004) reported a nonlinear relation for bulk $Zr_{65}Cu_{17.5}Ni_{10}Al_{7.5}$ as

$$Q^{-1} \propto \omega^{-n}, \tag{3.7}$$

where n is a constant with $0<n<1$. This nonlinear relation between Q^{-1} and $1/f$ is very important to understand the mechanism of relaxation in metallic glasses, and the index n is a microstructure-sensitive parameter of metallic glasses. Hence, through analyzing the variation of this parameter, information about defect variation in metallic glasses can be obtained. Moreover, information about microstructure change due to glass transition can be further revealed, since internal friction is closely related to the rapidly changing viscosity of the glassy solid in the supercooled liquid state around T_g.

As shown in Figure 3.2, internal frictions (IFs) with different testing frequencies are a constant value below 380K for all the specimens, following by significant increases which are frequency dependent. The temperature T_r, at which the deviation occurs can be obtained from IF spectrum as 368K, 398K, 418K and 456K for as-synthesized $Pd_{73}Si_{20}Cr_{7}$, and $Pd_{73}Si_{20}Cr_7$ annealed at T_a = 423K, 473K and 543K, respectively. The logarithmic relation between the internal friction and the frequency is plotted in Figure 3.10. The slopes of all the fitting lines are nearly zore at temperature below T_r, following by the increase to a constant with increasing temperature. Good linearity can be discovered for $\ln Q^{-1}$ verse $\ln\omega$, especially for $T>T_r$.

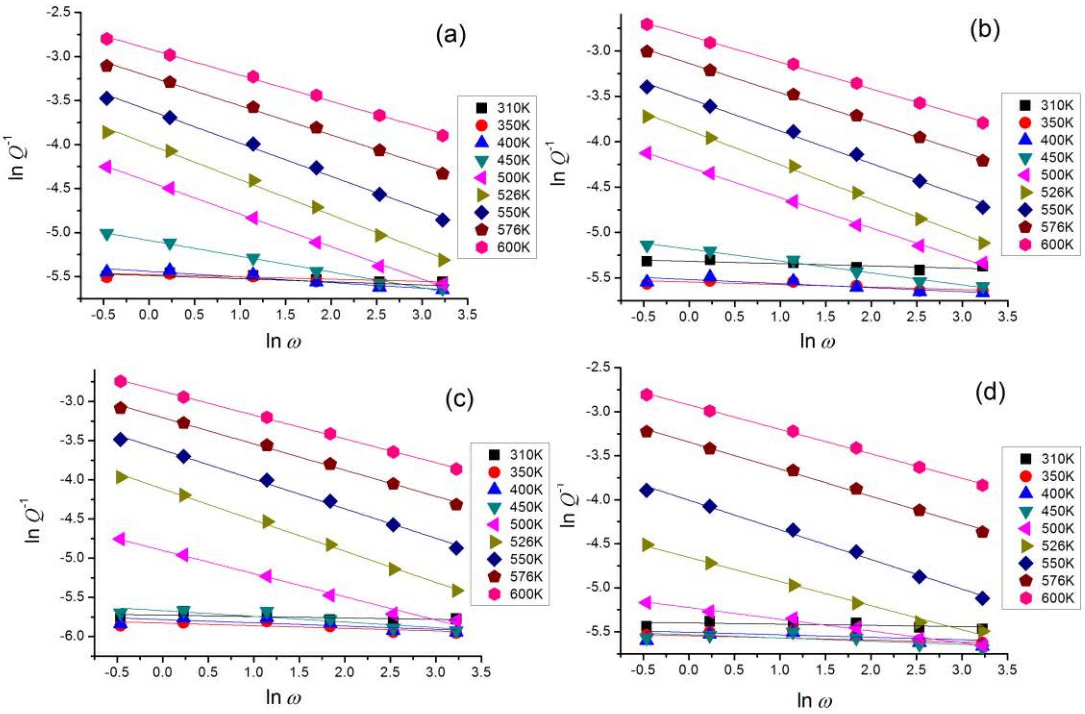

Figure 3.10 Logarithmic relation between the internal friction and frequency in Figure 3.2 for (a) as-synthesized $Pd_{73}Si_{20}Cr_7$, and (b)-(d) $Pd_{73}Si_{20}Cr_7$ after structural relaxation at T_a = 423 K, 473 K and 543 K, respectively.

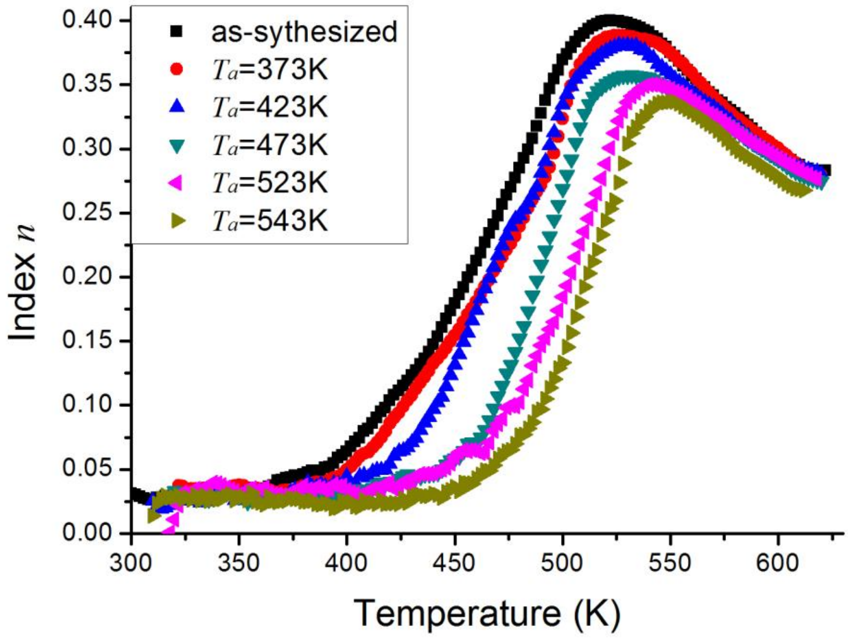

Figure 3.11 Index n for the as-synthesized $Pd_{73}Si_{20}Cr_7$ and those annealed at different T_a.

The index n of internal friction for samples annealed at T_a is shown in Figure 3.11. The significantly increases of index n for samples with different T_a occur at temperatures T_r. Index n achieves a maximum at a temperature between 523K and 548K depending on the degree of relaxation (or relaxation temperature T_a). Sample with higher T_a shows a smaller maximum value of n at higher temperature. However, the index n tends to be a constant n~0.28 at around 580K.

3.3 Structural configuration of metallic glasses related with as-synthesized defects

3.3.1 Atomic rearrangement due to thermal treatment

$Pd_{73}Si_{20}Cr_7$ ribbons annealed at different temperatures show different internal frictions as shown in Figure 3.2. This variation is directly related to different degrees of structural relaxations of defects in metallic glasses after thermal treatment. For the as-synthesized metallic glass, rapid solidification from the melting liquid phase inevitably introduces defects into the ideal glassy matrix, keeping them in non-equilibrium states. Furthermore internal stress would be retained in the structure as the atoms are quickly frozen due to rapid quenching. Therefore, long time annealing at certain temperature would lead to the transformation from an as-synthesized non-equilibrium state to a relatively more ideal or prefect state of glass by annihilation of the defects or dissipation of the internal residual stresses. This process could be also considered as the transition from loose-bonded atomic clusters to stable clusters with tight bonding, which is ideal glassy state in metallic glass (Fan, Liaw, et al. 2009). It has been indicated by previous researches that sub-T_g internal friction features can be affected by inhomogeneous deformation, subsequent annealing and electron irradiation (Khonik and Spivak 1996). All of these stimulations would change the atomic structure and further alter the overall mechanical properties. Therefore information we obtained from the internal friction measurements could be used to understand the nature of defects in metallic glasses.

Below 420 K, all the internal frictions shown in Figure 3.3 almost overlap with each other. A shoulder in internal friction can be detected for sample with T_a = 373 K as well as the as-synthesized sample. This shoulder of internal friction may relate with the internal stress dissipation, which would accompanied by slight rearrangement of local atomic structure in the matrix. However, the thermal kinetic energy at 373K is not large enough to fully dissipate the internal stresses in metallic glass. As annealing temperature increases, atoms in metallic glass would self-adjust their positions and dissipate the internal stresses due to chemical short-range order (CSRO) in metallic glasses. Eventually the shoulder would be unapparent in the internal friction for sample annealed at higher temperature T_a > 423 K as shown in Figure 3.3.

There are significant differences in internal frictions at T > 550 K of samples with $T_a \leq$ 473 K and those of samples annealed at T_a = 543 K, as shown in Figure 3.3. Because the annealing of sample at sub-T_g would promote defect annihilation in the metallic glass, therefore different non-equilibrium states would be formed corresponding to different degrees of structural relaxation. For T_a = 543 K, the corresponding structural relaxation process may be essentially related to topological short-range order (TSRO), which involves a relative long range rearrangement of all the atoms. If the annealing temperature is T_a > 543 K, atomic movement is not limited in the short range, and additional atomic rearrangement in a much broader range would take place (Dmowski, Fan et al. 2007).

3.3.2 Change of energy configuration

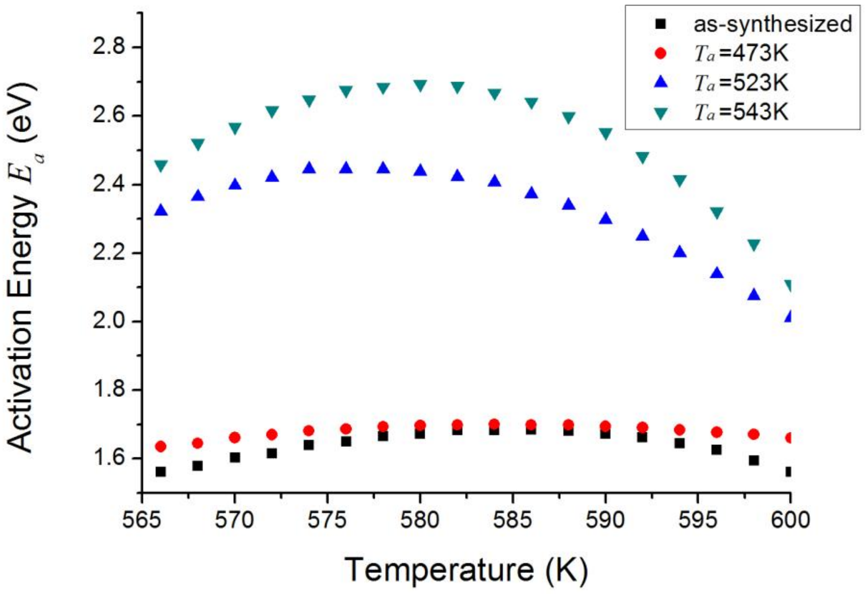

Figure 3.12 Activation energy of $Pd_{73}Si_{20}Cr_7$ samples annealed at different T_a for 20 hours.

The activation energy of $Pd_{73}Si_{20}Cr_7$ samples annealed at different temperatures is shown in Figure 3.12. The maximum of the activation energy E_0 of all the annealed samples as well as the as-synthesized sample are shown in Figure 3.13. Activation energy would keep as a constant E_0 = 1.75 eV until the temperature T_a reaches 500 K. Activation energy of glassy state would increase dramatically for T_a >500K, and E_0 = 2.70 eV will be achieved for the annealing temperature T_a = 543 K. The increase of activation energy with increasing relaxation temperature could be caused by the structural relaxation induced formation of lower energy state as valley “C” representing in Figure 3.14, showing that extra energy $\Delta E = E_g' - E_g$ is required for structural activation.

For annealing temperature lower than 473 K, the activation energy E_0 is nearly no change: E_0 = 1.75 eV. As mentioned above, this relaxation well below T_g is mainly related to CSRO. Since such structure change only occurs in the neighboring chemical environment as internal stress releases. This CSRO change in metallic glass does not change its overall energy configuration and slightly affects activation related to glass transition. As annealing temperature T_a increases, long-range rearrangement of all the atoms will be triggered. The kinetics at elevated T_a could drive atoms with much higher mobility for atomic rearrangement. Because further stable energy configuration is achieved after structural relaxation, the resulting activation energy E_0 would increase with T_a.

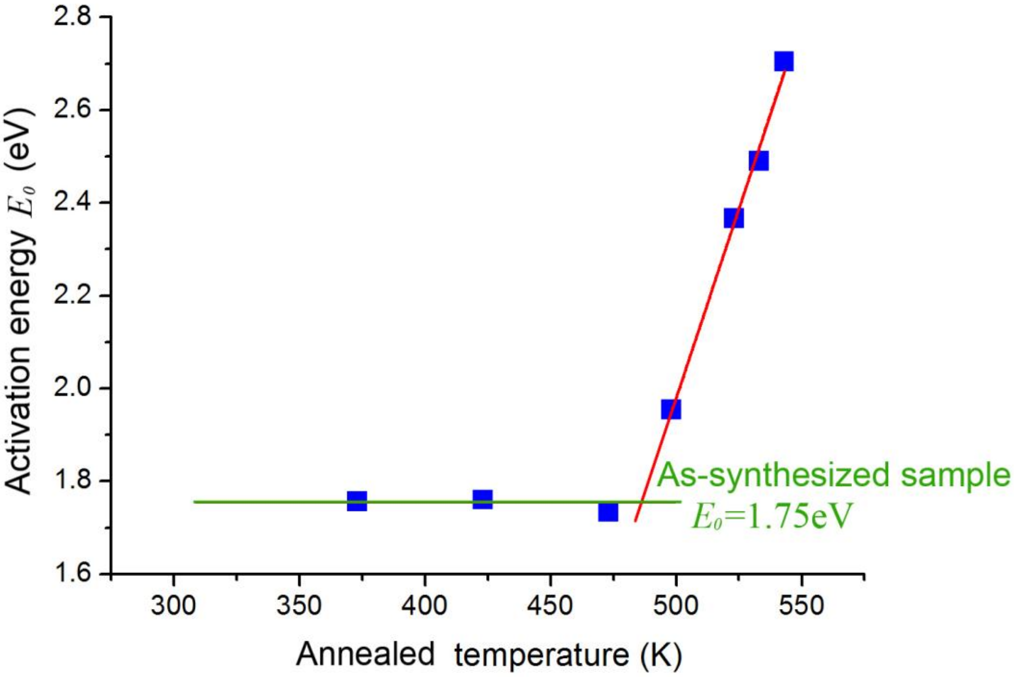

Figure 3.13 Activation energy of samples after annealing at different temperatures.

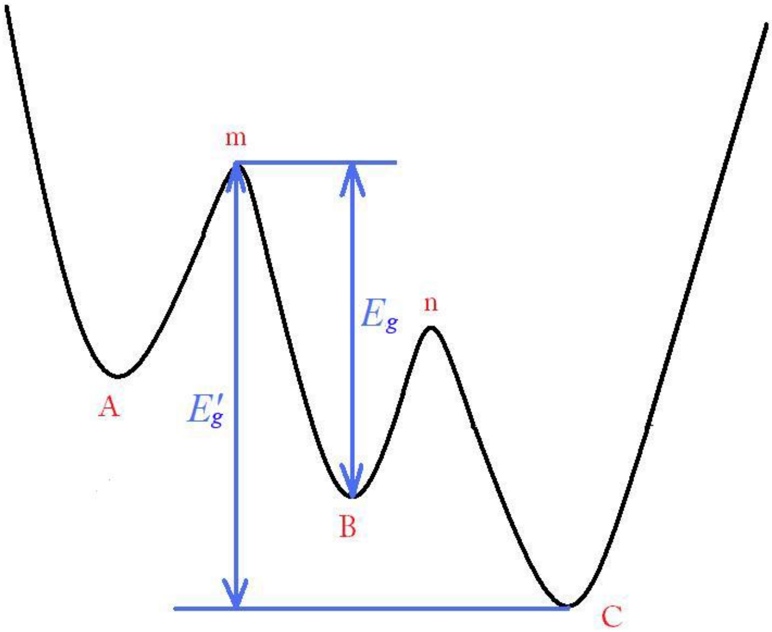

Figure 3.14 Schematics of energy state in metallic glass, where valley “A” represents high energy state after activation, valley “B” represents the initial state of as-synthesized materials before activation, and valley “C” represents energy state after long time relaxation at temperature below T_g. Saddle point “m” is an absolute energy point to be conquered for system activation, while saddle point “n” is an absolute energy point to be conquered for system relaxation.

3.4 The roles of defects in structural relaxation

3.4.1 Reversible structural relaxation described by index *n*

To characterize the structural variation using index *n*, the relations among index *n* at T_g and viscosity are analyzed for different metallic glasses such as $Pd_{82}Si_{18}$, $Al_{85}Ni_{10}Ce_5$, $(Ce_{0.72}Cu_{0.28})_{85}Al_{10}Fe_5$, and $Zr_{41.2}Ti_{13.8}Cu_{12.5}Ni_{10}Be_{22.5}$. Glass transition temperature T_g is determined by DSC.

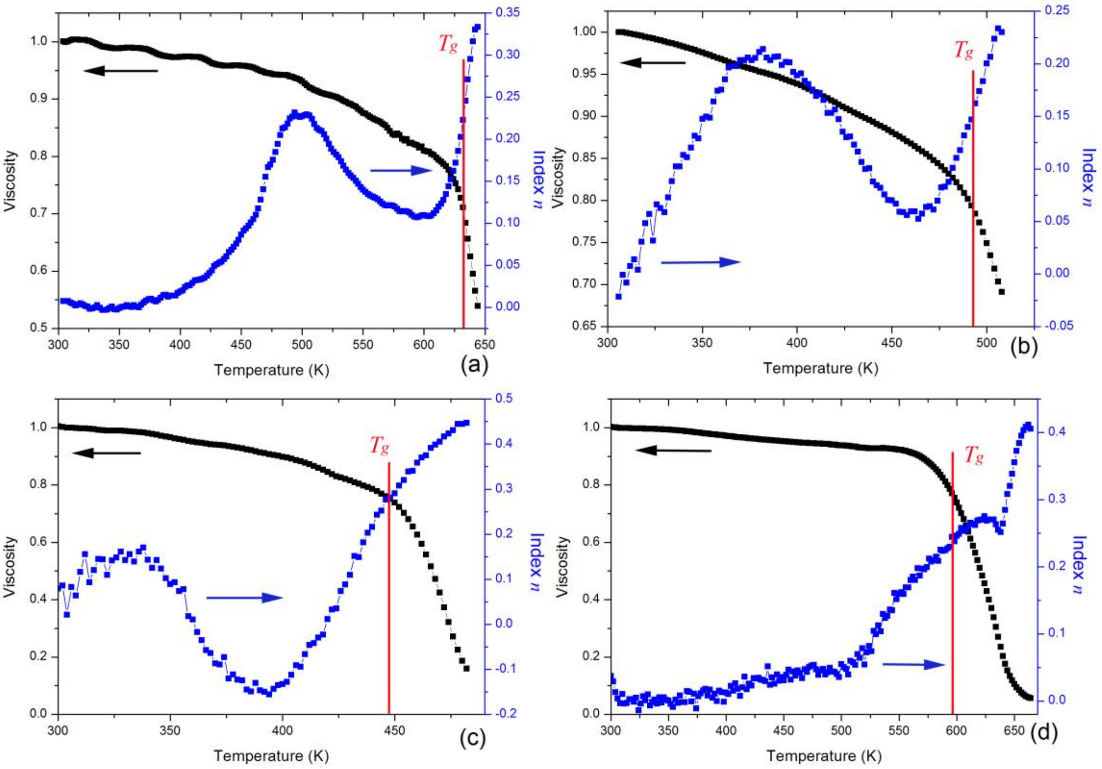

Figure 3.15 Index *n* and normalized viscosity vs temperature for metallic glasses: (a) $Pd_{82}Si_{18}$, (b) $Al_{85}Ni_{10}Ce_5$, (c) $(La_{0.624}Ce_{0.156}Ni_{0.22})_{75}Al_{25}$ and (d) $Zr_{41.2}Ti_{13.8}Cu_{12.5}Ni_{10}Be_{22.5}$. Glass transition temperature T_g is marked with red line. The heating rate is 0.3K/min.

The peaks of index *n* can be observed for $Pd_{82}Si_{18}$, $Al_{85}Ni_{10}Ce_5$, and

$(La_{0.624}Ce_{0.156}Ni_{0.22})_{75}Al_{25}$ as shown in Figure 3.15, which may relate to the reversible slow β relaxation which is considered as localized translational motions of a cluster of atoms within the elastic matrix confinement (Harmon, Demetriou et al. 2007). For better explanation, internal friction spectrums of these samples are all plotted in Figure 3.16, highlighting β relaxation feature as magnified in the insets. Although there is no typical β relaxation for $Pd_{82}Si_{18}$, the higher the testing frequency, the more significant increase of internal friction as shown in Figure 3.16 (a). Apparent β relaxation can be observed in $Al_{85}Ni_{10}Ce_5$ as shown in Figure 3.16 (b). As shown in Figure 3.16 (c), $(La_{0.624}Ce_{0.156}Ni_{0.22})_{75}Al_{25}$ shows a typical β relaxation between 300 K and 420 K, where the relaxation peak shifts to higher temperature with increasing frequency. Remarkably, these temperature ranges for β relaxation as shown in Figure 3.16 are the same as those of the peaks of index n as shown in Figure 3.15. For most metallic glasses, it is difficult to detect β relaxation from internal friction testing. For example, as shown in Figure 3.2, no peak can be detected from DMA testing. The explanation for this is that severe α relaxation would overwhelm β relaxation whose characteristic temperature is close to T_g. The maximum value of index n can be an effective and sensitive criterion to characterize β relaxation in metallic glasses. Based on the definition of index n, the features of β relaxation, *i.e.*, shifting of peak temperature with increasing testing frequency, always result in the peak of index n as shown in Figure 3.11 and 3.15, regardless of no apparent relaxation peak in the internal friction. Therefore, index n is quite sensitive to the β relaxation process and could reveal structural variation in metallic glasses which can not be obviously

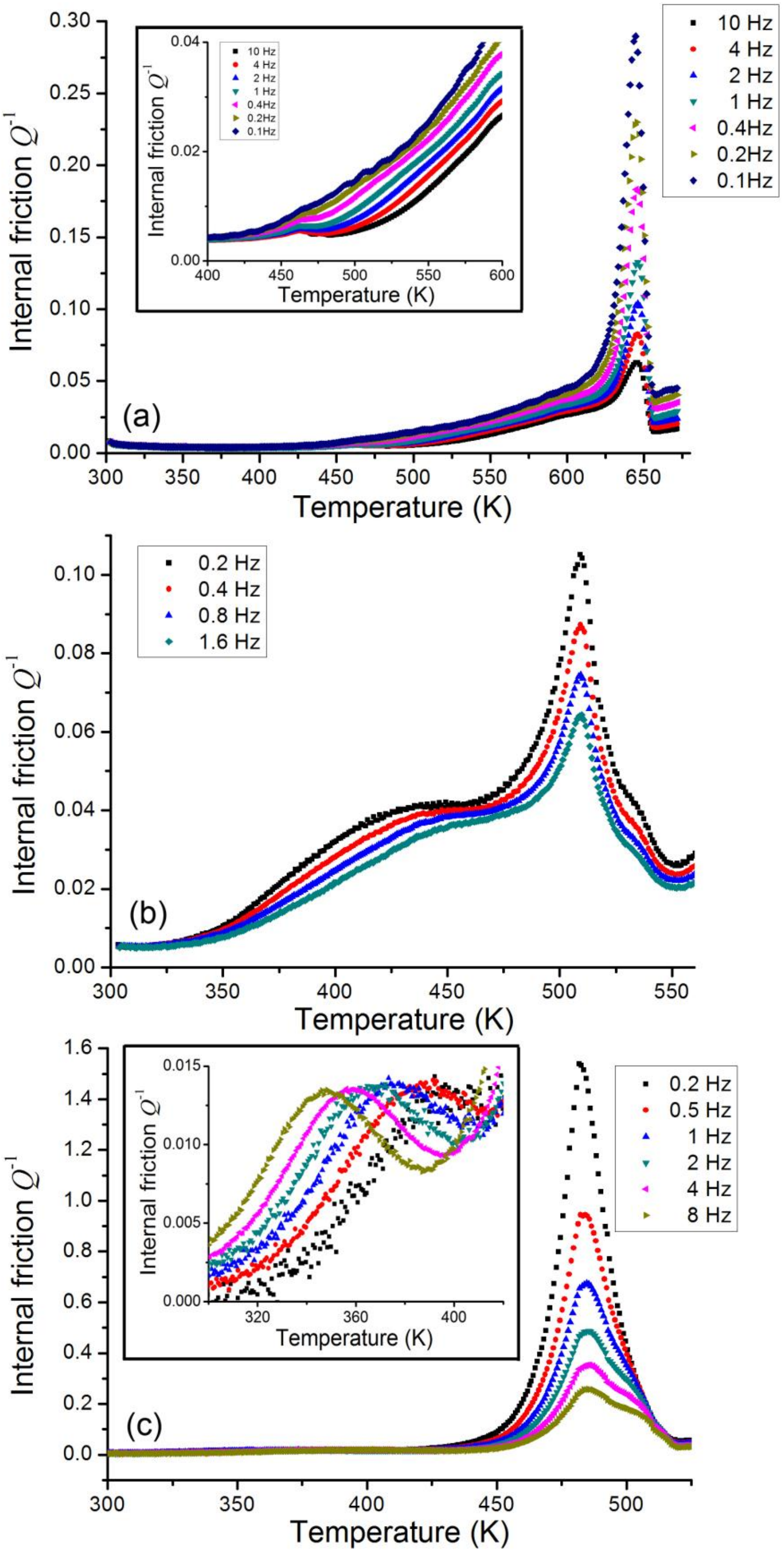

Figure 3.16 Internal friction of (a) $Pd_{82}Si_{18}$, (b) $Al_{85}Ni_{10}Ce_5$, and (c) $(La_{0.624}Ce_{0.156}Ni_{0.22})_{75}Al_{25}$. β relaxation feature is magnified in the insets.

detected by IF.

The sensitivity of index n would come from the microstructure variation, which alters the coupling strength between the oscillating stress and local response. This coupling factor a is closely related with frequency ω. Thus the harmonic force ΔF^{dyn} arising from forced oscillation during the IF measurement under the dynamic load $\sigma_A\sin(\omega t+\delta)$ can be written as (Zhang, Fung et al. 1995)

$$\Delta F^{\mathrm{dyn}} = a\,(\omega)\sigma_A\sin(\omega t+\delta). \tag{3.8}$$

The motion of atomic clusters around defects can be described as

$$\rho\ddot{x} + \gamma\dot{x} + kx = \Delta F' + \Delta F^{\mathrm{dyn}}, \tag{3.9}$$

where ρ is the average mass density around the defects, γ is the effective damping coefficient, which can be described as function of viscosity η as $\gamma = 2\eta\rho$, k is the dynamic restoring coefficient arising around defects, and k/ρ is the square of the resonant frequency ω_0 during structural relaxation, $\Delta F'$ represents the thermal driving force for structural relaxation. Therefore, Equation (3.10) can be further described as

$$\ddot{x} + 2\eta\dot{x} + \omega_0^2 x = f(t). \tag{3.10}$$

On the other hand, the dissipation of vibration energy due to structural relaxation per cycle of oscillation per unit volume of the specimen can be expressed as

$$\Delta W = N_a \int_0^p \Delta F^{dyn} \dot{x} dt, \tag{3.11}$$

where p is the period of oscillation, N_a is volume density of relaxation centers. Based on the definition of internal friction in Eq. (2.1), we have

$$Q^{-1} = \frac{\Delta W}{2\pi W} = N_a \int_0^p \Delta F^{dyn} \dot{x} dt / (\pi\sigma^2/\mu), \tag{3.12}$$

where μ is the modulus of sample, while W is the maximum kinetic energy input from the vibration. When there is a relation $Q^{-1} \propto \omega^{-n}$ as confirmed by experiments, the dissipation of vibration energy ΔW, and further the harmonic force ΔF^{dyn}, would closely relate with the index-n in Eq. (3.7). Therefore, in Eq. (3.8), the coupling factor a can be rewritten as a (ω^n), where index n is an important factor indicating internal structural variation. Internal friction would become more divergent with different frequencies under intensive structural change, such as β relaxation, which can be reflected as the increase of index n. According to Eqs. (3.9) and (3.10), index n is also related with viscosity η. Thus, index n would also be sensitive to the structural relaxation such as glass transition.

3.4.2 Irreversible structural relaxation of defects

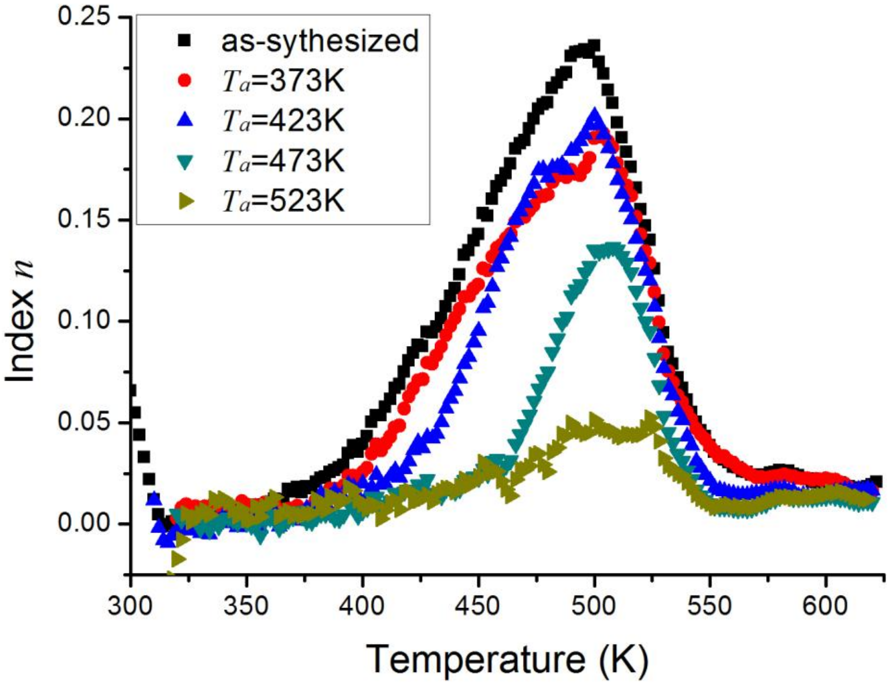

Figure 3.17 Subtracted index n for specimen annealed at T_a. The background index-n curve is with the sample annealed at T_a=543K as shown in Figure 3.11.

As discussed in Section 3.3, variation of internal friction for samples with different T_a is directly related to the degree of structural relaxation of metallic glasses after thermal treatment. This structural relaxation can be considered as the process of defect annihilation, leading to more ideal glassy matrix. n is also an important parameter for structural relaxation about defect annihilation. Since index n is a microstructure-sensitive parameter, any microstructure variation can be accurately illustrated. Therefore, we could use index n to characterize the sub-T_g structural relaxation which is irreversible.

This sub-T_g structural relaxation can be better described by subtracting the index-n curve in Figure 3.11 with that of sample annealed at T_a = 543K. The subtracted index n is shown in Figure 3.17. Peaks can be observed in these curves. The peak height decreases with T_a, while the peak temperature T_{pk}' increases with increasing T_a. As mentioned above, this feature would come from structural relaxation. Atomic arrangement causes transformation of the defected area to the ideal glass, which during reheating reduces the intensity of structural change. We may define these defective atomic clusters relating with such irreversible structural relaxation as initial defects or as-synthesized defects, since this structural heterogeneity comes from the rapid quenching and would be removed or reduced through thermal annealing at sub-T_g.

3.4.3 Index *n* for glass transition

Obviously, the sub-T_g structural relaxation as characterized by the peak of index n as shown in Figure 3.17 is an irreversible process. The subtracted index-n curve above 575K in Figure 3.17 tends to zero, and absolutely n ~ 0.28 can be obtained in Figure 3.11. Since T_g ~ 575K with $\dot{T}$ = 0.6 K/min for $Pd_{73}Si_{20}Cr_7$, the matrix of the sample would be in the same supercooled liquid state after the glass transition occurs. The glass transition temperature T_g= 575K or n ~ 0.28 can be further verified through plotting the relation between index n and viscosity as shown in Figure 3.18. Viscosity of $Pd_{73}Si_{20}Cr_7$ would significantly decrease above T_g, with the corresponding index n

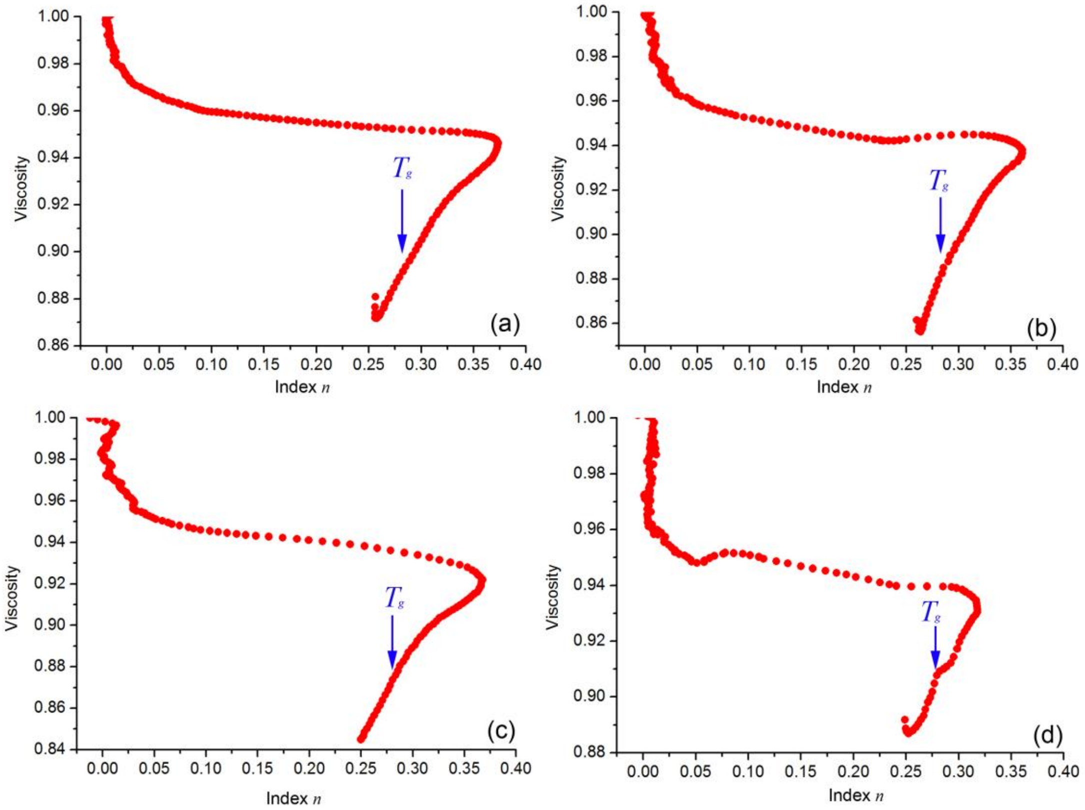

Figure 3.18 Index-*n* verse normalized viscosity for (a) as-synthesized $Pd_{73}Si_{20}Cr_7$, and (b)-(d) $Pd_{73}Si_{20}Cr_7$ after structural relaxation at T_a = 423 K, 473 K and 543 K, respectively. The arrows show the corresponding temperatures at which the glass transition occurs.

nearly unchanged in samples with different T_a. Therefore we could define 0.28 as the indication of glass transition. From Figure 3.18, it can be found that fully supercooled liquid (viscosity close to zero) can not be formed for $Pd_{73}S_{i20}Cr_7$ due to its poor glass forming ability and crystallization would happen as temperature is slightly higher than T_g. Thus the viscosity of $Pd_{73}S_{i20}Cr_7$ would only drop about 12%.

For metallic glasses $Pd_{73}Si_{20}Cr_7$, the index *n* is 0.28 when glass transition happens, which is quite close to those around 0.25 for $Pd_{82}Si_{18}$, $(La_{0.624}Ce_{0.156}Ni_{0.22})_{75}Al_{25}$, and $Zr_{41.2}Ti_{13.8}Cu_{12.5}Ni_{10}Be_{22.5}$ sample. This similarity in index *n* at T_g may come from the equivalent supercooled liquid state for all the metallic glasses. Glass transition would lead to the collapse of atomic structure of glass and larger scale rearrangements of atoms would be activated. The viscous liquid of each metallic glass above T_g would has similar kinetics since atoms in liquid have weak interactions with each other. Therefore, the index n is similar at T_g for various metallic glasses.

3.5 Conclusions

Atomic CSRO and TSRO rearrangements in metallic glasses are illustrated through dynamic mechanical analysis or internal friction studies. Metallic glasses after thermal annealing at different temperatures show different energy configurations which represent different degrees of structural relaxation due to thermal treatment. Structural relaxation would also be affected by external loading. More stable states that are archived through irreversible structural relaxation can be considered as a process of annihilation of defects which come from rapid quenching in the idea glassy matrix.

Characterization of structural relaxation can be achieved by using index n, a scaling exponent of internal friction. Irreversible structural relaxation, slow β relaxation and primary α relaxation show different features with index n. Annealing at sub-T_g would cause irreversible structural relaxation which annihilates defects generated from rapid quenching and change the glassy matrix into ideal glassy states. This irreversible structural relaxation is different from the reversible β relaxation, which is a universal feature of metallic glasses occurring through the relaxation of confined atoms. It is found a maximum index n is associated with the β relaxation. Above T_g, α relaxation occurs, which induces the transformation from glass to supercooled liquid. Similar index n of 0.25 is found to be associated with α relaxation.

Defects discussed in this chapter are caused by rapid quenching, which have been shown to have a close relation with structural relaxation in metallic glasses. In addition, defects in metallic glasses can be sources for plastic deformation, which govern the mechanical properties of metallic glasses. These deformation defects will be studied in next chapter.

4. Internal friction study of deformation defects in metallic glasses

4.1 Introduction

The exact nature of local atomic motion under shear stress in the metallic glasses is an essential issue which is not fully resolved (Schuh, Hufnagel et al. 2007; Chen 2008). It is considered that the fundamental deformation process is a local rearrangement of atoms under shear stress (Delogu 2011). Therefore, the atomic configuration of metallic glasses and its local topography are essential factors for the plastic deformation. Several models have been suggested to describe the deformation mechanisms of metallic glasses. As an explanation of homogeneous deformation of metallic glasses, free volume model proposed by Spaepen (Spaepen 1977) is used to describe the mechanical properties of metallic glasses (Dai, Yan et al. 2005; Yu, Bai et al. 2007; Song and Nieh 2009). Murali and Ramamurty (Murali and Ramamurty 2005) detected a remarkable loss in impact toughness upon structural relaxation. They interpreted that the free-volume annihilation during sub-T_g annealing is the fundamental reason for such embrittlement. However, Slipenyuk and Eckert (Slipenyuk and Eckert 2004) pointed out that the free-volume model can only predict the trend of the free-volume density change, not the peculiarities of the structural relaxation. More recently Dmowski *et al.* (Dmowski, Iwashita et al. 2010) found that density of free-volume defects is not only 1% as proposed by free-volume model. Instead, they found around 1/4 of its total volume were defects. In particular, the local atomic structure of deformation defect is not fully understood which makes it difficult to further study the mechanism of plastic deformation, especially the localized plastic deformation or shear banding in metallic glasses.

The defects that are responsible for the plastic deformation of metallic glass can be the as-synthesized defects created through rapid quenching from liquid as discussed in Chapter 3. The deformation defects can be also created by shear deformation, which can be homogeneously distributed when the sample is deformed above $0.7T_g$. The creation of deformation defects through deformation of metallic glasses can be considered as a structural variation process from an ideal state to relatively poor glassy configurations. The plastic deformation of metallic glasses at the microscopic scales is essentially a biased accumulation of local strains incurred through the operation of deformation defects and the redistribution of these defects (Schuh, Hufnagel et al. 2007).

In this chapter, we will characterize both defect annihilation and creation in the metallic glass under shear deformation using dynamic mechanical analysis. It is well known that defects in crystalline solids such as point defects, dislocations, and grain boundaries all show apparent relaxation peaks in internal friction measurement. The deformation defects from crystalline solid, *i.e.* the dislocation, can be characterized by Bordoni peak (Marchesoni 1995) in the temperature-dependent internal friction. However, there is no peak apparently appearing in the internal friction measurement of metallic glasses, because of the influence of strong internal friction background from intensive atomic rearrangement such as glass transition and crystallization. Therefore, characterization of defects that are related with plastic deformation seems difficult without additional effort to analyze the internal friction results.

4.2 Experimental details

4.2.1 Tensile test

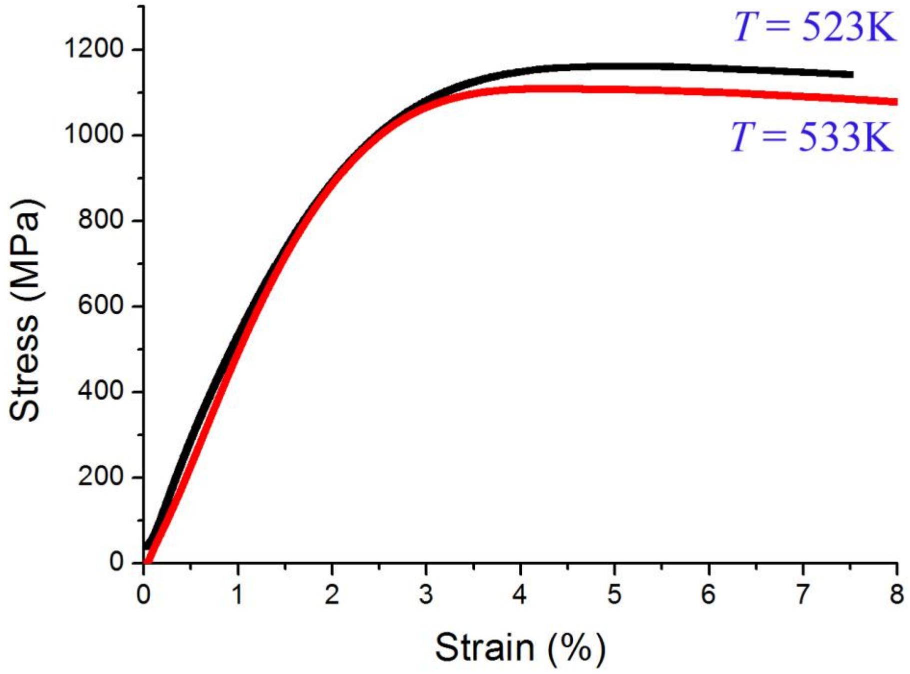

Figure 4.1 Tensile curves of metallic glass ribbon $Pd_{73}Si_{20}Cr_7$ at temperature of 523 K and 533 K with a strain rate of 10^{-4} min^{-1}.

The metallic glass ribbon $Pd_{73}Si_{20}Cr_7$ with 20 μm in thickness and 700 μm in width were deformed at temperature $T>0.7T_g$. The amorphous structure was examined in samples before and after plastic deformation by X-ray diffraction as shown in Figure 3.1 and Figure 4.2, respectively. We set the overall tensile strain to be 8% to make sure that sufficient homogeneous plastic deformation has occurred, at the same time fracture could be avoided. Figure 4.1 shows the tensile curves. To investigate the competition between defect creation by deformation and annihilation by thermal annealing, we investigated the plastic deformed $Pd_{73}Si_{20}Cr_7$ specimen with different strains of 4% and 12% respectively at the same temperature T = 523K with a strain rate of 10^{-4} min^{-1} as shown in Figure 4.3. To further investigate the competition between defect creation and annihilation, we studied tensile deformation behaviors of specimen under different annealing temperatures or strain rates as shown in Figure 4.1 and 4.4, respectively.

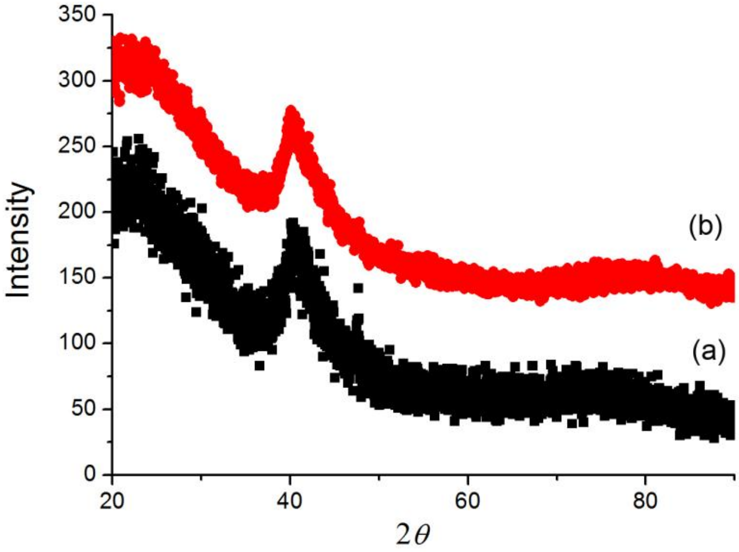

Figure 4.2 XRD pattern of plastically deformed $Pd_{73}Si_{20}Cr_7$ ribbon at (a) T_a = 523 K and (b) T_a = 533 K respectively. The strain rate is $10^{-4}min^{-1}$ for the deformation.

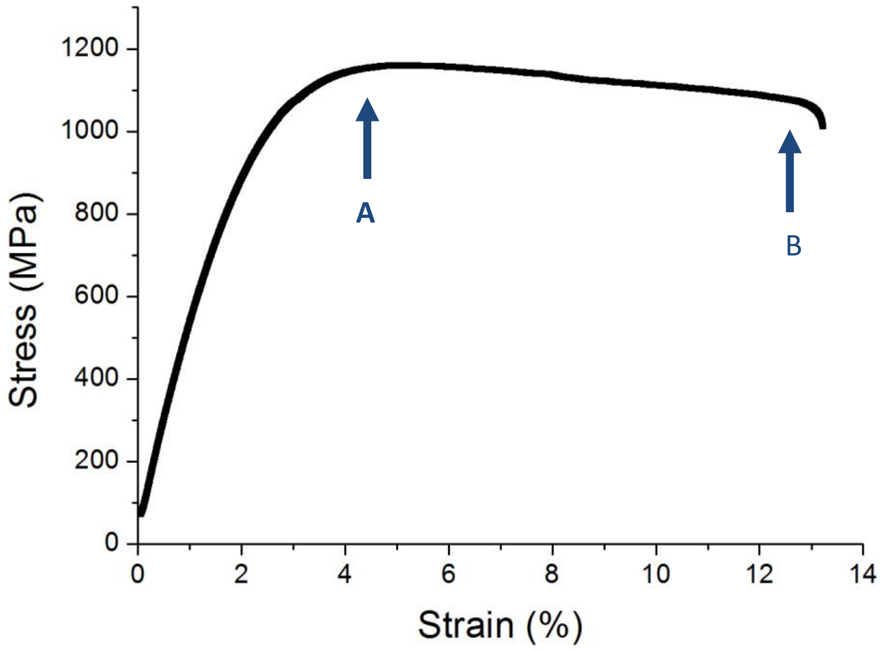

Figure 4.3 Tensile curve for metallic glass ribbon $Pd_{73}Si_{20}Cr_7$ at temperature of 523 K with a strain rate 10^{-4} min^{-1}. Tensile deformation would be stopped at A and B, where the tensile strain is 4% and 12% respectively.

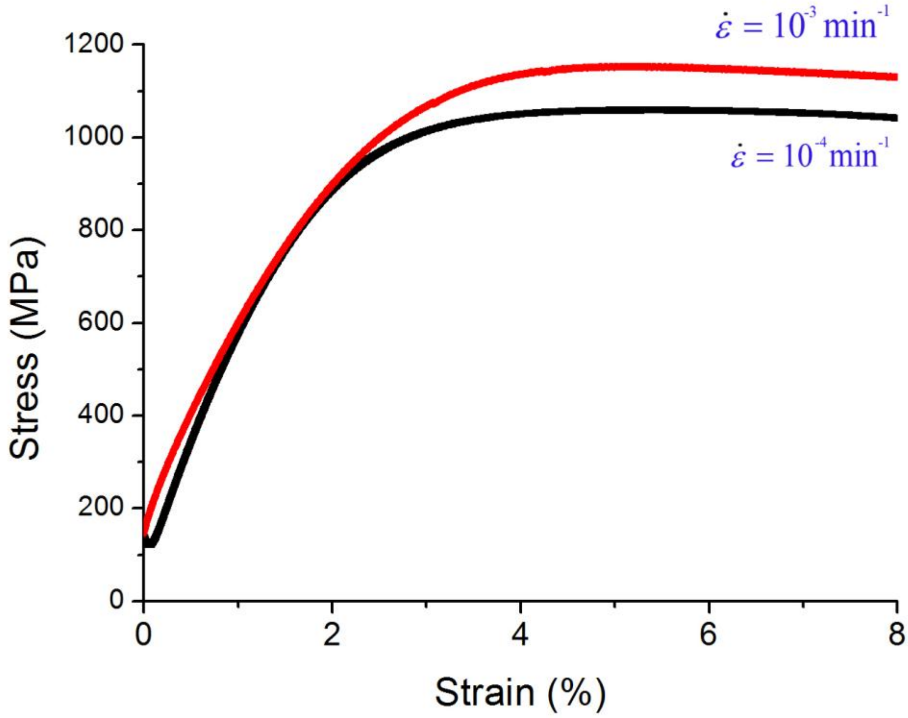

Figure 4.4 Tensile curve for metallic glass ribbon $Pd_{73}Si_{20}Cr_7$ at temperature of 543 K with strain rates 10^{-4} min^{-1} and 10^{-3} min^{-1} respectively.

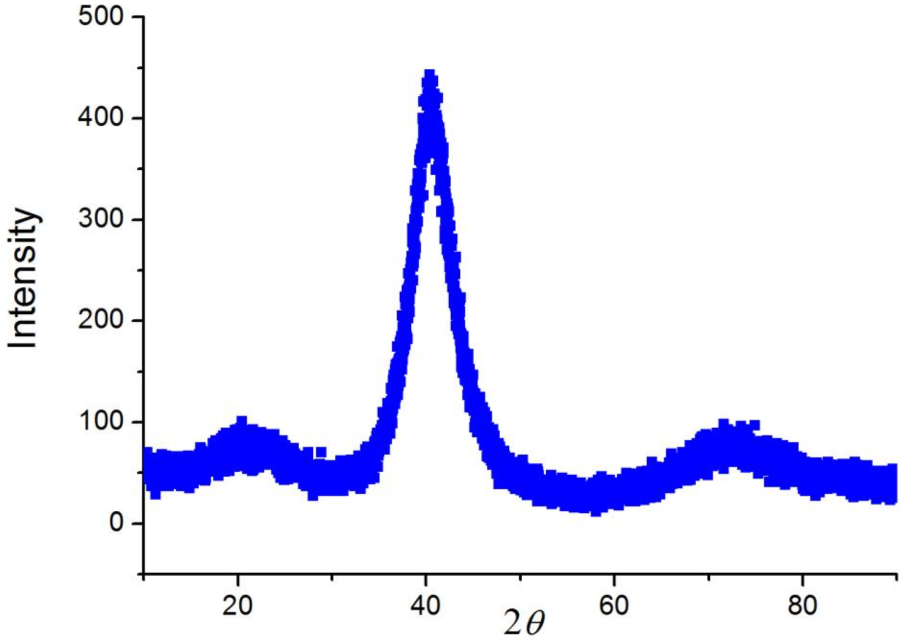

Figure 4.5 XRD pattern of as-synthesized $Pd_{82}Si_{18}$ ribbon.

The metallic glass ribbon $Pd_{82}Si_{18}$ was also processed by homogeneous plastic deformation. The XRD pattern in Figure 4.5 shows the amorphous nature of the as-synthesized sample. The tensile deformation was carried out at 583 K far below T_g = 648 K. Homogeneous plastic deformation occurs with strain rates 10^{-4} and 2.5×10^{-5} s^{-1} as shown in Figure 4.6. The samples were then rapidly cooled with liquid nitrogen once after the 5% total strain was achieved or fracture occured. All the samples after homogeneous plastic deformation were examined by X-ray diffraction to verify their amorphous structures as shown in Figure 4.7.

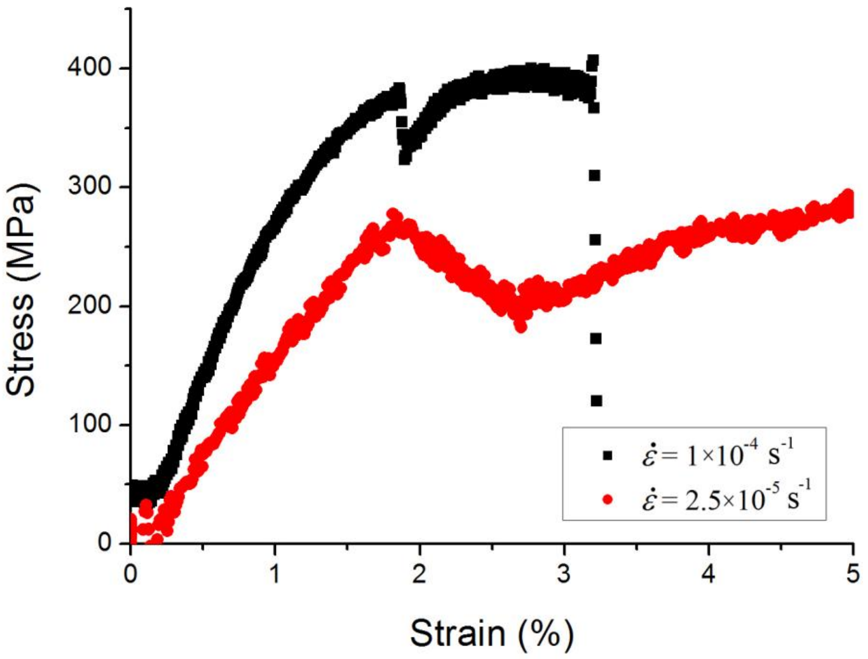

Figure 4.6 Tensile curves for metallic glass ribbon $Pd_{82}Si_{18}$ at 583 K with strain rates 10^{-4} s^{-1} and 2.5×10^{-5} s^{-1}.

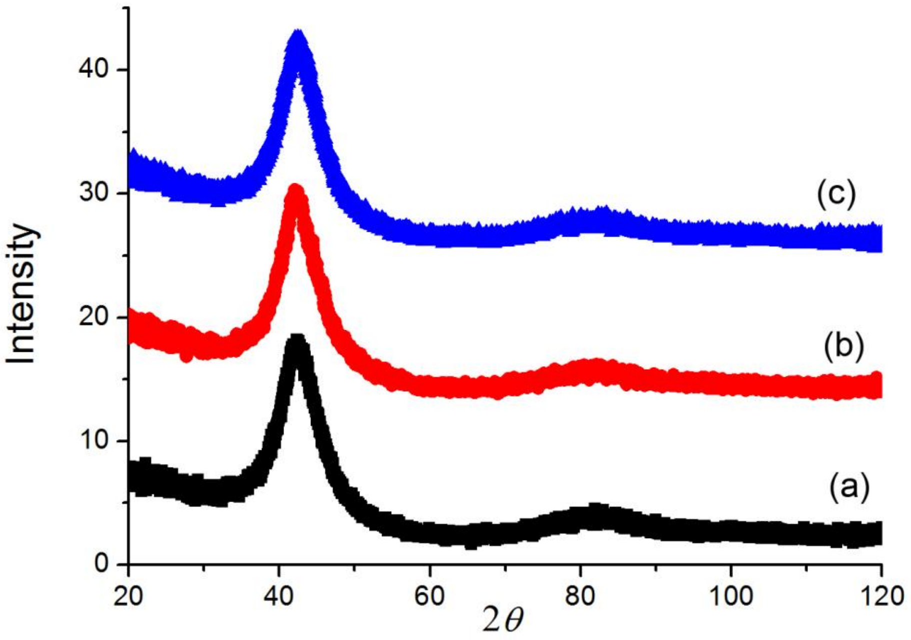

Figure 4.7 XRD pattern of $Pd_{82}Si_{18}$ (a) after plastic deformation at a strain rate of 10^{-4} s^{-1} and at T_a= 583 K ; (b) after plastic deformation at a strain rate 2.5×10^{-5} s^{-1} and at T_a=583 K; (c) after annealed at T_a=583 K without deformation.

4.2.2 Internal friction tests

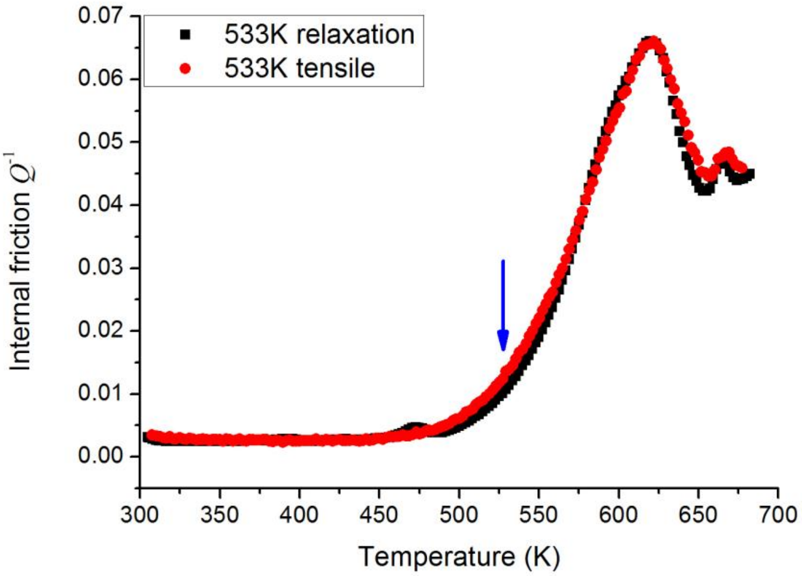

Figure 4.8 Internal friction of $Pd_{73}Si_{20}Cr_7$ samples with and without tensile homogenous deformation at 533 K. The testing frequency is 0.1 Hz, the heating rate is 0.6 K/min. The variation of internal friction curve marked by the arrow is considered to be related to defect creation.

The internal friction of $Pd_{73}Si_{20}Cr_7$ sample after 8% homogenous deformation at 533 K is shown in Figure 4.8, comparing with another specimen with identical thermal history but without any deformation, which is referred as a reference sample. Two samples have the same internal frictions at elevated temperatures before crystallization occurs, except for those in the temperature range between 480 K and 570 K. In this region, internal friction of specimen after 8% homogenous deformation at 533 K is slightly stronger than that of the reference one.

Similarly, internal friction of $Pd_{82}Si_{18}$ after 5% homogenous tensile deformation is compared with its reference sample as shown in Figure 4.9 (c). Difference in internal frictions of these two samples can be seen within the temperature range between 470 K and 570 K. Figure 4.9 (a) and (b) show the internal frictions at different testing frequency of the sample after 5% homogeneous deformation and its reference sample, respectively.

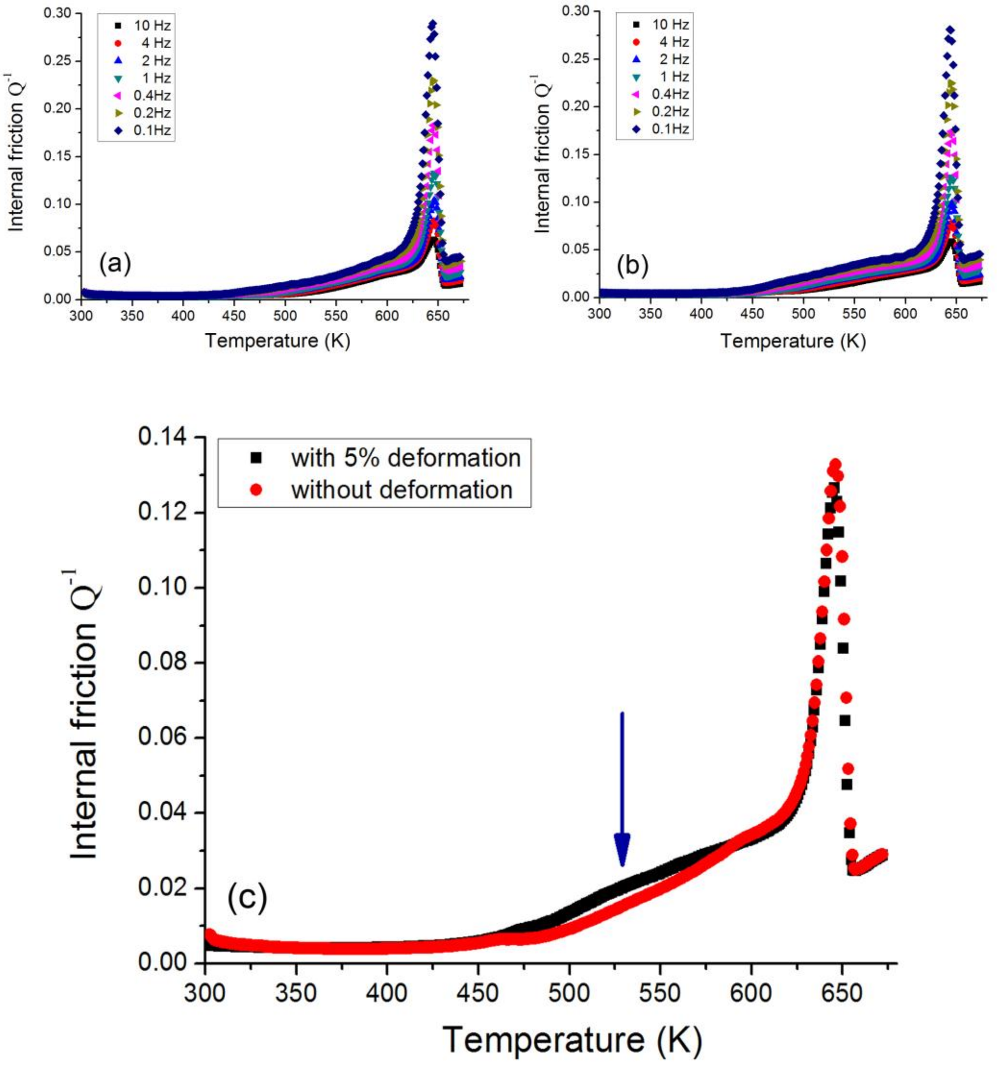

Figure 4.9 Internal friction of (a) Pd$_{82}$Si$_{18}$ samples after 5% homogenous tensile deformation under a strain rate 10^{-4} s^{-1}at 583 K. The heating rate is 0.3 K/min; (b) Reference Pd$_{82}$Si$_{18}$ sample. (c) Comparison of internal friction of two samples. The testing frequency is 1 Hz. The arrow is used to indicate the temperature region where annihilation of additional deformation defects occurs.

4.3 Deformation defects in metallic glasses

4.3.1 Structure variation after mechanical deformation

Table 4.1 Characteristics of glass transition of $Pd_{73}Si_{20}Cr_7$ samples after 8% homogenous tensile deformation at 533K with different pro-loading tensile stresses ($\dot{T}$=0.6K/min)

Stress τ	**120MPa**	**180MPa**	**240MPa**	**300MPa**
$E_0(\tau)$ (eV)	2.10	2.08	2.07	2.05
T_g (K)	573	570	567	562

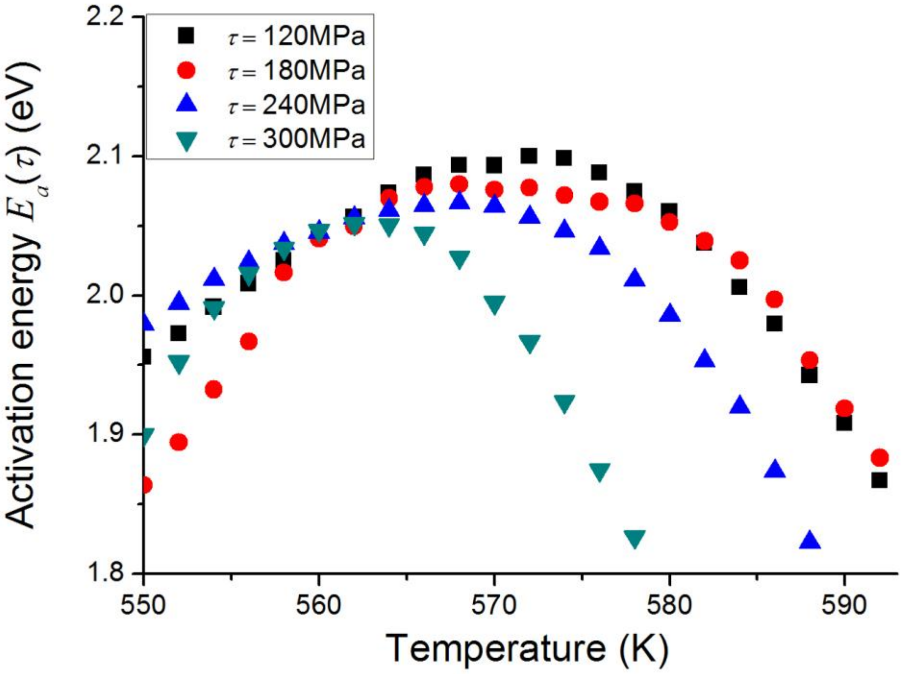

Figure 4.10 Activation energy of $Pd_{73}Si_{20}Cr_7$ samples after 8% homogeneous tensile deformation at T_a = 533 K under different pre-loading tensile stresses.

.

As discussed in Chapter 3, long time annealing at sub-T_g would change the metallic glasses from as-synthesized non-equilibrium state to a relatively ideal glassy state accompanying by annihilations of defects. On the contrary, it has been indicated by previous studies that through homogeneous deformation new defects would be created in the metallic glass matrix (Khonik and Spivak 1996), which can be considered as a structural transition from an ideal glass to the glass consisting of deformation defects.

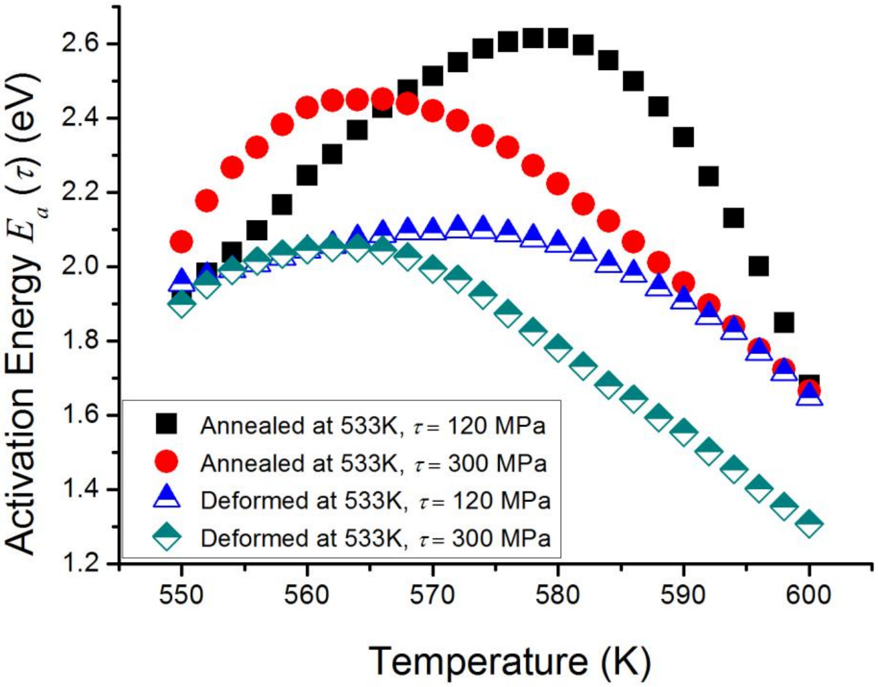

Figure 4.11 Activation energy of $Pd_{73}Si_{20}Cr_7$ samples under different pre-loading shear stresses. Samples have the same thermal history before internal friction test. The deformation strain is 8%.

Using the method mentioned in Section 3.2.2, the activation energy E_a of the deformed samples can be obtained, as shown in Figure 4.10. Similar to what we have discovered for 533 K annealed sample as shown in Figure 4.8, the maximum activation energy E_a which is referred as the activation enenrgy $E_0(\tau)$ for glass transition decreases with increasing pre-loading tensile stress τ, and the peak shifts towards lower temperature as shown in Figure 4.11, suggesting that T_g of sample decreases with increasing applied stress as listed in Table 4.1. Comparing $E_0(\tau)$ and T_g for reference sample as listed in Table 3.2 with those for sample after homogenous deformation as listed in Table 4.1, both $E_0(\tau)$ and T_g decrease after mechanical deformation, indicating that the energy barrier for glass transition reduces after homogenous plastic deformation. This is because homogenous plastic deformation would introduce addition defects in the glassy structure, promoting transformation from the glassy solid state to super-cooled liquid state. Figure 4.12 shows the relation between $E_0(\tau)$ and τ. By extrapolating the pre-loading tensile stress to zero, the activation energy E_g of glass transition without any loading can be calculated as 2.12 eV, and that for the reference specimen is 2.74 eV. Moreover, the average activation volume can be obtained as 0.043 nm^3, which is dramatically smaller than 0.145 nm^3 for reference sample which has been annealed at the same temperature without any plastic deformation. Smaller average activation volume could be caused by the additional deformation defects created through homogeneous plastic deformation at sub-T_g. The numbers of these additional deformation defects in the sample after mechanical deformation are much smaller than the original as-synthesized defects, which would drive the glassy solid to transform into a new disordered configuration. As shown in the energy configuration in Figure 4.13, sample after 8% homogeneous deformation can be considered to be at the higher energy state represented as a valley

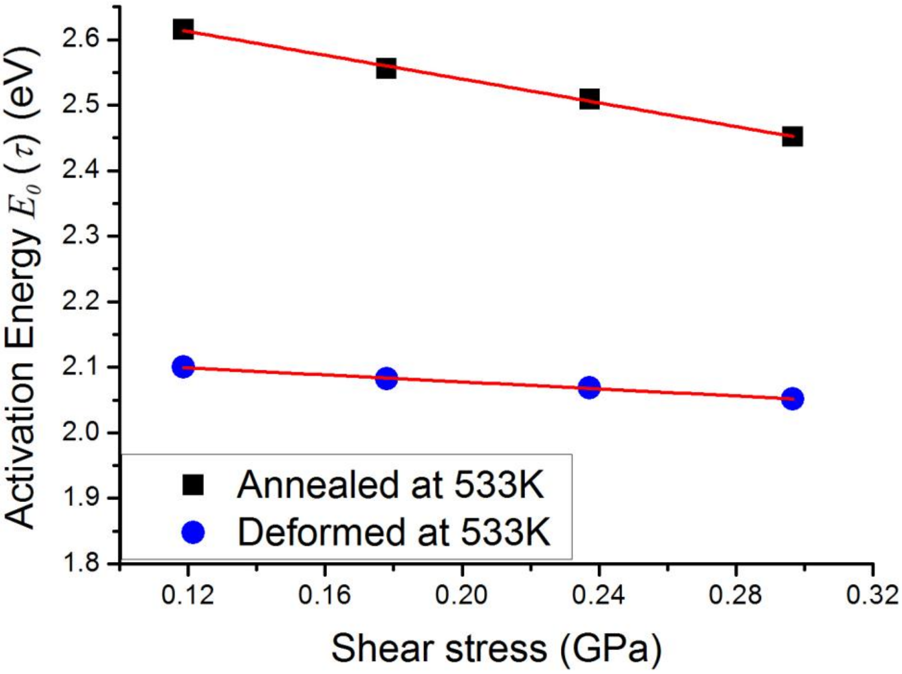

Figure 4.12 Relations between activation energy and pro-loading stress for sample after 8% tension at 533K and its reference sample.

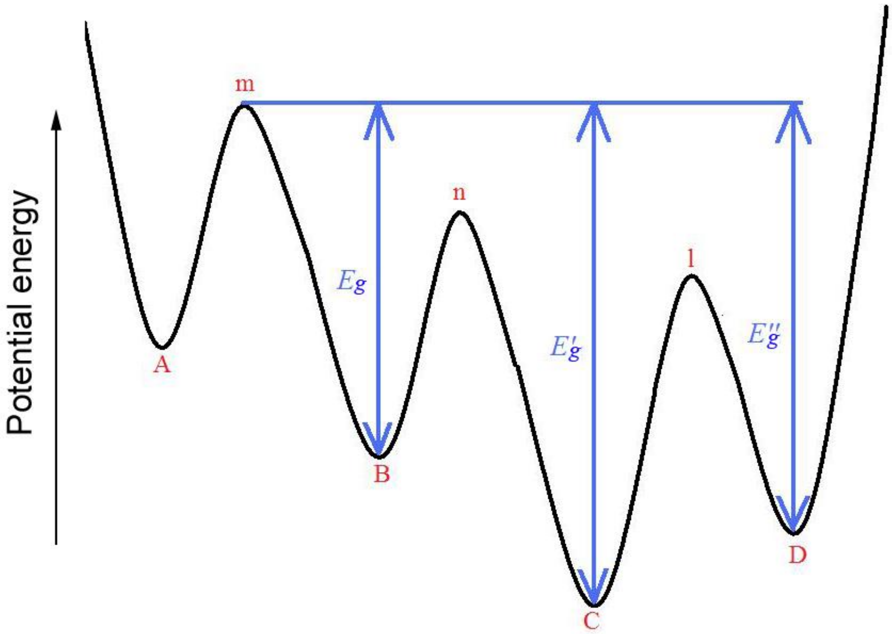

Figure 4.13 Schematic of energy state of metallic glass, where valley "A" represents the new energy state after glass transition activation; valley "B" represents the state of as-synthesized materials before activation; valley "C" represents the energy state after sub-T_g relaxation; and valley "D" represents the energy state after homogeneous plastic deformation at temperature below T_g. Saddle point "m" is an absolute energy point to be conquered for system under glass transition; "n" is an absolute energy point to be conquered for system under irreversible structural relaxation, and "l "is an absolute energy point to be conquered for plastic deformation below T_g.

"D", comparing with the valley "C" representing the potential of reference sample. Therefore, their potential difference can be calculated as $\Delta E = E_g'' - E_g' = 0.62$ eV.

4.3.2 Deformation defect creation as a process of phase transition

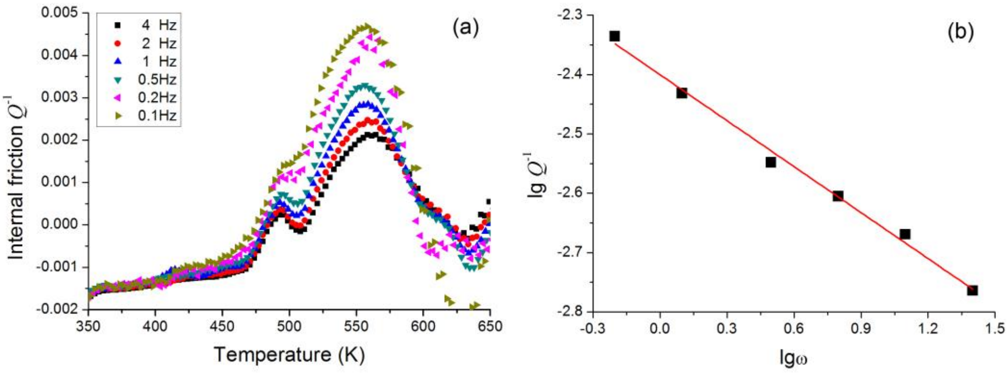

Figure 4.14 (a) Internal friction of $Pd_{73}Si_{20}Cr_7$ sample after 8% homogeneous deformation at 533 K, subtracted with that of its reference sample. The heating rate is $\dot{T} = 0.005$ K/s. (b) Relation between the height of internal friction peak in (a) and testing frequency

Unlike dislocations in crystalline solids which are characterized by the internal friction peaks at elevated temperature, there is no peak in internal friction associated with the deformation defects in metallic glass at temperatures higher than 100K. To investigate the IF characteristics of deformation defects in $Pd_{73}Si_{20}Cr_7$, we subtracted internal frictions of sample after 8% deformation with those of the reference sample as shown in Figure 4.14 (a). Such differences in internal frictions could be caused by the deformation defects generated through homogeneous plastic deformation.

With decreasing testing frequency, the peak becomes stronger, while the peak temperature does not change. The height of the internal friction peak has a logarithmic relation with the frequency as shown in Figure 4.14 (b), which is a characteristics of internal friction for first-order structural transition (Pérez-Sáez, Recarte et al. 1998; Perez-Saez, Recarte et al. 2000). This first-order structural transition peak could associate with the transformation of deformation defects created by homogeneous plastic deformation into an ideal glassy structure when temperature increases. The internal friction peaks for the deformation defects affected by testing frequency and heating rate are shown in Figure 4.15.

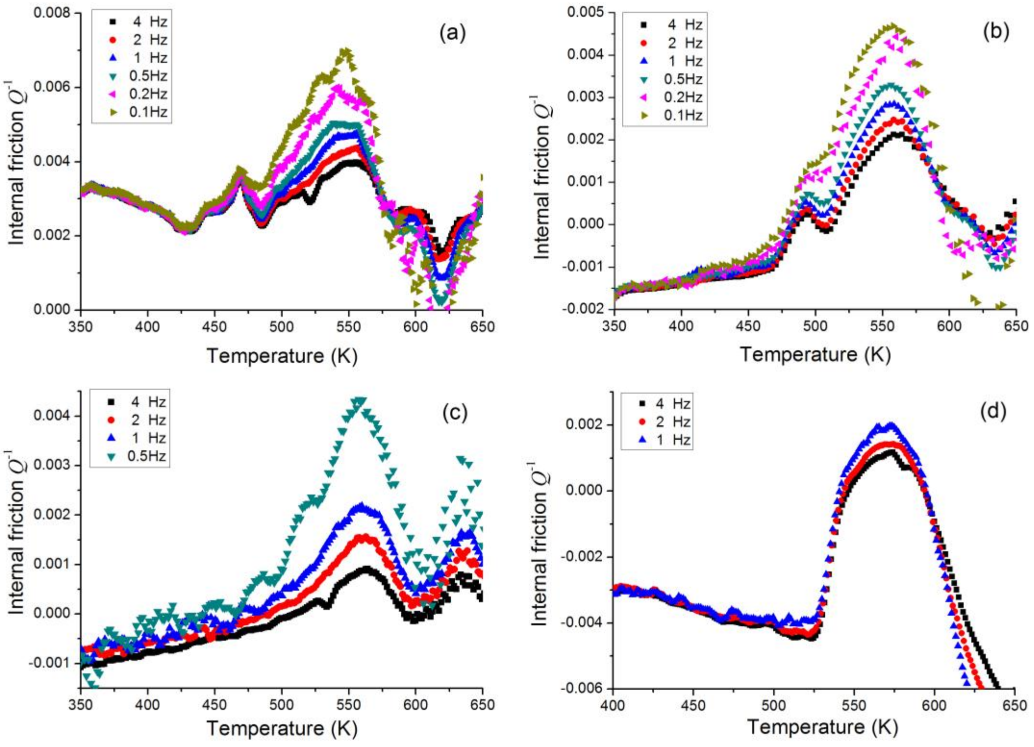

Figure 4.15 (a) Internal friction of deformation defect in $Pd_{73}Si_{20}Cr_7$ sample after 8% homogeneous deformation at 533 K. The heating rate is (a) 0.005 K/s, (b) 0.015 K/s, (c) 0.025 K/s and (b) 0.05 K/s.

For $Pd_{82}Si_{18}$ the first-order structural transition peak can be also observed in the internal friction of deformation defects obtained through subtracting the internal frictions of sample after 5% homogeneous plastic deformation with those of its reference one. As shown in Figure 4.16, the peaks increase with decreasing testing frequency. The peak temperature does not change with the testing frequency but increases with increasing heating rate. The relation between the peak height and the testing frequency is shown in Figure 4.17, which is well fitted as $Q^{-1} \sim \omega^{-\beta}$ with β = 0.24±0.02 un-affected by the heating rate. As discussed above, such peak of internal friction of deformation defect would associate with a first-order structural transition of the deformation defects into an ideal glass configuration at elevated temperature.

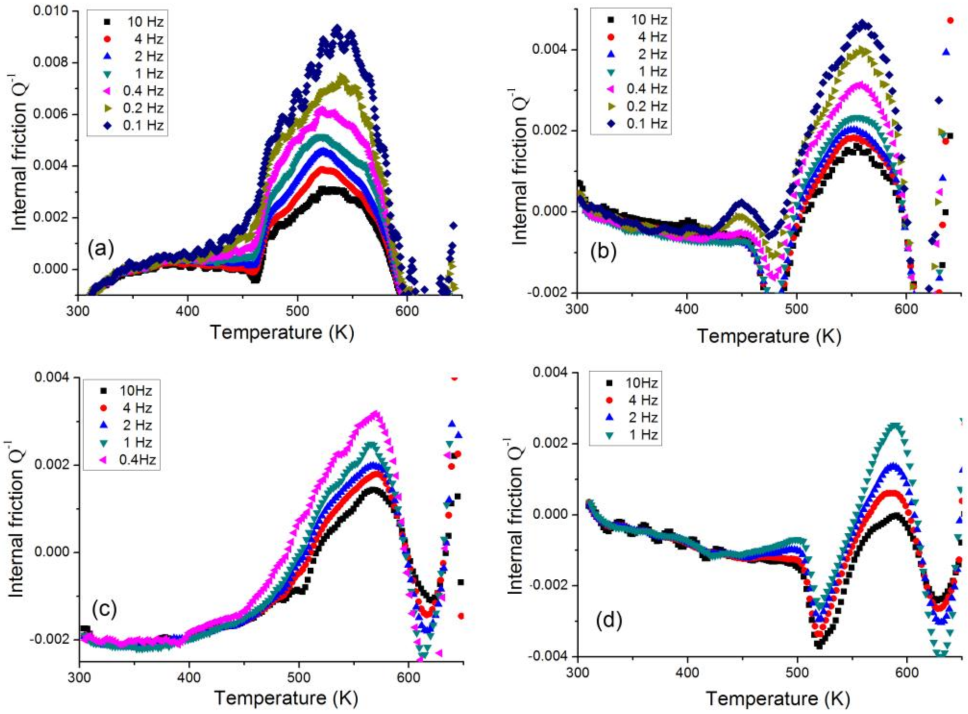

Figure 4.16 Internal friction of deformation defect in $Pd_{82}Si_{18}$ sample after 5% homogeneous deformation at 583 K. The testing heating rate is (a) 0.005 K/s, (b) 0.015 K/s, (c) 0.033 K/s and (b) 0.067 K/s.

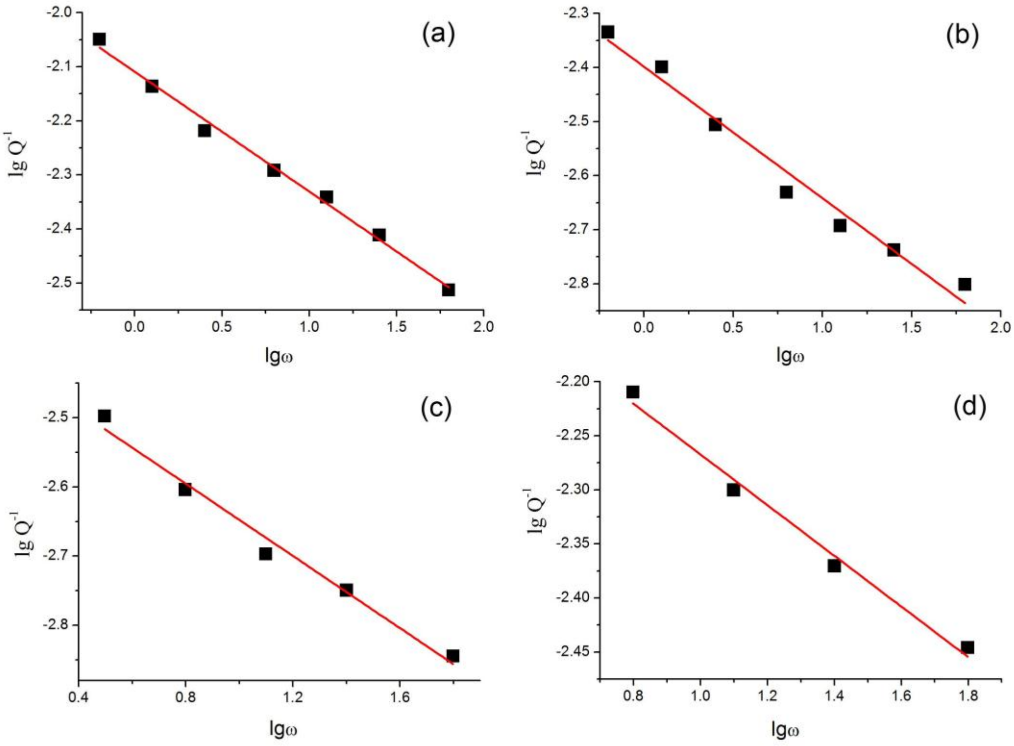

Figure 4.17 Relation between the internal friction height and frequency in Figure 4.16, with heating rates (a) 0.005 K/s, (b) 0.015

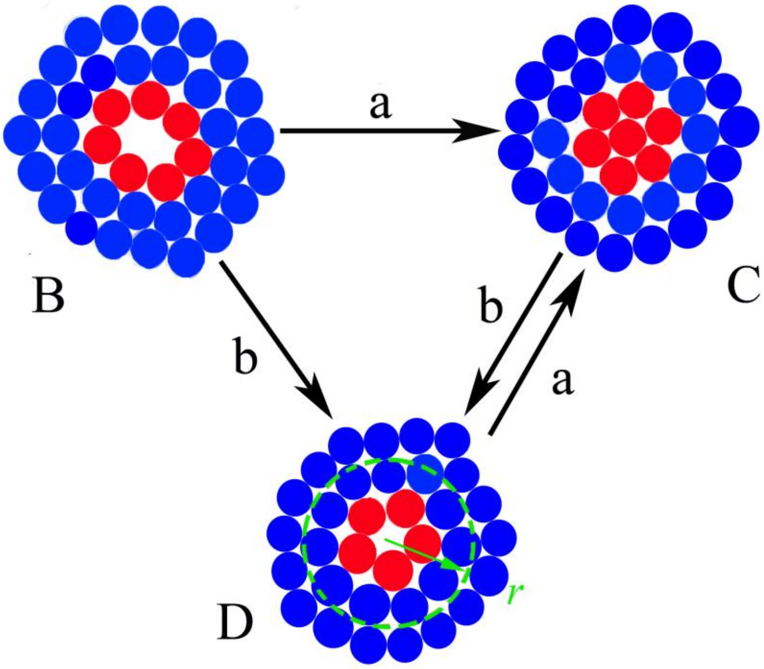

Figure 4.18 Models for the structural changes in metallic glass under thermal and mechanical stimulations. “B” marks the atomic configuration of the as-synthesized defects. “C” represents randomly close packed ideal glass. “D” marks the atomic configuration of deformation defect. Arrows “a” and “b” denote the thermal and mechanical stimulation processes, respectively. The schematic of these energy states is shown in Figure 4.13.

As-synthesized defects due to rapid quenching can be annihilated through annealing at sub-T_g as arrow “a” shown in Figure 4.18, or transform into defects with smaller sizes through local deformation as arrow “b” shown in Figure 4.18. Defects with metastable configuration of atoms marked as “D” in Figure 4.18 could be considered as deformation defects. Thus these deformation defects can be annihilated by thermal treatment or created by local shear deformation. If the metallic glass experiences homogeneous plastic deformation at sufficient low temperature, the net effect of atomic structural variations as shown in Figure 4.18 would be the creation of deformation defects. The model shown in Figure 4.18 that the transformation between the deformation defects (configuration “D”) and the ideal glass (configuration “C”) is rather through first-order structural transition than through relaxation, which has been already justified by our internal friction measurement results described above.

4.3.3 Activation energy for the creation of deformation defects

For the first-order phase transition, internal friction peak T_p would shift towards higher temperature with larger heating rate $\dot{T}$. Therefore, different heating rates as 0.005, 0.015, 0.025 and 0.05 K/s are applied in the dynamic mechanical analysis to systematically study the phase transformation from deformation defects to ideal glass structure in $Pd_{73}Si_{20}Cr_7$. The results are shown in Figure 4.19 (a). Table 4.2 lists the peak temperature T_p at different heating rates. The Kissinger relation (Kissinger 1957) for nucleation kinetics is used to describe the shifting of peak with heating rate:

$$\ln(T_\mathrm{p}^2/\dot{T}) = E_f/kT_\mathrm{p} + \mathrm{B}, \tag{4.1}$$

where k is the Boltzmann constant, E_f is the activation energy for the phase transition and B is a constant. Through Kissinger relation, the critical activation energy for phase transition can be obtained by plotting $\ln(T_p^2/\dot{T})$ versus $1/T_p$. A straight line with a slope of E_f/k can be figured out, as shown in Figure 4.19 (b). Therefore the activation energy for phase transition related with the deformation defects in $Pd_{73}Si_{20}Cr_7$ is calculated as $E_f = 2.48$ eV.

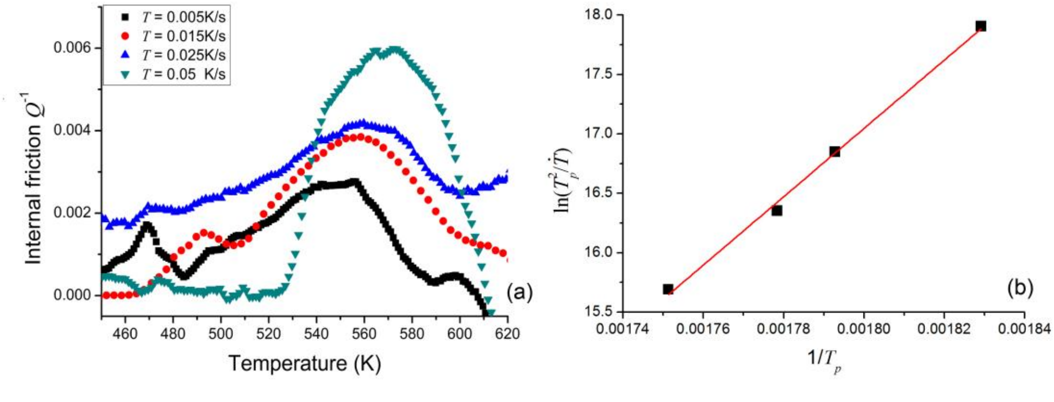

Figure 4.19 (a) Internal friction of deformation defect in $Pd_{73}Si_{20}Cr_7$ sample after 8% homogeneous deformation at 533 K. The testing frequency is 1Hz with four different heating rates (0.005, 0.015, 0.025 and 0.05 K/s); (b) Kissinger plot of $\ln(T_p^2/\dot{T})$ versus $1/T_p$ for the internal friction in (a).

Table 4.2 Peak temperature T_p of internal friction shown in Figure 4.19 for $Pd_{73}Si_{20}Cr_7$

Heating Rate (K/s)	**0.005**	**0.015**	**0.025**	**0.05**
T_a = 523K	547	558	562	571
T_a = 533K	550	559	565	573

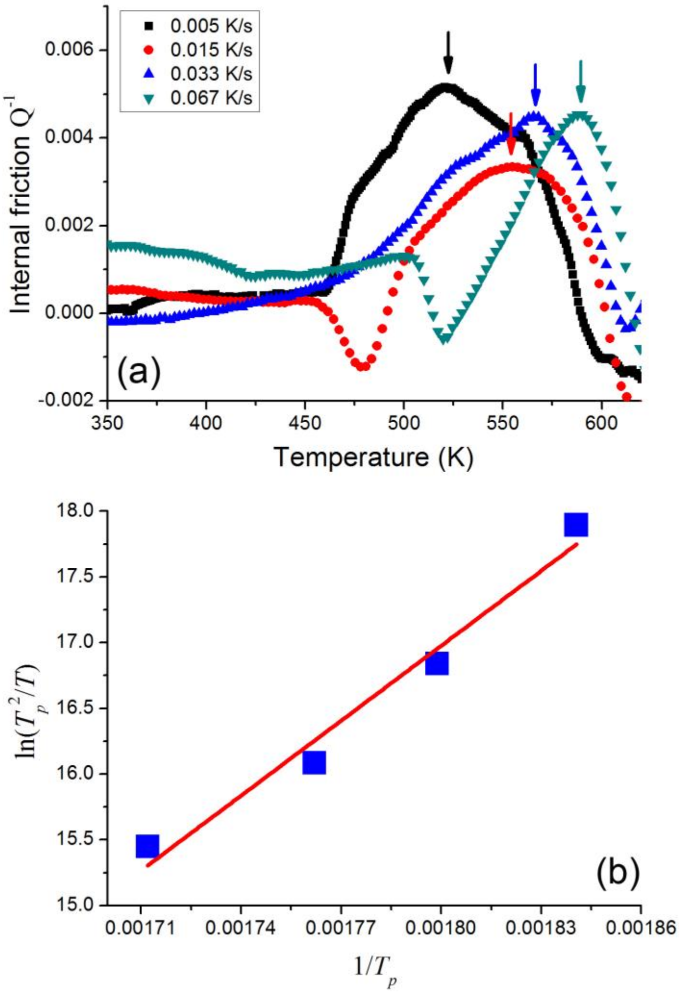

Figure 4.20 (a) Internal friction of deformation defects in metallic glass $Pd_{82}Si_{18}$ after homogeneous deformation at 583 K. The testing frequency is 1Hz with four different heating rates (0.005, 0.015, 0.033 and 0.067 K/s); (b) Kissinger plot of $\ln(T_p^2/\dot{T})$ versus $1/T_p$.

Table 4.3 Peak temperature T_p of internal friction shown in Figure 4.20 for $Pd_{82}Si_{18}$

Heating Rate (K/s)	**0.005**	**0.015**	**0.033**	**0.067**
$\dot{\varepsilon} = 10^{-4}\ s^{-1}$	534	556	567	588
$\dot{\varepsilon} = 2.5\times10^{-5}$	520	530	N.A.	559

Figure 4.20 (a) shows the increases of peak temperatures of internal frictions of deformation defects with increasing heating rates in $Pd_{82}Si_{18}$. Table 4.3 lists T_p at different heating rates in $Pd_{82}Si_{18}$ samples that have been homogeneously deformed at 583K with a strain rate $\dot{\varepsilon} = 10^{-4}\ s^{-1}$. Activation energy E_f of phase transition related with deformation defects in $Pd_{82}Si_{18}$ can be calculated as 1.64 eV.

4.3.4 Surface energy of deformation defects

Because of the structural and topological differences between deformation defects and nearby ideal glass in metallic glasses, there would be interface existing between the region consisting of defects and that of ideal glassy structure. The transformation between the deformation defects and ideal glass could be considered as the motion of such interface. Therefore, understanding the surface energy change is crucial for better understanding the phase transition of deformation defects in metallic glasses.

In the nucleation process of deformation defects, the total energy ΔG_{defect} of a deformation defect with a radius *r* is:

$$\Delta G_{defect} = -N \cdot \mu + 4\pi r^2 \gamma ,$$

$$\Delta G_{defect} = -\frac{4\pi}{3} \frac{r^3}{\Omega} \mu + 4\pi r^2 \gamma , \tag{4.2}$$

where *N* is the number of atoms inside the deformation defects; *r* is the defect radius as shown in Figure 4.18, Ω is the average atomic volume of atoms, *μ* is the potential energy for relaxation of atom and *γ* is the surface energy per unit area of interface formed between the defect and the surrounding ideal glass (Wright, Hufnagel et al. 2003). The critical radius r^* for nucleation of defect from the ideal glassy matrix can be described as:

$$r^* = \frac{2\gamma\Omega}{\mu} . \tag{4.3}$$

Therefore Eq. (4.2) can be rewritten to express the energy barrier ΔG_V:

$$\Delta G_V = \frac{16\pi}{3} \frac{\Omega^2 \gamma^3}{\mu^2} . \tag{4.4}$$

If we consider the nucleation of deformation defects from the ideal glass matrix as a process of plastic deformation, the energy change *μ* of atoms involve can be calculated as the difference of energy state: $\mu = E_g'' - E_g' = 0.62$ eV as described in Figure 4.13. And the energy barrier ΔG_V can be treated as the total energy for the structural transformation describing the process of the formation of deformation defect, which is already calculated using Kissinger relation as $E_f = 2.48$ eV for $Pd_{73}Si_{20}Cr_7$. Because the average volume Ω of atoms in the deformation defect is around 0.015 nm^3 as determined in Section 4.3.1, the surface energy associated with the deformation defect can be calculated from Eq. (4.4) to be 1.02 J/m^2.

4.4 Competition between creation and annihilation of deformation defects

As described in Section 4.3, deformation defect creation and annihilation occur simultaneously under homogeneous plastic deformation at elevated temperature. When the sample is homogeneously deformed at $0.7T_g<T<T_g$, the quantity of deformation defects annihilated increase with increasing temperature. The quantity of deformation defects created also increase with increasing plastic strains. By controlling temperature and strain rate during homogeneous deformation, the number of deformation defeats created can be controlled.

The internal frictions of deformation defects in $Pd_{73}Si_{20}Cr_7$ samples with different deformation strains 4% and 12% at 523K and at a strain rate of 10^{-4} min^{-1} are shown in Figure 4.21 (a) and (b), respectively. Both samples show internal friction peaks with first-order phase transition characteristics at 543K under a heating rate 0.005K/s. Moreover, the heights h_p of both internal friction peaks are the same: h_p = 0.005, which is obviously larger than h_p = 0.004 of that of the sample deformed at 533K with the same deformation strain rate 10^{-4} min^{-1} as shown in Figure 4.21 (c). The results demonstrate that metallic glasses deformed at lower temperature would create larger amount of defects. For $Pd_{73}Si_{20}Cr_7$ deformed at a higher temperature as 543K under the same strain rate 10^{-4} min^{-1}, internal friction peak for deformation defects would disappear as shown in Figure 4.21 (d). As strain rate is increased to 10^{-3} min^{-1} to homogeneously deformed $Pd_{73}Si_{20}Cr_7$ at T_a = 543K (its deformation curve is shown in Figure 4.4), the peak of internal friction of deformation defects in $Pd_{73}Si_{20}Cr_7$ would be detected as shown in Figure 4.22.

Homogeneous plastic deformation under different conditions such as isothermal temperature T_a and strain rate $\dot{\varepsilon}$ would lead to the formation of deformation defects with different densities. The results prove that there is competition between the thermal annihilation of deformation defects and the stress-induced creation of deformation defects when the sample is homogeneously deformed at $0.7T_g<T<T_g$. More deformation defects could be generated by homogeneous plastic deformation with higher strain rate at lower temperature. The changes in internal friction measured after the samples are deformed under different conditions further demonstrate that the IF peaks with first-order phase transition characteristics could be associated with the deformation defects.

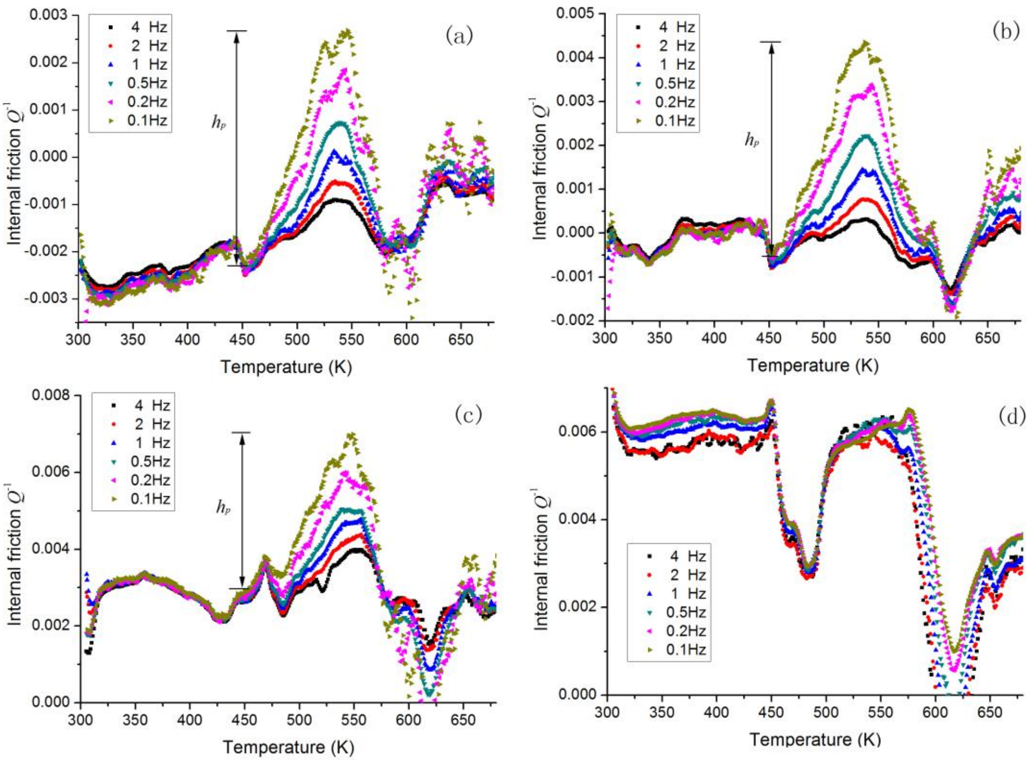

Figure 4.21 Internal friction of deformation defect in $Pd_{73}Si_{20}Cr_7$ for sample after (a) 4% and (b) 12% deformation at 523 K, (c) 8% deformation at 533 K, and (d) 8% deformation at 543 K, with the same strain rate 10^{-4} min^{-1}. The heating rate in the test is 0.005K/s.

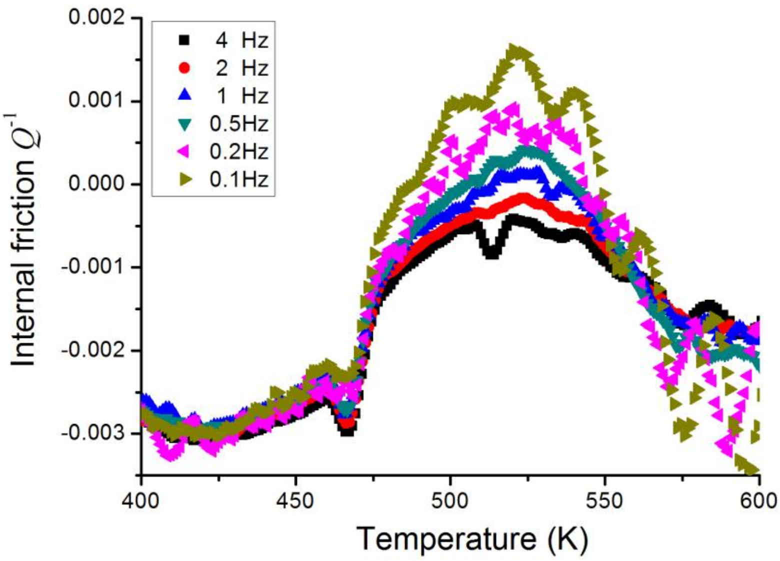

Figure 4.22 Internal friction of deformation defects in $Pd_{73}Si_{20}Cr_7$ sample after 8% deformation at 543 K with a strain rate 10^{-3} min^{-1}. The heating rate is 0.005K/s.

4.5 Relation between deformation defects and structural variation in metallic glasses

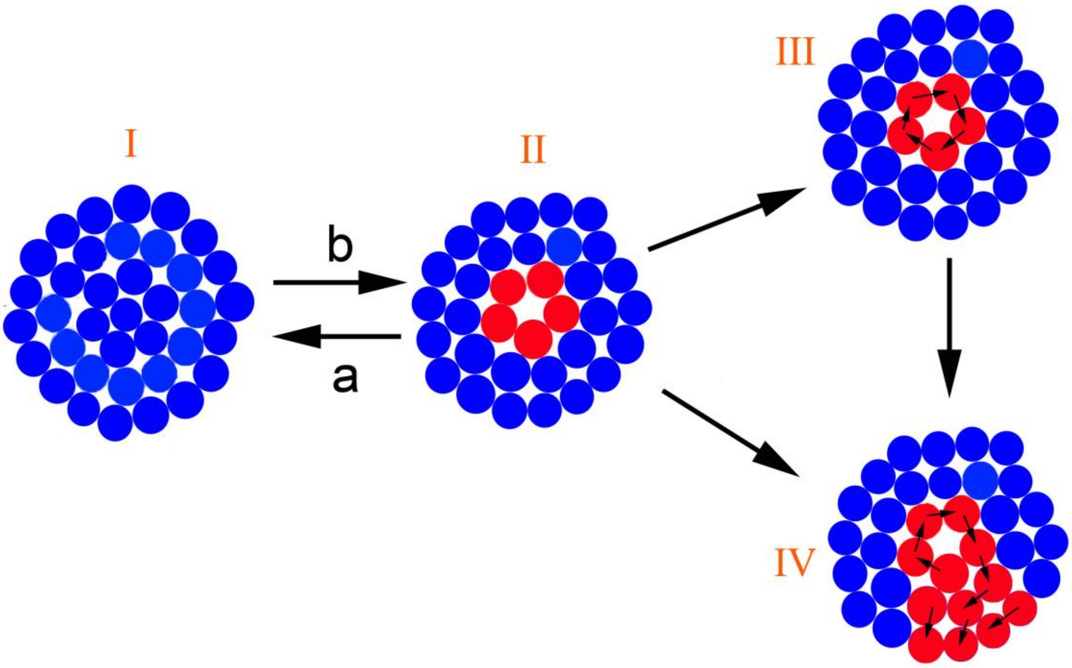

Figure 4.23 Schematics of atomic configurations in: (I) ideal glass and (II) defect, and atomic rearranging movement: (III) secondary relaxation and (IV) primary relaxation. Each energy state and atomic movement event can be activated through thermal or/and mechanical stimulation. Meanings of “a” and “b” are the same as those in Figure 4.18.

As discussed in Chapter 3, two main relaxation processes, *i.e.*, the primary relaxation and the secondary relaxation (which is also described as α relaxation and β relaxation respectively), govern the atomic relaxation in metallic glasses (Debenedetti and Stillinger 2001). The α relaxation dominates glass transition of metallic glasses, where the matrix confinement is collapsed and large scale rearrangements of atoms are activated, as shown in the schematic IV in Figure 4.23. On the other hand, β relaxation in metallic glasses is considered as localized translational motion of a cluster of atoms within the matrix confinement (Harmon, Demetriou et al. 2007).

Therefore β relaxation in metallic glasses is a reversible event, as shown in the schematic III in Figure 4.23.

Besides these two processes, there are small scale cooperative motions of local atoms that lead to irreversible structural changes in metallic glasses (Ladadwa and Teichler 2006). These irreversible events in metallic glasses might be closely related with weak local atomic the defects, where the probability of atomic rearrangement is larger than the around matrix confinement due to their so called “more disordered” topology. These irreversible events can be considered as the creation and annihilation of deformation defects as shown in Figure 4.23. We already defined in this chapter that creation and annihilation of deformation defects in metallic glasses exhibit phase transition characteristics. This transition process related with the rearrangement of local atoms would be different from the secondary relaxation process mentioned above. Secondary relaxation or β relaxation is a fully reversible process, since rearrangement of atoms is confined in the elastic matrix. This local rearrangement can be activated through thermal stimulation, when the constraint around is weaker due to the thermal activation. Restriction from the surrounding environment would push the shifted atoms back to their initial sites as the external influence is withdrawn. For the phase transition between ideal glass and the deformation defect as shown in Figure 4.23, atomic rearrangement can be excited mechanically or/and thermally. However rearranged atoms would retain their position variations and can not return to their initial sites, resulting in an irreversible structure change. In this chapter, this irreversible structural change is considered as a transition between two phase, ideal glass and defects, which is completely different from the secondary relaxation where atoms are slight rearranged or shifted inside the defective units without permanently altering their positions.

However, the creation and annihilation of deformation defects will affect the β relaxation as shown in Figure 4.23. It is speculated that the deformation defects could contribute to the secondary relaxation because of their weak structural configuration compared with the surrounding ideal glassy matrix. These additional loose-packed sites in metallic glasses provide sources for the translation motions of β relaxation. On the other hand, the concentration of deformation defect affects the glass transition as well. Because the energy potential is reduced through plastic deformation of metallic glasses, the glass transition with lower activation energy E_g is facilitated as shown in Figure 4.13.

4.6 Conclusion

Dedicated experiments are conducted to explore the internal friction (IF) related with deformation defects in metallic glass. The IF of deformation defects shows first-order phase transition characteristics. The activation energy and interfacial energy of deformation defects in Pd-Si metallic glasses are measured. The results demonstrate that the plastic deformation accommodated by the thermal or mechanical activation of deformation defects could be related with a structural transformation which is of first order. Such feature of plastic deformation in metallic glasses could facilitate the theoretical description and computational modeling on the atomistic details of localized plastic deformation in metallic glasses.

5. Phase field computer modeling

5.1 Introduction

5.1.1 Modeling shear banding in BMGs

The atomic structure of deformation defects such as average atomic volume, bonding orientation and number of coordinating atoms are different from that in the ideal glassy region (Argon 1979). Under critical loading conditions numerous deformation defects are connected with each others to form shear bands in which the plastic strains are localized (Spaepen 1977). Since shear banding is the only deformation mechanism operating at temperatures below $0.7T_g$, the defects that are responsible for the shear banding must be atomistic and collective (Zheng 2011). Regions with lower density and higher degrees of chemical or structural disorders in metallic glasses are preferred to conduct shear flow via shear banding (Zhu, Shiflet et al. 2010). Both the microscopic and macroscopic deformation behaviors are actively investigated in the past decades. Although connection between macroscopic mechanical properties and local dislocation activities is well established for the crystalline materials, the connection between the microscopic and macroscopic deformation behaviors in metallic glasses is still missing. Therefore, for better understanding the deformation behaviors of metallic glasses that are promising in industrial application, it is necessary to predict the material failure or guide the design and application of metallic glasses using computer modeling.

Due to the length scale limitation of first-principles and molecular dynamic simulations, the macroscopic deformation behaviors of metallic glasses are not well understood. On the other hand, the finite element method (FEM) is incapable of characterizing the nano-scale shear bands, which play a dominant role in the deformation behavior of metallic glasses. In this chapter, we applied phase-field modeling to illustrate the mesoscopic deformation behavior during shear-banding introduced plastic deformation based on the collective activities of deformation defects. Advantages of applying phase-field simulation on plastic deformation of metallic glasses can be interpreted as follows (Zheng 2011):

1. Phase-field modeling formulism is established based on the experimental study of deformation defects in the metallic glasses. Parameters about the ideal glassy matrix and deformation defects can be obtained from experiment for the construction of those energetic functions necessary for the modeling. As a phenomenological model formulized by free energy function of the amorphous system, this method bridges the atomistic structural changes with the macroscopic mechanical properties of metallic glasses.

2. Without the length scale limitation which has prevent the first-principles and molecular dynamic methods from characterization of shear banding, phase-field modeling could capture the deformation details such as shear band formation, propagation and branching in the length scales from tens of nanometers to tens of

microns.

3. Unlike the FEM, which ignores the details of nano-scale shear bands, mesoscopic phase-field method could characterize the localized structure changes when shear bands form and propagate.

5.1.2 Phase field modeling of metallic glass

5.1.2.1 Transition theory for the deformation and fracture of metallic glasses

It is has been proved by experiments that brittleness due to annealing corresponds well to the decrease of free volumes, since there are less defects in the glass to carry the plastic deformation (Yoo, Park et al. 2009). As discussed in Section 4.2, plastic deformation of metallic glasses is always accompanied by local defect creation since dilatation stress introduces extra volumes for atomic diffusion and rearrangement. Therefore free volumes inside deformation defects can be considered as microscopic flow units in glassy material. Free volume v_f of an atom is defined by $v_f = v_i - v_0$, where v_i is the volume of Voronoi polyhedron of the atom and v_0 is atomic volume. The normalized deformation defect density can be represented as $v_f/(v_m - v_0)$, where v_m is the maximum free volume when complete decohesion occurs in the glassy alloy. Therefore, we could define the density of deformation defects $w(r)$ at position r as a coarse-grain average of deformation defect density in a spatial region of R_0 which is the average size of deformation defect.

Deformation defect can be thermally or mechanically activated because it is more vulnerable to internal rearrangement than its dense random packing counterpart in the matrix (Argon 1979). At temperature well below T_g and under the applied stress $\sigma_A << \sigma_F$, which is a critical stress for local plastic flow, the amorphous solid acts like an elastic medium since there is little deformation defect sites that can be activated. As σ_A approaches σ_F, defect sites can be activated by applied stress (Spaepen 1977) or by local heating (Chen, He et al. 1994) due to plastic deformation. When the accumulation of these activated deformation defect reaches a critical value, the shear band forms (Gerlin, Schimansky et al. 1988). Further growth of defect sites leads to the local fracture events. Zheng *et al.* (Zheng and Li 2009) expressed the free energy density of deformation defects by a Ginzburg-Landau formulism as

$$f = \frac{a}{2} w^2 + \frac{b}{3} w^3 + \frac{c}{4} w^4 + \ldots \quad , \tag{5.1}$$

where a, b and c are coefficients depending on local strain energy and temperature. The local strain energy can be written as

$$\begin{aligned} e[\varepsilon_{ij}] &= \frac{1}{2} C_{ijkl} \varepsilon_{kl} \varepsilon_{ij} \\ C_{ijkl} &= \mu(\delta_{ik}\delta_{jl} + \delta_{il}\delta_{jk}) + \lambda \delta_{ik}\delta_{jl} \ , \end{aligned} \tag{5.2}$$

which is the strain tensor defined by the displacement field **u** through the relation $\varepsilon_{ij} = (\partial u_j / \partial x_i + \partial u_i / \partial x_j)/2$ and *i*, *j* = 1, 2, 3; μ is the shear modulus and λ is related to the bulk modulus *B* by $B = \lambda + 2\mu/3$. Because the deformation defect density is very small at the elastic region, Zheng *et al.* (Zheng and Shen 2010) expanded the coefficients of Eq. (5.1) can be expanded by the plastic strain energy $\Delta e = e[\varepsilon_{ij}] - e_0$:

$$\begin{aligned} a &= a_0 + a_1 \Delta e + a_2 (\Delta e)^2 + \ldots \\ b &= b_0 + b_1 \Delta e + b_2 (\Delta e)^2 + \ldots \\ a &= c_0 + c_1 \Delta e + c_2 (\Delta e)^2 + \ldots \end{aligned} , \qquad (5.3)$$

where e_0 is the strain energy of glassy alloy at the elastic limit. a_0, b_0 and c_0 are independent of strain. Assuming the leading error term $\Delta e \cdot w^4$ or $(\Delta e)^2 \cdot w^2$, the free-energy density of deformation defects described by Eq. (5.1) is thus approximated as (Zheng and Shen 2010)

$$f = \frac{a_0}{2} w^2 + \frac{b_0}{3} w^3 + \frac{c_0}{4} w^4 + \left(\frac{a_1}{2} w^2 + \frac{b_1}{3} w^3\right)(e[\varepsilon_{ij}] - e_0) . \qquad (5.4)$$

The coefficients of Eq. (5.4) depend on the energy landscape of defects. There should exist an energy barrier between the un-activated ($w = 0$) and activated ($w \sim 1$) states of deformation defects in BMG, which can be interpreted as E_f calculated in Section 4.3, since it is considered as an activation energy for the deformation defects. When *w* increases to a critical value w_c under plastic deformation as described on Figure 5.1, shear bands may form.

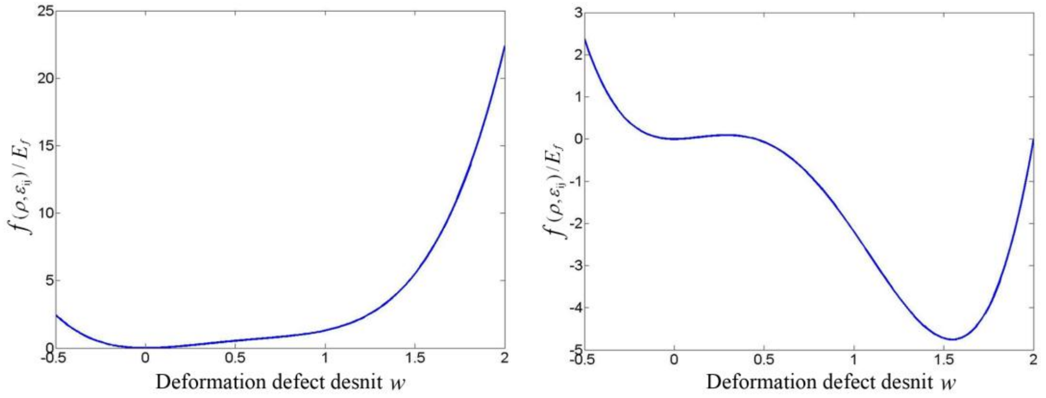

Figure 5.1 Free energy density of deformation defect (a) without local shear energy, (b) with local elastic energy due to the applied stress, deformation defects can be activated from $w = 0$ in (a) to $w = 1.5$ in (b)

5.1.2.2 Phase-field modeling of shear band propagation in metallic glass

Based on the atomic-scale deformation mechanism of metallic glasses, the free-energy functional of metallic glasses under external loading is given by Zheng *et al.* (Zheng and Shen 2010) as:

$$F = \int \{\frac{\kappa}{2}|\nabla w|^2 + f(w,\varepsilon_{ij}) + \frac{\rho}{2}[\dot{\vec{u}}]^2\} dV\,, \tag{5.5}$$

where κ is the surface tension of deformation defect where free-volume tends to locate. ρ is the density of solid. Based on the Ginzburg-Landau formulism, the equations of motions for *u* and *w* are described respectively by

$$\tau_w \frac{\partial w}{\partial t} = -\frac{\delta F}{\delta w} = \kappa\nabla^2 w - (a_0 w + b_0 w^2 + c_0 w^3) - w(a_1 + b_1 w)(e[\varepsilon_{ij}] - e_0) \tag{5.6a}$$

and

$$\rho \frac{\partial^2 \vec{u}}{\partial t^2} = -\nabla \cdot [\frac{\delta F}{\delta \varepsilon_{ij}}] = \mu \nabla \cdot [w^2 (\frac{a_1}{2} + \frac{b_1}{3} w) \nabla \vec{u}] \quad . \qquad (5.6b)$$

where τ_w is the characteristic time of deformation defect activation. Eqs.(5.2) and (5.6) govern the local strains and the evolution of deformation defects generated by the plastic deformation in metallic glasses, respectively, and thus form a complete set of equations for the description of dynamics of deformation and fracture of metallic glasses. By solving these equations, the shear banding resulting from the evolution of defects can be obtained. Further growth of shear bands leads to cracking of metallic glasses.

Noted that Eq. (5.6a) is similar with the Langevin equation describing the diffusion of stochastic particles, the phase-field model for the description of deformation defects developed above in general differs from the previous work (Spaepen 1977; Thamburaja and Ekambaram 2007) where the evolution of free volumes is treated by diffusion-creation-annihilation equation, or transition state model. It remains very interesting to compare these two approaches. For example, under what circumstances their predictions of shear banding converge. Nonetheless we can observe that the gradient term of defects in the free energy functional (Thamburaja and Ekambaram 2007) plays an important role in the description of shear banding.

5.2 Model building

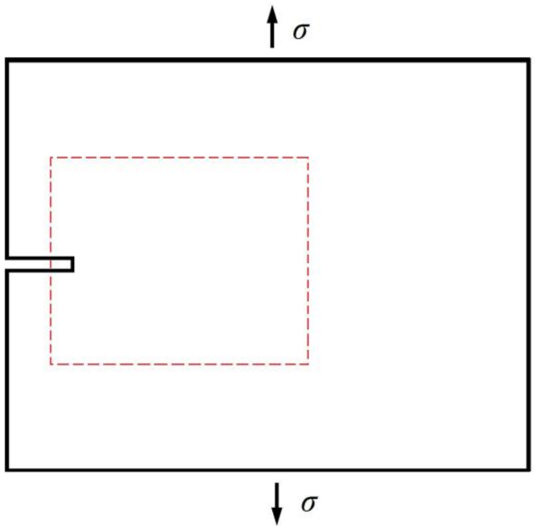

Figure 5.2 System for the simulation of shear banding in metallic glass.

As shown in Figure 5.2, we consider a $Pd_{73}Si_{20}Cr_7$ ribbon plate with a single-edge notch which is simplified as a plane-stress problem. The size of this plate is 20 μm×20 μm with a thickness d = 2 μm. An initial crack with a length of l_0 = 0.4 μm is introduced prior to the application of a tensile stress along the y direction and at the upper and lower boundaries. For the simulation of shear banding and crack propagation in metallic glass of $Pd_{73}Si_{20}Cr_7$ with materials properties listed as follows: T_g = 570 K; the Young's modulus E = 90 GPa; Poisson's ratio ν = 0.41; ρ = 10000 kg/m^3 (Wang 2005). The elastic strain limit under uniaxial tension is ε_0 = 2%.

As first proposed by Argon (Argon 1979) and Spaepen (Spaepen 1977), the deformation defect activation energy is an important parameter which characterizes the microscopic deformation behaviors of metallic glasses, which from experimental results is generally determined by the strain-rate-sensitivity of plastic flow at various temperatures below T_g (Wang, Pelletier et al. 2005). For $Pd_{73}Si_{20}Cr_7$, E_f has already been calculated as 2.48 eV. In our phase-field formulism, E_f is equivalent to the energy barrier indicated by Eq. (5.4) for un-deformed BMG. Thus the coefficients of Eq. (5.6) are given by $a_0 = 4(2\text{-}T/T_g)E_f$, $b_0 = -32E_f$, $c_0 = 16E_f$. To stabilize the activated deformation defectstate at w=1 under plastic deformation we choose $a_1 = 4$ and $b_1 = -9$. We define that the shear band forms in a region where $w > w_c = 0.8$ and the cracking or fracture occurs in BMG if $w > 1$.

Another important parameter which determines the microscopic deformation behaviors is the surface tension κ of deformation defect. Because the growth and evolution of deformation defect lead to fracture surface, κ can be estimated from the surface energy $\kappa = \gamma R$, where R is the characteristic length of the vein pattern at the fracture surface. In the simulation, we use $R = 0.5$ μm. It should be noted that γ is not the solid (glass) - vapor surface energy because of the unique structure of deformation defect. The parameter γ has already been calculated in the last Chapter 4 as around 1 J/m^2 for both as-synthesized and relaxed $Pd_{73}Si_{20}Cr_7$ samples.

Based on the triangle meshes of the model system, partial differential equations (Eqs. (5.6a) and (5.6b)) are solved numerically using Crank-Nicolson scheme. The length rescale factor

$$l_r = \sqrt{\kappa / \mu e_0}\,, \tag{5.7}$$

and time rescale factor

$$t_r = l_r / \sqrt{\mu / \rho} \tag{5.8}$$

are used to reduce Eqs. (5.7) - (5.8) into dimensionless equations. Hence l_r and t_r represent the length scale and the time scale of the system respectively. The meshes are adaptive when shear band present in the metallic glass matrix. The sizes of triangle meshes can be as small as 0.2 nm. These features are essential in the numerical simulation since Eqs. (5.7) and (5.8) are extremely stiff because of the shear localization. We find that although the system size is small compared with the actual metallic glass, the simulation results are not dependent on the system sizes. This is because the shear bands generated by the activated deformation defects are typically localized within a length scale of tens of nanometers, as shown in Figure 5.3.

5.3 Simulation results

We consider the shear band propagation in the as-synthesized metallic glass $Pd_{73}Si_{20}Cr_7$ with an activation energy of E_f = 2.48 eV. The shear band of the metallic glass starts from the original crack when the stress intensity factor K_I is larger than 19.8 MPa m$^{1/2}$ and will spread away, which has been successfully captured by our phase-filed modeling as shown in Figure 5.3. For 19.8 MPa m$^{1/2}$< K_I <26.6 MPa m$^{1/2}$, we can see that the plastic strain accumulated resulting from activated deformation defect (w>0.8) is highly localized in a single shear band with 50nm thickness as shown in Figure 5.3 (a1)-(a5). If K_I > 26.6 MPa m$^{1/2}$, branching of shear band or crack (w>1.0) occurs resulting from shear band propagation as shown in Figure 5.3 (b1)-(b5) and (c1)-(c5). Under large applied load, multi-branching of shear band occurs in a way similar to that observed in experiments (Lowhaphandu and Lewandowski 1998). These features have not been captured by other simulation methods such as MD and FEM before, suggesting the successful application of the phase-field approach on the modeling of deformation in metallic glasses.

The velocity of shear band propagation in this phase field model is shown in Figure 5.4. For shear band propagation under stress intensity factors 44.4 MPa m$^{1/2}$ and 66.7 MPa m$^{1/2}$, branching of shear band would occur as more plastic deformations would be carried by more shear bands. The velocity of shear band propagation would decease before branching, which reduce the risk of catastrophe failure of metallic glass since the spreading of shear banding is hindered. Therefore, the formation of multiple shear bands in the metallic glass would be crucial for the plasticity of metallic glass.

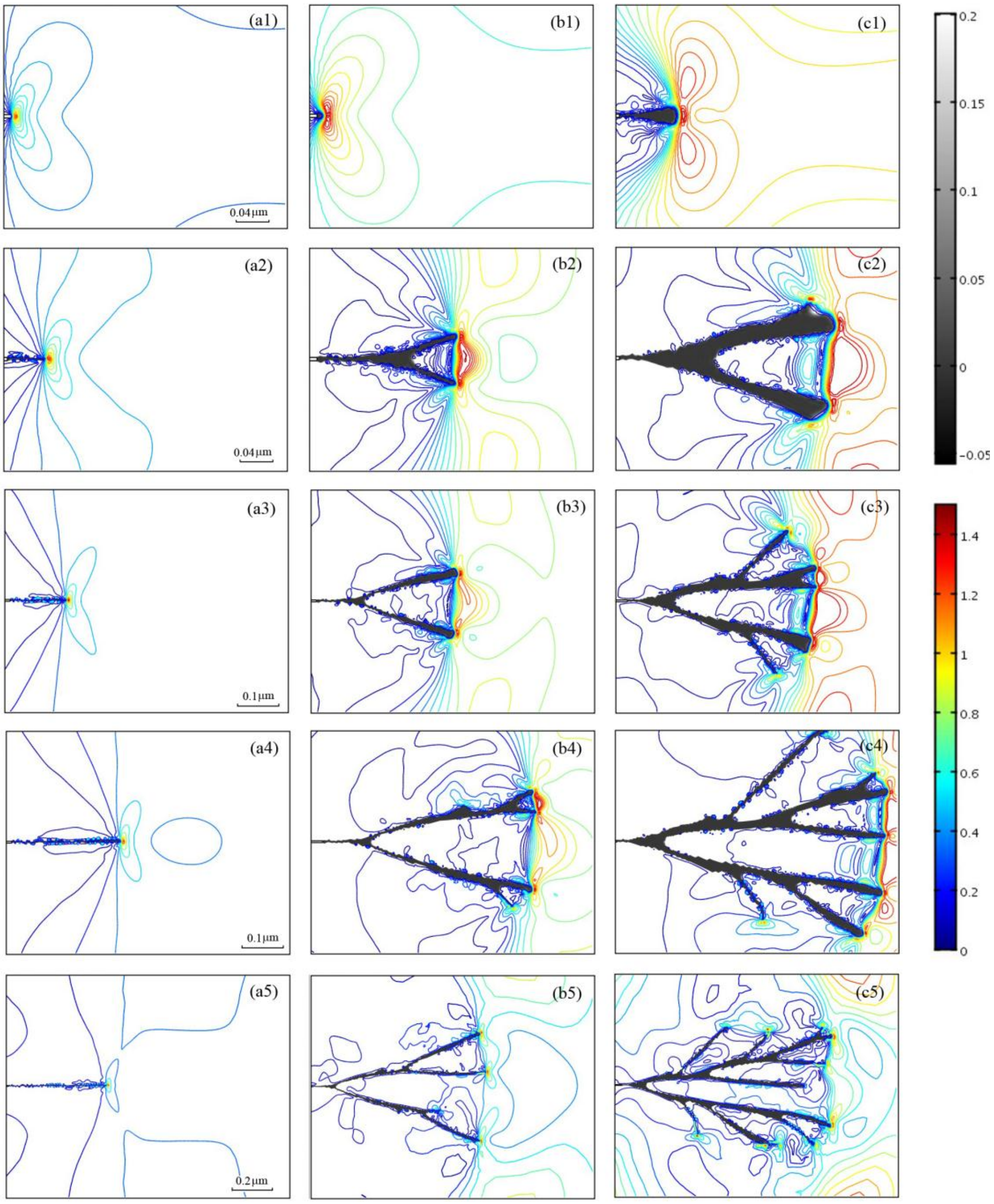

Figure 5.3 Shear banding and crack propagation in annealed metallic glass Pd$_{73}$Si$_{20}$Cr$_{7}$ under stress intensity factors K = 22.2 MPa m$^{1/2}$, 44.4 MPa m$^{1/2}$and 66.7 MPa m$^{1/2}$ for columns (a) ~ (c), respectively, and at time t = 30, 40, 50, 60, 80 ns for rows (1) ~ (5) respectively. The gray scales correspond to the values of 1 – *w*, The color bars (×870 MPa) are for the contour plots of Von Mise stress in the plate.

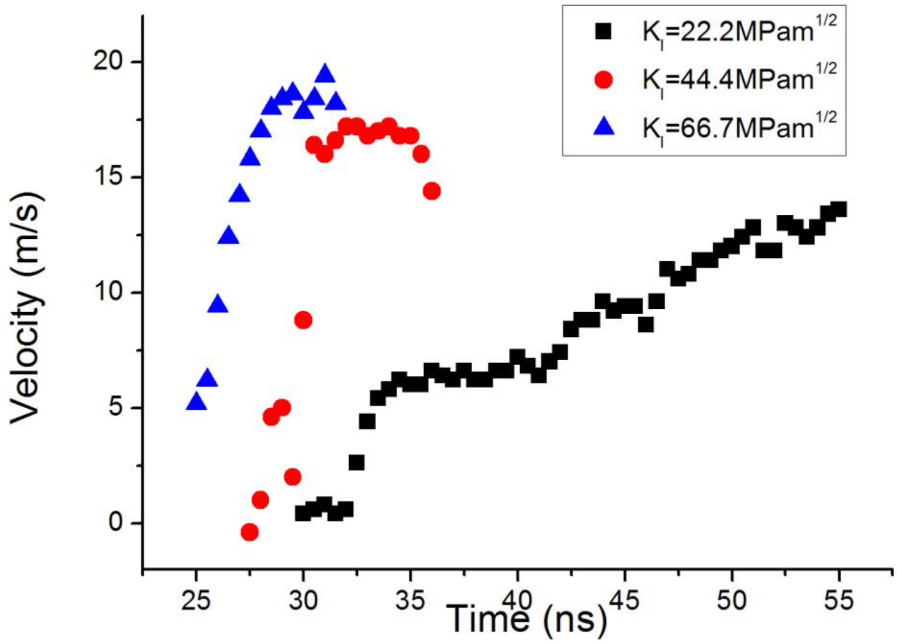

Figure 5.4 Velocity of shear band propagation under stress intensity factors K = 22.2 MPa m$^{1/2}$, 44.4 MPa m$^{1/2}$ and 66.7 MPa m$^{1/2}$ in (a) as-synthesized and (b) annealed metallic glass $Pd_{73}Si_{20}Cr_7$ before branching.

Based on experimental study of the local deformation defects of the metallic glasses, the mesoscopic phase field modeling provides a useful tool to characterize the macroscopic mechanical properties of the metallic glasses using a phenomenological model for the atomistic deformation defects. The deformation behaviors from these simulation studies would facilitate our further attempt to improve its mechanical properties, especially its plasticity.

5.4 Phase-field modeling of shear band propagation in fiber-reinforced BMG composites

Assume the crystalline reinforcements are in fiber shape and are embedded in the

BMG matrix. If the adhesion between the fiber and the BMG matrix is perfect, the strain in the composite should be continuous at the fiber-BMG interface. Under this condition, the shear band initiating in the BMG matrix either detours or passes through the crystalline fiber. In the later case, we also need to consider the phase-field modeling for fracture of the crystalline fiber. Although the fracture and cracking processes in crystalline solid are complicated because of the dislocations generated, the dynamics process of fracture in crystalline solid has already been analyzed successfully using phase-field approaches.

Considering the phase field ϕ describing the state of fracture of the crystalline solid: $\phi = 1$ denotes fully ruptured state and $\phi = 0$ denotes unbroken solid. As shown in Eq. (5.9) the govern equation for the phase field ϕ is developed by Karma *et al.* (Karma, Kessler et al. 2001; Karma and Lobkovsky 2004) to investigate the unsteady crack motion during brittle facture:

$$\tau \frac{\partial \phi}{\partial t} = D_\phi \nabla^2 \phi - V'(\phi) - \frac{\mu}{2} g'(\phi)(\left|\varepsilon_{ij}\right|^2 - \varepsilon_c^2) , \qquad (5.9)$$

where τ determines the characteristic time of fracture process and D_ϕ characterize the size of fracture process zone. $V(\phi) = \phi^2(1-\phi^2)/4$ is a double-well potential describing the states of fracture mentioned above. $g(\phi) = 4\phi^3-3\phi^4$ is used to stabilize the unbroken state when the strain ε_{ij} is smaller than a critical value ε_c. Hence ε_c is a measure of the fracture energy of the crystalline fiber.

Although the underlying physics of phase-field modeling of fracture in crystalline solid is not straight forward because there exists long-range elastic interaction resulting from the dislocation activities, Eq. (5.9) may provide a way to investigate the crack propagation in crystalline solid in the mesoscopic scales. Combined with the equations of motions for defects and displacement field as described in Section 5.1, Eq. (5.9) can be used to understand how fiber reinforcements affect the shear banding and crack propagation in the BMG matrix.

5.4.1 Modeling

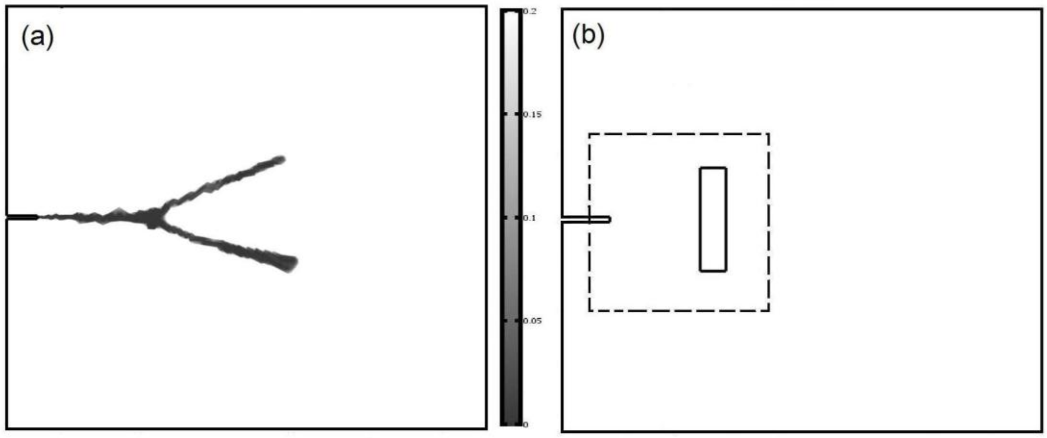

Figure 5.5 (a) Shear band in BMG without any reinforcement; (b) model system of fiber-reinforced BMG composite plate.

As shown in Figure 5.5, we consider a BMG plate with a single-edge notch which is simplified as a plane-stress problem. The size of this plate is 20 μm × 20 μm with a thickness d = 2 μm. The reinforcements are in rectangle shape. An initial crack with a length of l_0 = 0.4 μm is introduced prior to the application of a tensile stress along the y direction and at the upper and lower boundaries. For the simulation of shear banding and crack propagation in BMG, we choose a Zr-based BMG (Zr-Ti-Ni-Cu-Be) with the materials properties listed as follows: T_g = 625 K; the Young's modulus E = 90 GPa; Poisson's ratio $\nu = 0.36$, ρ = 6050 Kg/m^3. The elastic strain limit under uniaxial tension is $\varepsilon_0 = 1.2\%$.

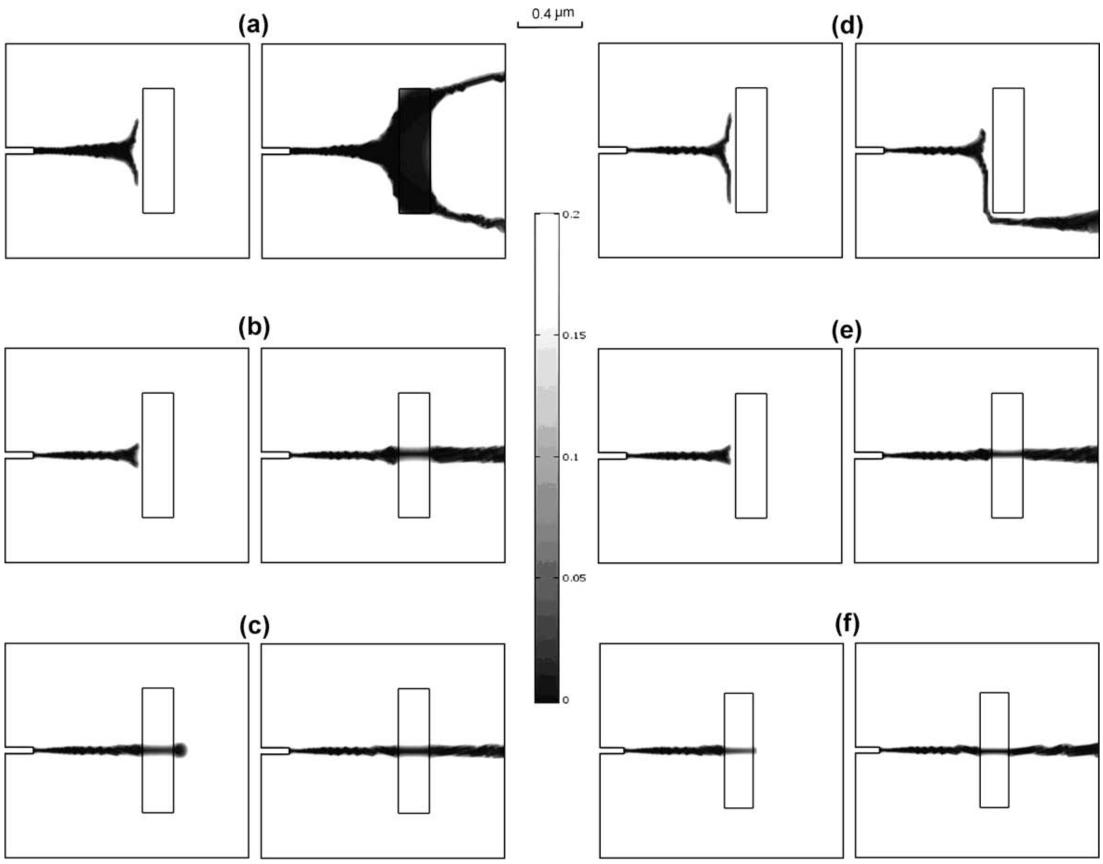

Figure 5.6 The crack propagations in different fiber-reinforced BMGs under K = 36.5 MPam$^{1/2}$. The gray scales correspond to the values of 1-w in the BMG matrix or the values of 1-ϕ in the fiber. For parameters of the fiber: (a) e_c = 354 J/m^2; γ_t = 10.2 J/m^2, t = 42 ns and 45 ns; (b) e_c = 354 J/m^2; γ_t = 5.1 J/m^2, t = 35 ns and 40 ns; (c) e_c = 354 J/m^2; γ_t = 2.04 J/m^2, t = 35 ns and 40 ns; (d) e_c = 708 J/m^2; γ_t = 4.08 J/m^2, t = 45 ns and 50 ns; (e) e_c = 708 J/m^2; γ_t = 3.06 J/m^2, t = 35 ns and 40 ns; (f) e_c = 708 J/m^2; γ_t = 2.04 J/m^2, t = 35 ns and 40 ns.

For Zr-based BMG, activation energy ΔG is 4.6 eV at room temperature (Lu, Ravichandran et al. 2003). Thus the coefficients of Eq. (5.4) are given by $a_0 = 4(2-T/T_g)\Delta G$, $b_0 = -32\Delta G$, $c_0 = 16\Delta G$. To stabilize the activated deformation defect state at $w = 1$ under plastic deformation we choose $a_1 = 4$ and $b_1 = -9$. We define that the shear band forms in a region where $w > w_c = 0.8$ and the cracking or fracture occurs in BMG if $w > 1$. The surface energy can be approximated by the liquid surface energy which is of the order of 1 J/m^2 for Zr-based BMG. Evidence for this comes from the observations of vein-patterned fracture surface and molten droplets on the fracture surface. In the simulation we choose $\gamma = 2$ J/m^2 as an approximation.

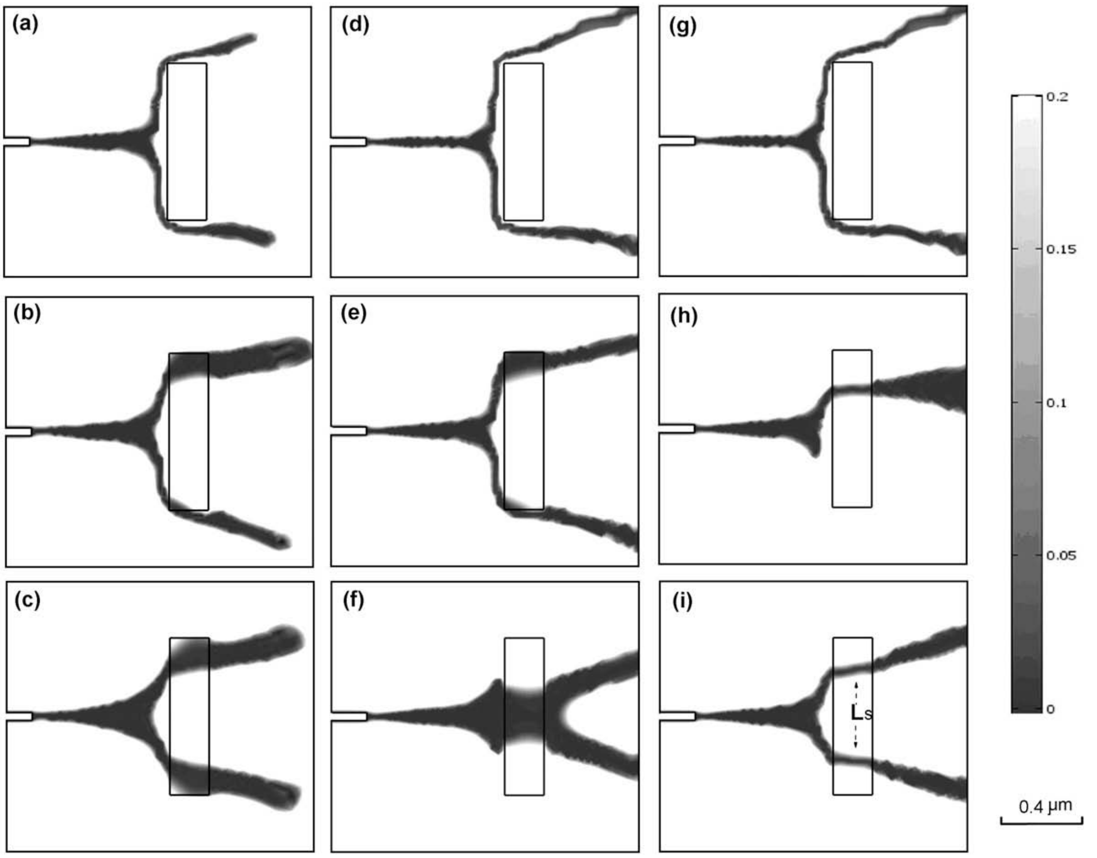

Figure 5.7 The crack propagations in different fiber-reinforced BMGs under $K = 36.5$MPam$^{1/2}$. The gray scales correspond to the values of 1-w in the BMG matrix or the values of 1-ϕ in the fiber. For parameters of the fiber: (a) $e_c = 354$ J/m^2; $\gamma_t = 10.2$ J/m^2, t = 42 ns and 45 ns; (b) $e_c = 354$ J/m^2; $\gamma_t = 5.1$ J/m^2, t = 35 ns and 40 ns; (c) $e_c = 354$ J/m^2; $\gamma_t = 2.04$ J/m^2, t = 35 ns and 40 ns; (d) $e_c = 708$ J/m^2; $\gamma_t = 4.08$ J/m^2, t = 45 ns and 50 ns; (e) $e_c = 708$ J/m^2; $\gamma_t = 3.06$ J/m^2, t = 35 ns and 40 ns; (f) $e_c = 708$ J/m^2; $\gamma_t = 2.04$ J/m^2, t = 35 ns and 40 ns.

5.4.2 Shear band propagation in tungsten fiber reinforced Zr-Based BMG

A more practical model of fiber-reinforced BMG composite is investigated where we allow the spreading of crack into the crystalline fibers. The propagation of crack in the fiber is described by Eq. (5.9). We first model one of the most important BMG composites, tungsten reinforced Zr-based BMG. We choose the modeling coefficients in Eq. (5.9) for tungsten as follows: the surface energy of tungsten is $\gamma_t = 5.1$ J/m^2 (Fu, Ohnishi et al. 1985) and the fracture energy e_{tc} is 354 J/m^2(Gumbsch, Riedle et al. 1998). The surface tension can be calculated by $D_\phi = \gamma_t R$, where $R = 2$ μm is the scale of the roughness of fracture surface. The time constant in Eq. (5.9) is $\tau = 0.02$ μs. Figure 5.6(b) shows the crack propagating through the tungsten fiber at a stress intensity factor of 36.5 MPam$^{1/2}$. The fracture toughness of this tungsten-reinforced BMG is determined to be 35 MPam$^{1/2}$, which is consistent with experiments (Conner, Dandliker et al. 1998). The result further demonstrates the phase-field modeling is useful in the investigation of BMG composite. Besides tungsten, other crystalline fibers have been used to reinforce BMGs as well. To provide some information for the choice of fibers in experiments, in what follows we quantitatively analyze the relation between the mechanical properties of fiber reinforcements and the fracture toughness of BMG composites. Figure 5.6 and 5.7 show the cracking around the fiber reinforcement with different surface energy γ_t and fracture energy e_{tc}. The relation between the fracture toughness of composite and the surface energy e_{tc} of fiber reinforcement is shown in Figure 5.8 (a). It is found that the fracture toughness of

BMG composite increases more significantly with increasing fiber surface energy when a tougher fiber (larger e_{tc}) is used. When the fracture energy e_{tc} of fiber is small, the enhance of fracture toughness of reinforced BMG can be written as

$$K_{IC} - K_{IC0} \propto \gamma_t^{\alpha}, \tag{5.10}$$

where the exponent α = 0.8-1.2 decreases with decreasing fracture energy of fiber. Eq. (5.10) can be related to the Griffith theory of brittle fracture when α = 0.5, which could occurs at very small e_{tc}. Thus Eq. (5.10) suggests choosing fibers with high surface energy to reinforce BMG, in consistent with the experimental observation.

Based on Figs. 5.6 and 5.7, four types of failures in BMG composite can be summarized as follows. (i) Type S: Shear failure characterized by the cracking of fiber reinforcement along its orientation direction (Figure 5.6 (a)). (ii) Type T: Transverse failure of fiber in its center. A crack passes straight through the fiber which is broken into half (Figure 5.6 (b)); (iii) Type R: Ramification transverse failure of fiber at several places due to the branching of shear bands. The fiber is broken into several segments (Figure 5.7 (i)). The characteristic length of the segment is defined as L_S. (iv) Type L: Longitudinal failure characterized by the spreading of shear bands close to the interface (Figure 5.7 (g)). These modes of failures can be observed in experiments in BMG composites (Conner, Dandliker et al. 1998; Qiu, Wang et al. 2002).

It is expected that the type-T failure characterized by L_S =0 may be favorable for achieving a higher fracture toughness of composite since the branching of shear bands is restricted, and at the same time the possibility that the shear bands are impeded by other nearby fibers will increase. In Figure 5.8 (b) we plot the failure segment length L_S defined in Figure 5.7 (i) of a type-R failure as a function of the stress intensity factor. Figure 5.8 (b) indicates that the type-T failure (L_S=0) can occur only in some fibers when the relation between their surface energy and fracture energy is properly tuned, *i.e.*, $\sqrt{e_{tc}\cdot\gamma_t}=60\text{J/m}^2$, suggesting a particular criterion for the selection of fiber to reinforce BMG.

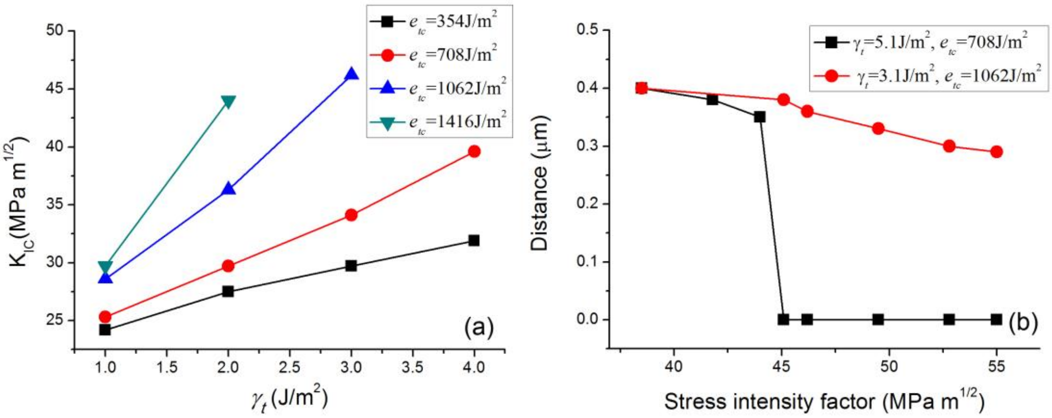

Figure 5.8 (a) The threshold stress under different γ_t and e_{tc} ; (b) The loading stress vs crack distance in the fiber

5.4.3 Influence from the interface

As shown in Figure 5.9, the simulation model of BMG composite consists of cylindrical reinforcing tungsten fibers with a diameter of d = 0.2 μm, which are embedded in a Zr-based BMG ($Zr_{41}Ti_{14}Ni_{10}Cu_{12.5}Be_{22.5}$) plate with edged notches. Tensile stresses perpendicular to the fibers are applied at the upper and lower edges of the plate with dimensions of 20 μm × 20 μm.

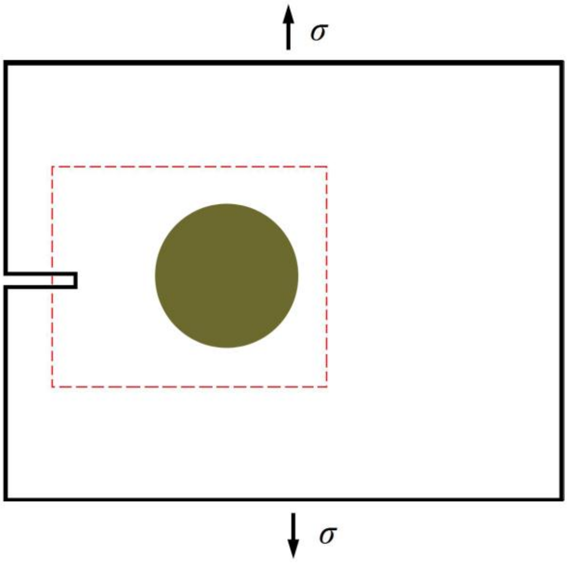

Figure 5.9 System for the simulation of shear banding in BMG composites, the shadow area represents reinforcing fiber

When the reinforcing material is introduced into BMG-matrix to form BMG composite, due to the difference of the coefficients of thermal expansion between BMG matrix and the reinforcing material, residual stress is inevitably introduced at the matrix/reinforcement interface, and usually can be estimated (Kim, Fleury et al. 2005). For example, in tungsten fiber-reinforced Zr-based BMG, tungsten and BMG-matrix have different thermal coefficients 4.5×10^{-6} and 8.5×10^{-6} K^{-1}, respectively, therefore tensile residual stress (with respect to the BMG-matrix) is likely to be introduced at the interface. However, if the reinforcement is 1080 steel fiber, compressive residual stress would be generated at the interface due to its relatively large thermal expansion coefficient 13×10^{-6} K^{-1}. In in-situ formed Zr-based BMG, the lattice constant of β-phase crystallites embedded in the BMG-matrix is 0.3496 nm (Hofmann, Suh et al. 2008), which would misfit the amorphous matrix's atomic structures, resulting in the residual stress and deformation defect at the interface as well.

The residual stresses at the interface are quantitatively considered in Eq. (5.11) based on the boundary conditions (BCs) for the displacement field **u** at the interface:

$$\mathbf{n} \cdot [(c\triangledown\mathbf{u}+a\mathbf{u}-b)_1-(c\triangledown\mathbf{u}+a\mathbf{u}-b)_2] = g \tag{5.11}$$

where c is the module matrix, **n** is the direction vector and g is the residual stress at the matrix/reinforcement interface; parameters in bracket 1 stands for the BMG-matrix, and 2 for the reinforcing material. In our simulation we set parameters a and b as zero. Figure 5.10 (a) and (d) shows the displacement field **u** around the matrix/reinforcement interface when there are compressive and tensile residual stresses at the interface, respectively. Dirichlet boundary condition for Eq. (5.6) is imposed for w at the interface, i.e., w is a constant value at the interface. Because the deformation defect field $w=w_0$ describes atomic volume dilatation in the BMG-matrix, hence w_0 measures the atomic bonding condition between the amorphous matrix and the crystalline reinforcing materials, *e.g.*, for prefect atomic bonding w_0=0, and w_0=1 for the decohesion between the BMG-matrix and the reinforcement.

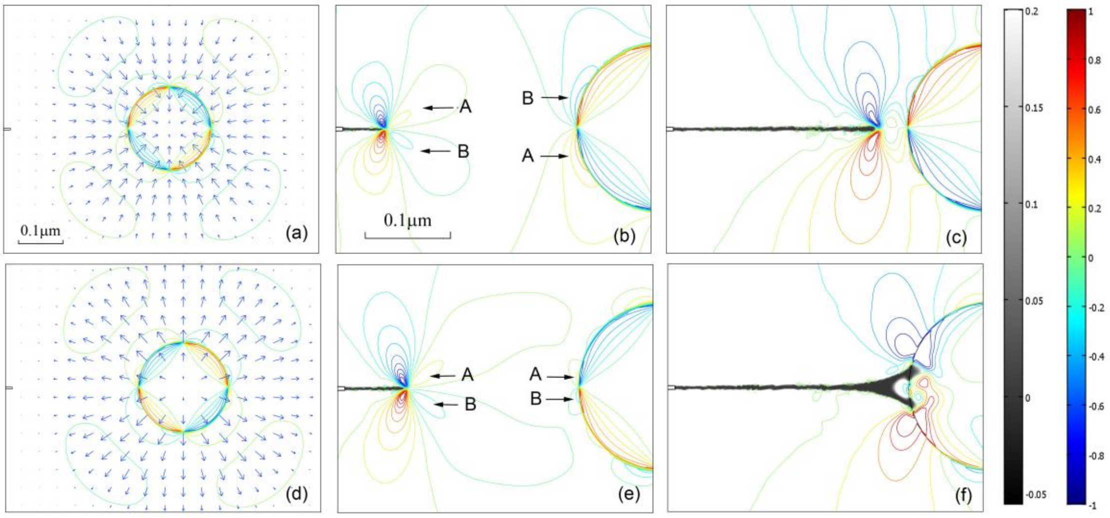

Figure 5.10 (a)-(c) Shear band propagates toward the reinforcing fiber with a compressive residual stress -260MPa at its interface at 5, 35 and 50ns, respectively; (d)-(f) shear band propagates toward the reinforcing fiber with a tensile residual stress 260MPa at its interface at 5, 35 and 50ns, respectively. The arrows in (a) and (d) represent the displacement fields. The gray scales correspond to the values of 1-*w* in the matrix; or to the value of 1-ϕ in the tungsten fiber; the contour plots with the color bars (×870MPa) are for shear stresses in the composite. The arrows A and B in (b) and (e) indicate the negative and positive shear stresses, respectively.

As shown in Figure 5.11, tensile residual stress at the interface would accelerate the propagation of shear band in the BMG-matrix, while the compressive residual stress would slow it down. These results are quite consistent with the previous experimental study conducted by Conner *et al*. (Conner, Dandliker et al. 1998), who predicted that tensile hoop stress around the interface would encourage the cracks to propagate toward the reinforcing fibers, while compressive hoop stress should deflect cracks away from the fibers. Our phase-field simulation results provide further insight views on how these two opposite residual stresses at the matrix/reinforcement interface affect the shear band propagation. If there is compression residual stress at the interface, the shear stress around the shear band approaching the reinforcement has the opposite sign as that around the reinforcement, as shown in Figure 5.10 (b) and (c). Hence shear band propagation will be decelerated (Figure 5.10 (c)) and even forced to detour the reinforcement. If there is tensile residual stress at the interface, the shear stress around the shear band approaching the reinforcement has the same sign as that around the reinforcement, as shown in Figure 5.10 (e) and (f). As a consequence the shear band will be accelerated to propagate toward the interface (Figure 5.10 (e)) and eventually triggers cracks in the crystalline reinforcement, as shown in Figure 5.10 (f).

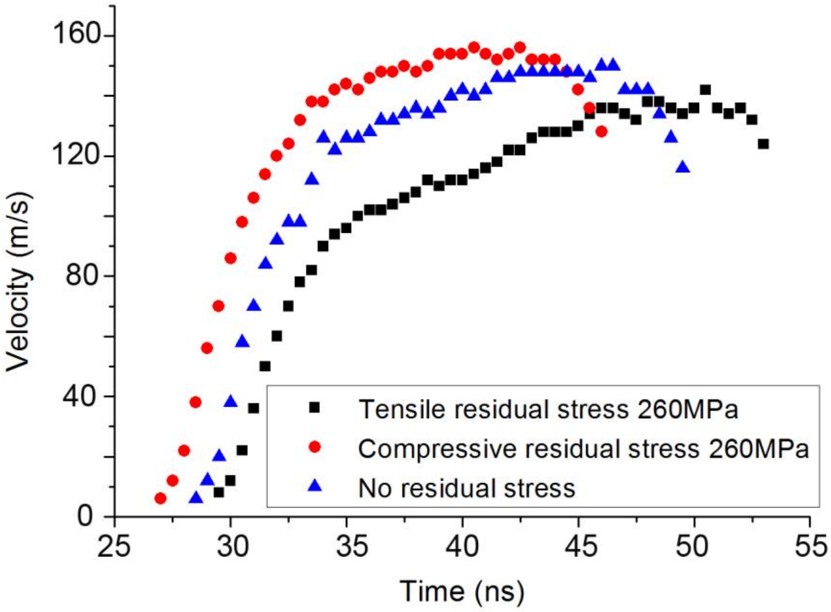

Figure 5.11 Effect of residual stress at the interface on the velocity of shear band propagating toward the fiber. The stress intensity factor is K_I = 27.5 MPam$^{1/2}$. The distance between the notch and the interface is 0.28 μm.

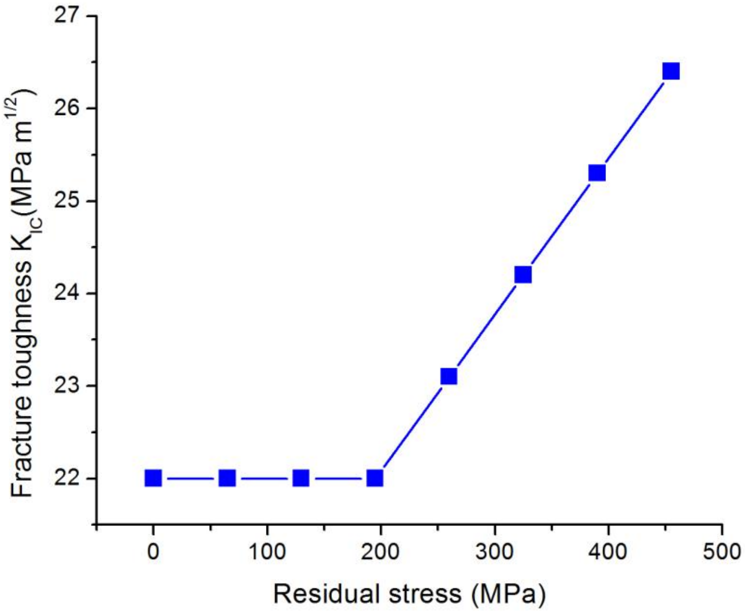

Figure 5.12 The relation between the fracture toughness of BMG composite and the compressive residual stress at the interface.

Compressive residual stress not only hinders shear band propagation, but also affects the initiation of shear band from the initial single-edge notch. Figure 5.12 shows the relation between the fracture toughness and the compressive residual stress g at the interface, when the minimum distance between the notch and the reinforcement is fixed as 0.28 μm. For the compressive residual stress g smaller than g_0 = 195 MPa, its influence on the shear band initiation is negligible. If g is larger than 195 MPa, the fracture toughness of the composite K_{IC} can be described as

$$K_{IC}= K_{IC0}+0.017|g-g_0|, \tag{5.12}$$

where K_{IC0} = 22 MPam$^{1/2}$ is the fracture toughness for shear band initiation from the notch in BMG without the reinforcement.

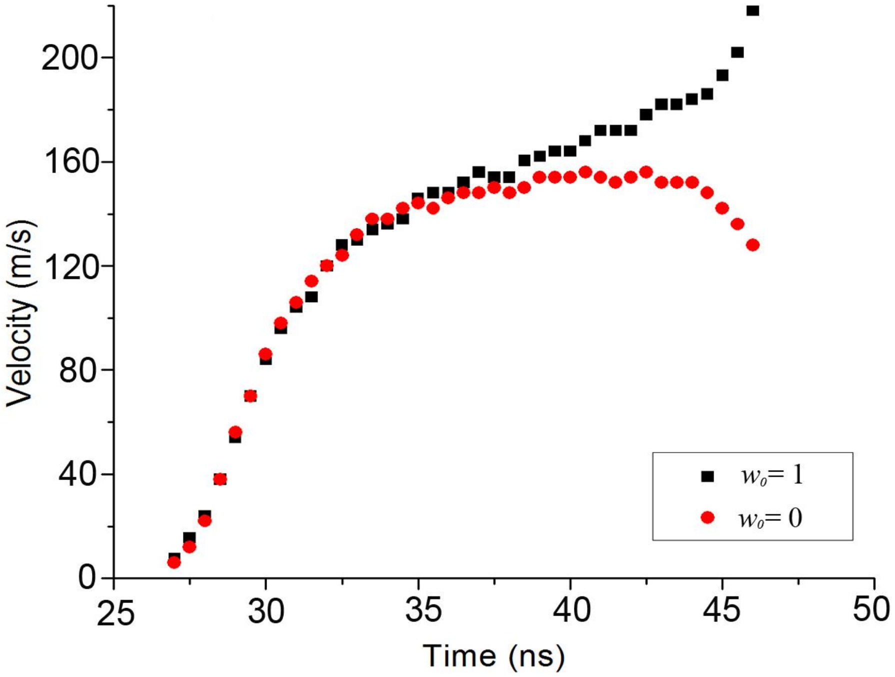

Figure 5.13 Effect of atomic bonding condition at the interface on the velocity of shear band propagating toward the fiber. The stress intensity factor is K_I = 27.5 MPam$^{1/2}$. The distance between the notch and the interface is 0.28 μm.

Based on these simulation results we can conclude that the tensile residual stress at the matrix/reinforcement interface is preferable for enhancing the plasticity of the BMG composite (Kim, Fleury et al. 2005; Hofmann, Suh et al. 2008), since the reinforcement in this case may accommodate local plastic strain triggering by the shear band, as shown in Figure 5.10 (f). Compressive residual stress would improve the fracture toughness of BMG-matrix, but it is no helpful for enhancing the plasticity of BMG. This is because shear band impeded by the reinforcement tends to detour around the reinforcement as shown in Figure 5.14 (c), resulting in the delamination and pullout of the reinforcements during the fracture process in the BMG-matrix composite.

Figure 5.13 shows the effect of atomic bonding condition at the matrix/reinforcement interface on shear banding in the BMG matrix without considering the residual stress at the interface ($g = 0$). When the shear band approaches the interface with the worse bonding condition ($w_0 = 1$), its propagation will be speeded up. If the interface has the perfect bonding condition ($w_0 = 0$), shear band propagation will slow down. On the other hand shear bands can be initiated from the interface if the bonding condition at the interface satisfies $0.6<w_0<1$ (Shen and Zheng 2010).

The effects of residual stress and atomic bonding condition at the matrix/reinforcement interface on shear banding and crack propagation can be summarized into several deformation modes as shown in Figure 5.14. If the interface between the BMG-matrix and the reinforcement has perfect adhesion ($w_0 = 0$), without residual stress ($g = 0$) shear band touching the interface would cause cracking inside the crystalline reinforcement, shown as color plots for ϕ in Figure 5.14 (a) and (b). Larger applied load would trigger shear band to split in front of the reinforcement to suspend more plastic strains as shown in Figure 5.14 (b). With compressive residual stress ($g = -435$ MPa) at the interface, shear banding tends to occur along the surface of the reinforcement as shown in Figure 5.14 (c). With tensile residual stress (g = 175 MPa) at the interface, there is a straight propagation of the shear band before it touches the interface, resulting in the crack branching inside the reinforcement as shown in Figure 5.14 (d).

For the interface with defective atomic bonding condition ($0<w_0<1$), the shear band would split into two branches and detour around the reinforcing fiber as shown in Figure 5.14 (e). Furthermore, in the worse atomic bonding condition at the interface ($w_0 = 1$), shear band propagation immediately transfers from one side of the reinforcement to the other side without any branching as shown in Figure 5.14 (f).

The above-mentioned deformation modes have been experimentally discovered in BMG composites (Fan, Li et al. 2000; Lee, Lee et al. 2004; Kim, Fleury et al. 2005; Lee and Sordelet 2006; Hofmann, Suh et al. 2008; Shen and Zheng 2010). Our simulations can quantitatively describe the occurrences of these deformation modes by characterizing the residual stresses and atomic bonding condition at the matrix/reinforcement interface, *e.g.*, through Eqs. (5.5), (5.6) and (5.11). Therefore the simulation approach developed in this study is extremely useful in the development and design of BMG-matrix composites with improved fracture toughness and ductility.

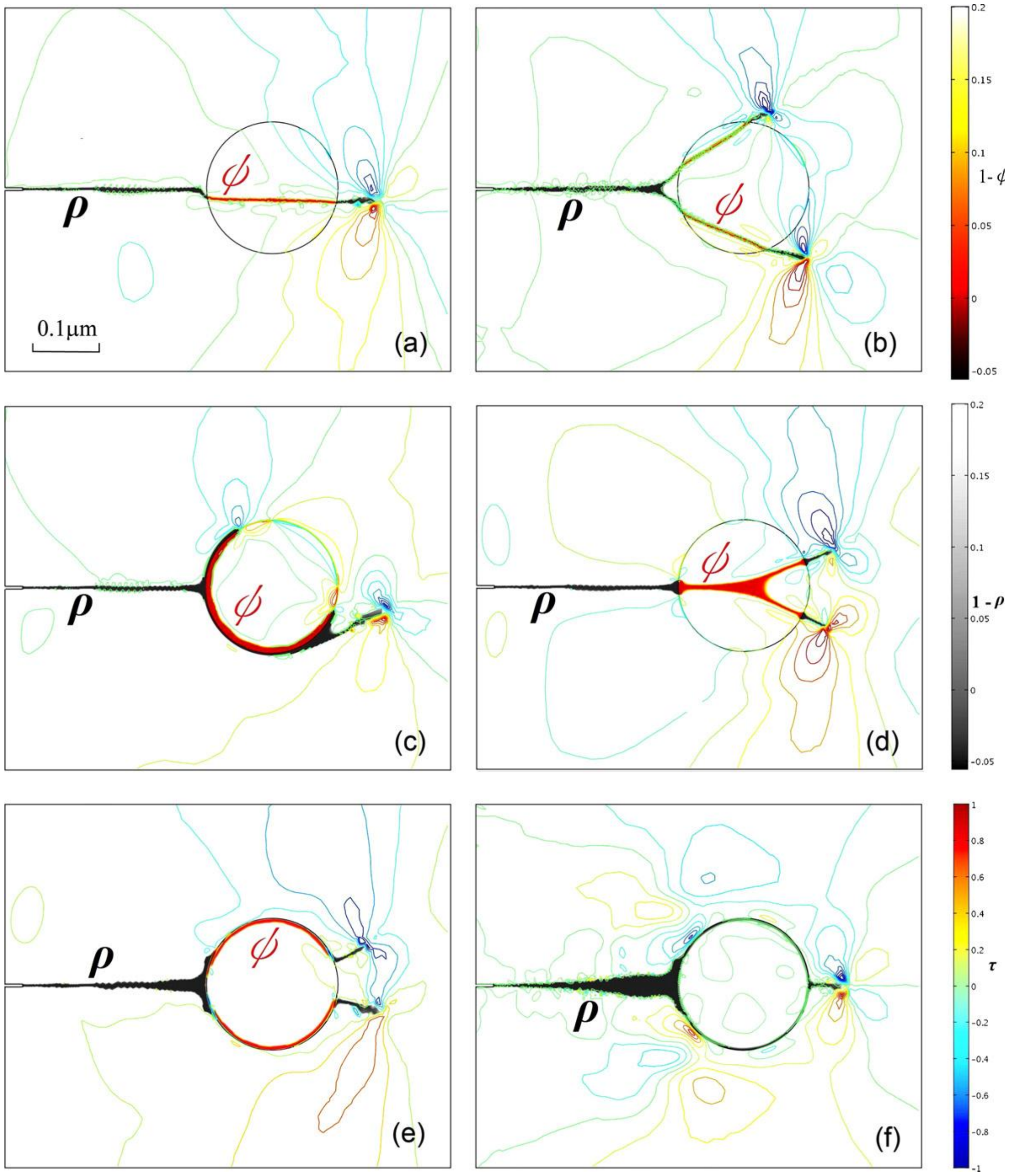

Figure 5.14 Different deformation modes for shear banding and crack propagation in the BMG composite: (a) and (b) Shear banding induced cracking inside the reinforcement after the shear band interacts with reinforcement. g = 0, w_0 = 0; K_I = 24.2 MPam$^{1/2}$ (a), and 27.5 MPam$^{1/2}$ (b); (c) propagation of shear band along the reinforcement surface with compressive residual stress g = -435 MPa; w_0 = 0; (d) shear banding induced cracking inside the reinforcement with tensile residual stress g = 175 MPa at its surface; w_0 = 0; (e) Branching of shear band along the reinforcement surface; w_0 = 0.8; g = 0. (f) Shear banding at opposite sides of the reinforcement surface; w_0 = 1; g = 0. K_I = 27.5 MPam$^{1/2}$ in (c)-(f). The defect field ϕ in BMG and crack field in tungsten is identified and their values are indicated by grey scales and color scales, respectively.

5.5 Modeling of Shear Band Multiplication and Interaction in Metallic Glass Matrix Composites

Under critical loading conditions numerous deformation defects are connected with each others to form shear bands in which the plastic strains are localized (Spaepen 1977; Inoue, Nakamura et al. 1992). Although in monolithic BMG, only elastic strain (about 2%) was found under tensile deformation due to the strain softening (Inoue, Shen et al. 2006), it has been found that in the compression deformation of monolithic BMG, shear band multiplication could be triggered by shear band interaction when shear bands meet, which increases the flowability of the plastically deformed BMG and yields a global ductility with large plastic strain (Das, Tang et al. 2005). On the other hand, in BMG-matrix composites, the crystalline reinforcements can promote the generation of multiple shear bands in BMG matrix (Schroers and Johnson 2004; Xie and George 2008). Typically the multiple shear bands prevent the catastrophe failure led by a single shear band. These mechanisms of shear band interaction and multiplications have been considered in the designs of a large number of BMG-matrix composites (Fan and Inoue 1997; He, Eckert et al. 2003; Chen, Inoue et al. 2006) with enhanced fracture toughness and ductility. In this section, phase-field modeling approach is used to simulate shear band formation, multiplication and interaction in Zr-based BMG-matrix composite (Liu, Dai et al. 2005).

5.5.1 Simulation model and stress distribution

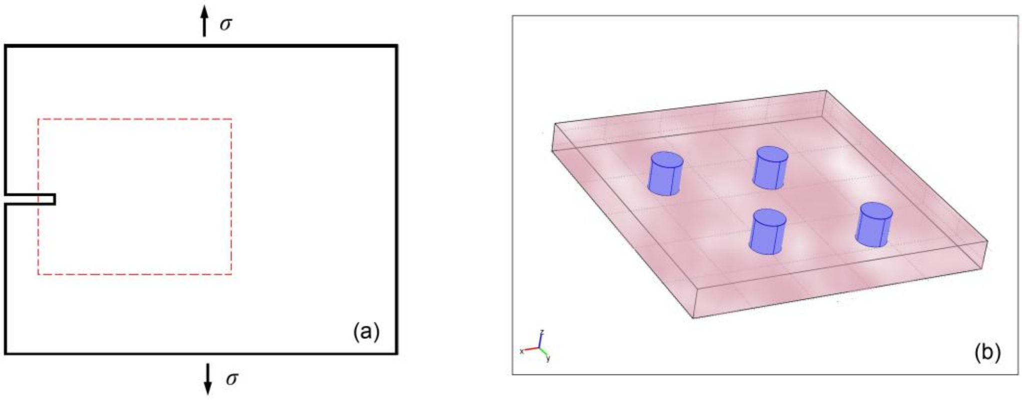

Figure 5.15 (a) System for the simulation of shear banding in BMG; (b) System for the simulation of shear band interaction and multiplication in Zr-based BMG with tungsten fiber reinforcements.

The simulation model for shear banding in BMG composite is shown in Figure 5.15 (a)-(b). Cylindric reinforcing tungsten fibers with a diameter of d = 0.5 mm are embedded in the Zr-based BMG plate with edged notches. Stress distribution around shear band is important for the analysis of shear band interaction and multiplication. This is because the plastic strain of BMG is localized in the shear bands, and stresses distributing around the shear bands would definitely influence the propagation speed and direction of shear bands. When two shear bands approach to each other, their interaction will be affected by the stress distribution around them. We first analyze the stress distribution of a straight shear band as shown in Figure 5.16 (a)-(c). As demonstrated in Figure 5.16 (a)-(c), the maxima of stresses σ_{xx} and σ_{yy} are in the front of the shear band. The maximum and the minimum of the shear stress σ_{xy} locate at two sides of the shear band. Stress distributions around the shear band are summarized in Figure 5.16 (d). If all the stress components symmetrically distribute around the shear band, the shear band will propagate in a straight manner.

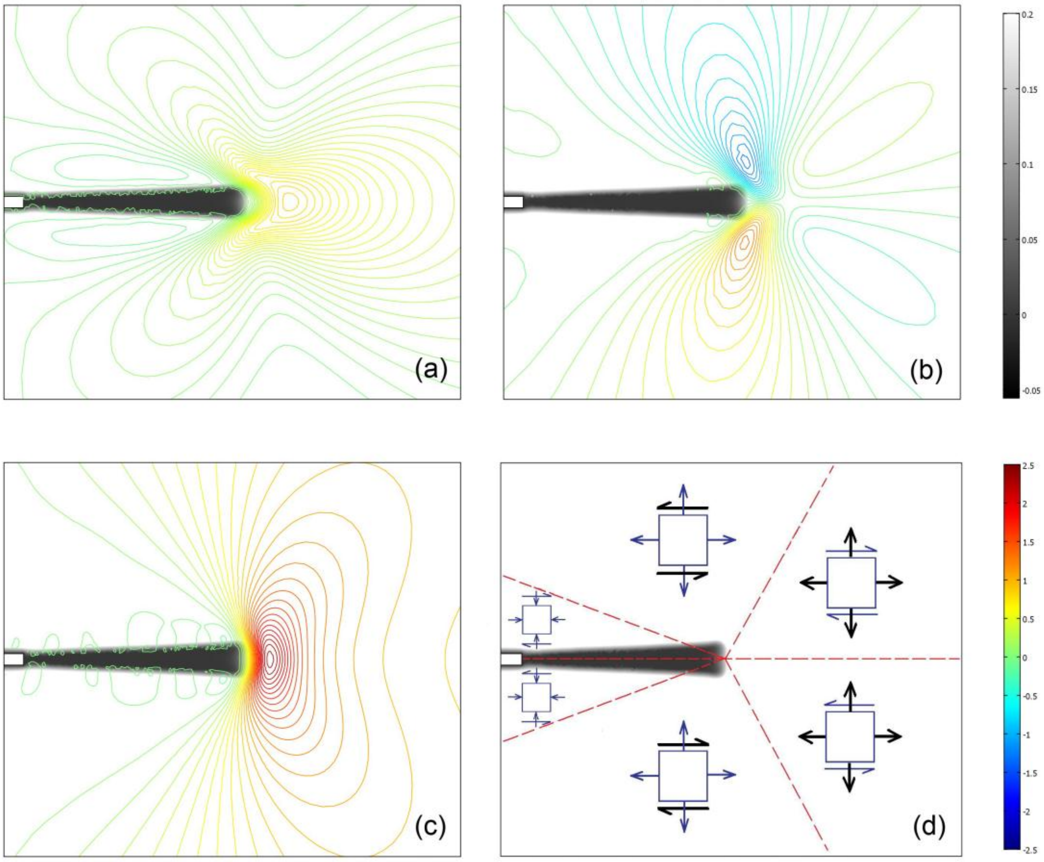

Figure 5.16 Stress distribution of σ_{xx}, σ_{xy}, and σ_{yy} around a straight shear band; (d) indication of stress around the shear band with symbols. The gray scales correspond to the values of 1-*w* in the BMG matrix or the values; The color bars (×870MPa) are for the contour plots of stresses.

5.5.2 Shear band multiplication

In BMG-matrix composite, the bonding condition between the BMG matrix and reinforcement is one of the major concerns for shear band initialization and propagation. The preparation of BMG composite may introduce defects at the interface, where shear bands can be initiated under certain loading conditions. We consider the system as described in Figure 5.15 (b). We impose the Dirichlet boundary conditions on Eq. (5.6) by considering the atomic dilatation volume at the interface as a constant deformation defect density w_0, *i.e.*, $w_0(\mathrm{r}) = w$ at the interface. We define the fracture toughness $\mathrm{K}_{\mathrm{IC}} = \sigma_c \sqrt{\pi d}$, where σ_c is the critical applied stress when the shear band is initiated from the interface. Figure 5.17 (a) shows the relationship between the fracture toughness and the deformation defect density at the interface, which can be described as

$$K_{\mathrm{IC}}\text{-}K_{\mathrm{IC0}} \propto (1\text{-}w_0)^b, \tag{5.12}$$

where b = 1.6. When w_0 =1 the shear bands would be easily initiated from the interface, resulting in a fracture toughness of $\mathrm{K}_{\mathrm{IC0}}$ = 22.4 MPa m$^{1/2}$. It is also found that if the deformation density at the interface is small, *e.g.*, $w_0<0.4$, which suggests good bonding between the BMG matrix and the reinforcements, the shear band can not be initiated from the interface and the fracture toughness of the composite is significantly enhanced. Considering the worst bonding condition between the BMG matrix and the reinforcing fibers, *i.e.*, w_0 = 1, the relation between the applied stress measured by the stress intensity factor $\mathrm{K}_{\mathrm{I}} = \sigma_c \sqrt{\pi d}$ and the number of shear bands emitted from the interface is shown in Figure 5.17 (b). In this case Figure 5.18 (a) shows the shear bands initiated from the interface and the shear stress distribution around them when K_{I} = 50 MPa m$^{1/2}$. The distribution of shear bands around the reinforcement is similar to that of the edge dislocations emitted from the reinforcement in the fiber-reinforced crystalline materials (Janssen, Zuidema et al. 2004) as shown in Figure 5.18 (b). Such similarity suggests that the shear bands can interact with each other depending on the stress states around them.

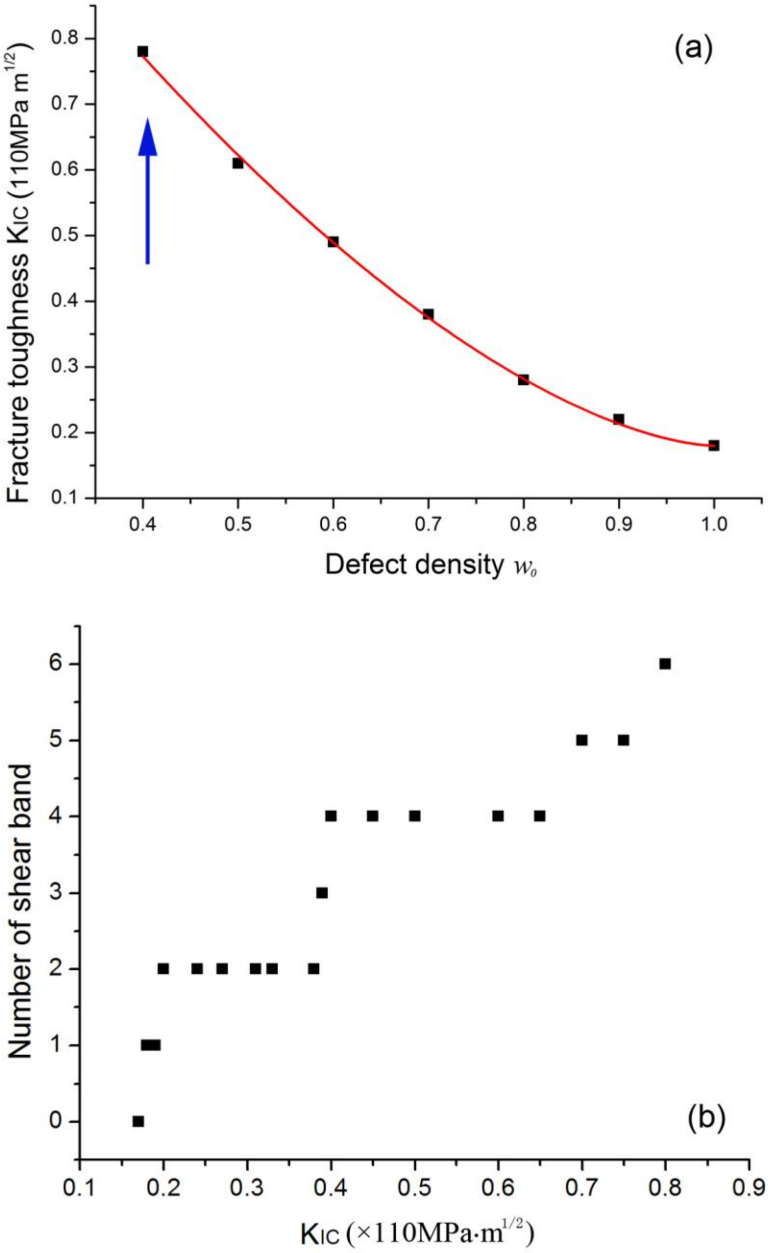

Figure 5.17 (a) The relation between fracture toughness and deformation defect density at the interface between BMG and reinforcements. The red line is the fits of Eq. (5.1). The arrow indicates the significant increase of fracture toughness when w_0<0.4. (b) Number of shear bands under different stress intensity factor.

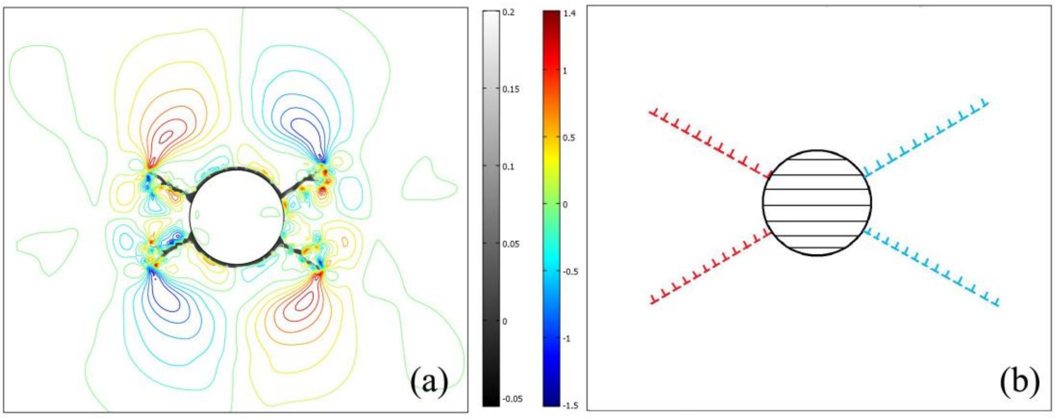

Figure 5.18 (a) The shear bands emitted from the BMG-reinforcement interface and the shear stresses around the shear bands. (b) The schematic of the distribution of edge dislocations in fiber-reinforced crystalline materials. Gray scales for 1-*w* and color scales for the contour plots of shear stresses are the same as those in Figure 5.3.

5.5.3 Shear band interaction

When two shear bands meet, due to the changes of their shear stresses, the shear bands will be either deflected or attracted as shown in Figure 5.19 (a) and 5.19 (b) respectively. The deflection and attraction of shear bands occur only when shear stresses of two interacting shear bands are affected by each other. When the shear stresses near the approaching parts of two shear bands have opposite signs as marked by arrows A in Figure 5.19 (a), the deflection (indicated by arrows B) occurs. When the shear stresses near the approaching parts of two shear bands have the same sign as marked by arrows C in Figure 5.19 (b), two shear bands attract with each other and finally integrate together to form a loop, as indicated by arrows D in Figure 5.19 (b). The formation of such shear band loop results in the suspension of shear band propagation. Hence the attraction between two shear bands could impede the motions of shear bands.

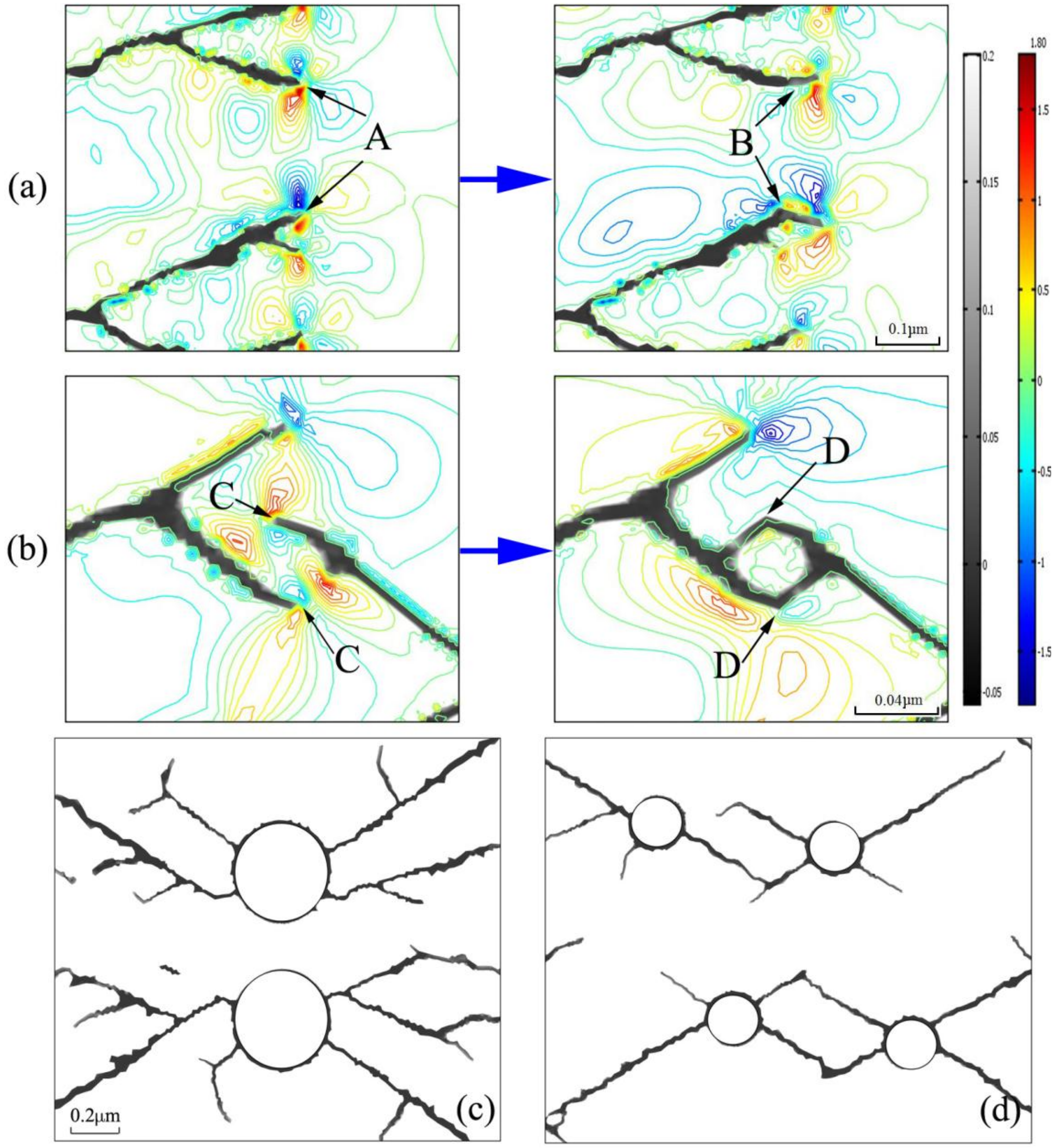

Figure 5.19 Interaction between two shear bands. (a) The process of shear band deflection. (b) The process of shear band attraction. The arrangement of reinforcing fibers in the BMG matrix will result in either shear band deflection (c) or shear band integration (d). The gray bars and color bars have the same meanings as those in Figure 5.3.

The properties of shear band interaction can facilitate the design of fiber-reinforced BMG-matrix composite with improved ductility and fracture toughness. If a number of reinforcing fibers are arranged along the direction of the applied stress, shear bands emitted from the interface tend to deflect with each other as shown in Figure 5.19 (c). If there are reinforcing fibers arranged along the direction perpendicular to the applied stress, shear bands emitted from nearby fibers tend to integrate and are locked as shown in Figure 5.19 (d), which could enhance the ductility and fracture toughness of the composite.

5.6 Formation of secondary shear bands

When two shear bands integrate with each other, their propagations are suspended and the secondary shear bands would be initiated from the intersection points to accommodate more plastic stains, as shown in Figure 5.20. If two shear bands integrate with an obtuse angle as shown in Figure 5.20 (a), there will be only one new secondary shear band which propagates upward. If shear bands integrate with a straight angle, there will be two secondary shear bands initiated from the intersection point as shown in Figure 5.20 (b). Such behaviors of secondary shear band generation are related to the stress states (Figure 5.16(d)) of two approaching major shear bands and how the shear stress distributions change when shear bands meet, demonstrating by the contour plots of the shear stresses before and after the shear band integration (Figure 5.20). Moreover, as indicated by a dash rectangle in Figure 5.20 (b), the cross shaped shear band consisting of major shear band and secondary shear band looks like a “step”, which is similar with those observed in plastically deformed BMG composites (Kim, Das et al. 2006; Hofmann, Suh et al. 2008). Because the propagations of major shear bands are suspended after the integration, the probability of catastrophe failure of BMG composite is reduced. On the other hand the generation of secondary shear band can sustain more plastic strains, thus improve the overall plasticity of the BMG composites.

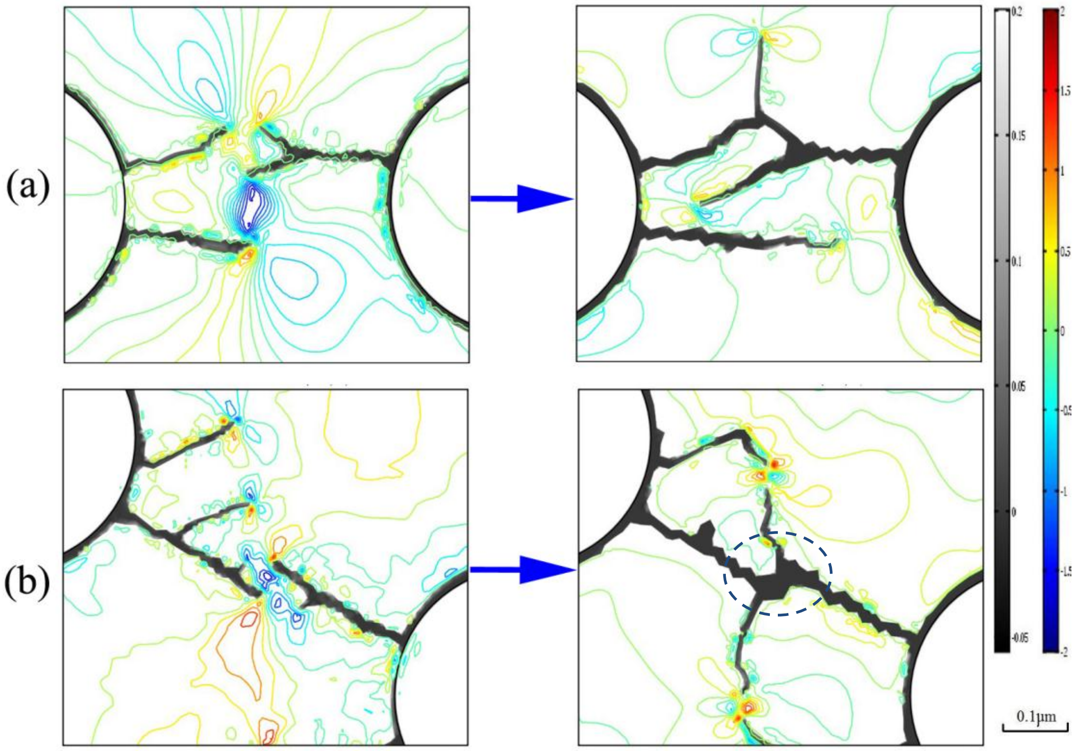

Figure 5.20 The formation of secondary shear bands during the interaction of two major shear bands. (a) Formation of one secondary shear band marked by a dash circle; (b) Formation of two secondary shear bands marked by dash circles. The gray bars and color bars have the same meanings as those in Figure 5.3.

5.7 Conclusion

We studied systematically the shear banding and shear band propagation in metallic glasses and fiber-reinforced metallic glass composites using continuum mesoscopic phase-field model. Fracture in tungsten-reinforced BMG composite is investigated. The fracture toughness and the modes of failure obtained from the simulation are consistent with experiments, suggesting the successful application of the phase-field approach on the understanding of shear banding and fracture processes of practical BMG composites. The relations between the fracture toughness of BMG composite and the fracture energy and surface energy of the fiber reinforcements are characterized. These simulation results may provide useful information for the design and fabrication of BMG composites.

Besides, it is found the tensile residual stress at the interface between BMG-matrix and the reinforcement is preferred for the purpose of enhancing the plasticity of the BMG composite, while the compressive residual stress would improve its fracture toughness. Furthermore, the residual stress and atomic bonding condition at the interface can be used to determine the deformation modes in the BMG-matrix composite. The simulation results are all consistent with those from the experimental investigations, suggesting that the modeling could provide guidance for materials selection and preparation for high performance BMG composites.

Based on phase-field model of shear banding in metallic glasses, we investigated the shear band interaction and multiplication in Zr-based BMGs reinforced with tungsten fibers. Multiple shear bands can be initiated from the interface between the reinforcements and the BMG matrix. The enhanced fracture toughness of the composite is related to the bonding conditions between the BMG and the reinforcement and its relation with the defects at the interface is quantitatively determined. The deflection and attraction of two meeting shear bands occur depending on the signs of shear stresses near the approaching parts of these shear bands. From the simulation study it is found that the integration of two attracting shear bands will result in the generation of secondary shear bands. It is remarkable that the shear band multiplication and the generation of secondary shear bands could enhance the plasticity or fracture toughness of the BMG composites and the modeling could be a useful tool for the design of strong and ductile BMG composites. Moreover the simulation further suggests that the appearance of a cross shape in shear band consisting of both the major and secondary shear bands could be the explanation on the formation of shear band "steps" experimentally observed in the plastically deformed BMG composite.

6. Conclusions

The structural and energetic properties of as-synthesized defects and deformation defects in metallic glasses are investigated in this thesis using dynamic mechanical analysis. The experimental results facilitate the development of computational methods for the simulation of plastic deformation in metallic glasses.

Atomic CSRO and TSRO rearrangements in metallic glasses are illustrated through internal friction studies. Internal frictions of samples after thermal annealing at different temperature vary due to different resulting states achieved by metallic glasses. As-synthesized defects in the ideal glass matrix can be annihilated through structural variation. We examine the structural variations using index n, which is an exponent describing the relation between internal friction and dynamic frequency. Irreversible structural relaxation, slow β relaxation and primary α relaxation show different features with index n. Annealing at sub-T_g would cause irreversible structural relaxation which annihilates defects generated from rapid quenching and change the glassy matrix into ideal glassy states. This irreversible structural relaxation is different from the reversible β relaxation, which is a universal feature of metallic glasses occurring through the relaxation of confined atoms. It is found a maximum index n is associated with the β relaxation. Above T_g, α relaxation occurs, which induces the transformation from glass to supercooled liquid. Similar index n of 0.25-0.28 is found to be associated with α relaxation.

In addition to the investigations on as-synthesized defects, dynamic mechanical analysis of metallic glass after homogeneous deformation is also conducted to explore the internal friction (IF) of deformation defects in metallic glass. The IF of deformation defects shows first-order phase transition characteristics by comparing the deformed samples with their unreformed references. The activation energy and interfacial energy of deformation defects in Pd-Si metallic glasses are measured to be 2.48 eV and 1.02 J/m^2 respectively. The results demonstrate that the thermal or mechanical activation of deformation defects is a process of first-order phase transition with distinct features of the structural changes compared with those of β and α relaxation. Clarifying the features of deformation defects in metallic glasses and obtaining those important parameters about their activation could facilitate the theoretical description and computational modeling on the atomistic details of plastic deformation in metallic glasses.

Based on experimental studies on the deformation defects in the metallic glasses, mesoscopic phase field modeling with necessary parameters obtained from the IF measurements is applied to characterize the mechanical properties of metallic glasses. The deformation caused by shear banding in metallic glass ribbon Pd-Si is studied by the phase field model. Using this model, we further systematically investigate the shear banding, crack initiation and propagation in fiber-reinforced bulk metallic glasses. We find that the enhanced fracture toughness is related to the effects of reinforcements on the cracking speed and stress distributions near the reinforcement/matrix interface. The effects of fibers' length and orientation on the fracture toughness can be well described by the micromechanics models for composite materials. Fracture in tungsten-reinforced BMG composite is also investigated. The fracture toughness and the modes of failure obtained from the simulation are consistent with experiments, suggesting the successful application of the phase-field approach on the understanding of shear banding and fracture processes in the BMG composites. In the modeling of BMG composites, multiple shear bands can be initiated from the interface between the reinforcements and the BMG matrix. The enhanced fracture toughness of the composite is found to relate to the bonding conditions between the BMG and the reinforcements and its relation with the defect at the interface is quantitatively determined. From the simulation study it is found that secondary shear band can be generated from the integration of two attracting shear bands. It is remarkable that the shear band multiplication and the generation of secondary shear bands could enhance the plasticity or fracture toughness of the BMG composites. Moreover the simulation further suggests that the appearance of a cross shape in shear band consisting of both the major and secondary shear bands could be the explanation on the formation of shear band "steps" experimentally observed in the plastically deformed BMG composites.

In summary, this thesis provides a deep understanding about defects, especially the deformation defects in metallic glasses. Based on the features of activation process of deformation defects in metallic glasses and their important parameters such as activation energy and interfacial energy, theoretical description on the atomistic details of localized plastic deformation in metallic glasses is developed. With continuum mesoscopic phase-field modeling, more information about deformation of BMGs and BMG composites can be manifested, which facilitates us to search high performance BMG or BMG composites for engineering application.

Bibliography

Argon, A. (1979). "Plastic deformation in metallic glasses." Acta Metallurgica **27**(1): 47-58.

Bei, H., S. Xie, et al. (2006). "Softening caused by profuse shear banding in a bulk metallic glass." Physical Review Letters **96**(10): 105503.

Bennett, D. W. (2010). Understanding single-crystal X-Ray crystallography, Wiley-VCH.

Bernal, J. D. (1964). "The Bakerian Lecture, 1962. The Structure of Liquids." Proceedings of the Royal Society of London. Series A. Mathematical and Physical Sciences **280**(1382): 299-322.

Bernal, J. D. (1960). "Geometry of the structure of monatomic liquids." Nature **185**(4706): 3.

Bidaux, J. E., R. Schaller, et al. (1989). "Study of the hcp-fcc Phase Transition in Cobalt by Acoustic Measurements." Acta Metallurgica **37**(3): 803-811.

Branagan, D., J. Zhou, et al. (2010). "Achieving usable ductility in Glassy Nanomaterials." Advanced Materials & Process: **168**(10): 25-31

Brothers, A. H. and D. C. Dunand (2005). "Ductile bulk metallic glass foams." Advanced Materials **17**(4): 484-486.

Cahn, R., N. Pratten, et al. (1983). "Studies of relaxation of metallic glasses by dilatometry and density measurements", MRS Proceedings **28**: 241-252

Cai, B., L. Shang, et al. (2004). "Mechanism of internal friction in bulk $Zr_{65}Cu_{17.5}$ Ni_{10} $Al_{7.5}$ metallic glass." Physical Review B **70**(18): 184208.

Callister, W. D. and D. G. Rethwisch (2007). Materials science and engineering: an introduction, Wiley New York.

Cao, Q., J. Li, et al. (2005). "Free-volume evolution and its temperature dependence during rolling of Cu60Zr20Ti20 bulk metallic glass." Applied Physics Letters **87**(10): 101901.

Chaudhari, P., A. Levi, et al. (1979). "Edge and Screw Dislocations in an Amorphous Solid." Physical Review Letters **43**(20): 1517-1520.

Chekhovskoi, V. Y. and V. Peletsky (2011). "On Relaxation of point defects in metals." High Temperature **49**(1): 45-54.

Chen, D., M. Sixta, et al. (2000). "Role of the grain-boundary phase on the elevated-temperature strength, toughness, fatigue and creep resistance of silicon carbide sintered with Al, B and C." Acta Materialia **48**(18-19): 4599-4608.

Chen, H., Y. He, et al. (1994). "Deformation-induced nanocrystal formation in shear bands of amorphous alloys." Nature **367**(6463): 541-543.

Chen, H. and D. Turnbull (1969). "Formation, stability and structure of palladium-silicon based alloy glasses." Acta Metallurgica **17**(8): 1021-1031.

Chen, L., A. Setyawan, et al. (2008). "Free-volume-induced enhancement of plasticity in a monolithic bulk metallic glass at room temperature." Scripta Materialia **59**(1): 75-78.

Chen, M. (2008). "Mechanical behavior of metallic glasses: microscopic understanding of strength and ductility." Annual Review of Materials Research 38: 445-469.

Chen, M., I. Dutta, et al. (2001). "Kinetic evidence for the structural similarity between a supercooled liquid and an icosahedral phase in $Zr_{65}Al_{7.5}Ni_{10}Cu_{12.5}Ag_5$ bulk metallic glass." Applied Physics Letters **79**(1): 42-44.

Chen, M., A. Inoue, et al. (2000). "Formation of icosahedral quasicrystals in an annealed $Zr_{65}Al_{7.5}Ni_{10}Cu_{12.5}Ag_5$ metallic glass." Philosophical Magazine Letters **80**(4): 263-269.

Chen, M., A. Inoue, et al. (2000). "Quasicrystals and nano-quasicrystals in annealed ZrAlNiCuAg metallic glasses." Intermetallics **8**(5-6): 493-498.

Chen, M., A. Inoue, et al. (2006). "Extraordinary plasticity of ductile bulk metallic glasses." Physical Review Letters **96**(24): 245502.

Cheng, Y., A. Cao, et al. (2009). "Correlation between the elastic modulus and the intrinsic plastic behavior of metallic glasses: The roles of atomic configuration and alloy composition." Acta Materialia **57**(11): 3253-3267.

Conner, R., R. Dandliker, et al. (1998). "Mechanical properties of tungsten and steel fiber reinforced $Zr_{41.25}Ti_{13.75}Cu_{12.5}Ni_{10}Be_{22.5}$ metallic glass matrix composites." Acta Materialia **46**(17): 6089-6102.

Dai, L., M. Yan, et al. (2005). "Adiabatic shear banding instability in bulk metallic glasses." Applied Physics Letters **87**(14): 141916.

Das, J., M. B. Tang, et al. (2005). "“Work-Hardenable” Ductile Bulk Metallic Glass." Physical Review Letters **94**(20): 205501.

Debenedetti, P. G. and F. H. Stillinger (2001). "Supercooled liquids and the glass transition." Nature **410**(6825): 259-267.

Delogu, F. (2011). "Irreversible atomic rearrangements in elastically deformed metallic glasses." Intermetallics **19**(1): 86-92.

Demetriou, M. D. and W. L. Johnson (2004). "Shear flow characteristics and crystallization kinetics during steady non-isothermal flow of Vitreloy-1." Acta Materialia **52**(12): 3403-3412.

Dmowski, W., C. Fan, et al. (2007). "Structural changes in bulk metallic glass after annealing below the glass-transition temperature." Materials Science and Engineering: A **471**(1-2): 125-129.

Dmowski, W., T. Iwashita, et al. (2010). "Elastic Heterogeneity in Metallic Glasses." Physical Review Letters **105**(20): 205502.

Dyre, J. C. (2006). "Colloquium: The glass transition and elastic models of glass-forming liquids." Reviews of Modern Physics **78**(3): 953-972.

Egami, T. (1981). "Structural relaxation in metallic glasses." Annals of the New York Academy of Sciences **371**(1): 238-251.

Fan, C. and A. Inoue (1997). "Improvement of mechanical properties by precipitation of nanoscale compound particles in Zr-Cu-Pd-Al amorphous alloys." Materials Transactions, JIM(Japan) **38**(12): 1040-1046.

Fan, C., C. Li, et al. (2000). "Deformation behavior of Zr-based bulk nanocrystalline amorphous alloys." Physical Review B **61**(6): 3761-3763.

Fan C, P. K. Liaw, et al. (2009) "Atomistic model of amorphous materials", Intermetallics **17**:86-87.

Frank, F. (1952). "Supercooling of liquids." Proceedings of the Royal Society of London. Series A, Mathematical and Physical Sciences **215**(1120): 43-46.

Fu, C., S. Ohnishi, et al. (1985). "All-electron local-density determination of the surface energy of transition metals: W (001) and V (001)." Physical Review B **31**(2): 1168.

Gaskell, P. (1978). "A new structural model for transition metal–metalloid glasses." Nature **276**(5687): 484-485.

Gaskell, P. (1979). "A new structural model for amorphous transition metal silicides, borides, phosphides and carbides." Journal of Non-crystalline Solids **32**(1-3): 207-224.

Gaskell, P. H. (2005). "Medium-range structure in glasses and low-< i> Q</i> structure in neutron and X-ray scattering data." Journal of Non-crystalline Solids **351**(12): 1003-1013.

Gerlin, R., F. Schimansky, et al. (1988). "Ductilization of brittle amorphous alloys and reversible changes of the free volume by thermal treatments." Scripta Metallurgica **22**(8): 1291-1295.

Gilbert, C., R. Ritchie, et al. (1997). "Fracture toughness and fatigue-crack propagation in a Zr–Ti–Ni–Cu–Be bulk metallic glass." Applied Physics Letters **71**(4): 476-478.

Gilman, J. (1965). "Dislocation mobility in crystals." Journal of Applied Physics **36**(10): 3195-3206.

Gilman, J. (1973). "Flow via dislocations in ideal glasses." Journal of Applied Physics **44**(2): 675-679.

Gilman, J. J. (1975). "Mechanical behavior of metallic glasses." Journal of Applied Physics **46**(4): 1625-1633.

Gumbsch, P., J. Riedle, et al. (1998). "Controlling factors for the brittle-to-ductile transition in tungsten single crystals." Science **282**(5392): 1293-1295.

Guo, H., P. Yan, et al. (2007). "Tensile ductility and necking of metallic glass." Nature Materials **6**(10): 735-739.

Guoan, W., N. Cowlam, et al. (1984). "An investigation of the influence of cold-rolling on the structure factor of a metallic glass." Journal of Materials Science **19**(4): 1374-1384.

Harmon, J. S., M. D. Demetriou, et al. (2007). "Anelastic to plastic transition in metallic glass-forming liquids." Physical Review Letters **99**(13): 135502.

He, G., J. Eckert, et al. (2003). "Novel Ti-base nanostructure-dendrite composite with enhanced plasticity." Nature Materials **2**(1): 33-37.

Hirth, J. P. and J. Lothe (1982). Theory of dislocations John Wiley and Sons, Inc., New York.

Hofmann, D. C., J. Y. Suh, et al. (2008). "Designing metallic glass matrix composites with high toughness and tensile ductility." Nature **451**(7182): 1085-1089.

Hofmann, D. C., J. Y. Suh, et al. (2008). "Development of tough, low-density titanium-based bulk metallic glass matrix composites with tensile ductility." Proceedings of the National Academy of Sciences **105**(51): 20136.

Hufnagel, T., C. Fan, et al. (2002). "Controlling shear band behavior in metallic glasses through microstructural design." Intermetallics **10**(11-12): 1163-1166.

Hui, X., R. Gao, et al. (2008). "Short-to-medium-range order in $Mg_{65}Cu_{25}Y_{10}$ metallic glass." Physics Letters A **372**(17): 3078-3084.

Ichitsubo, T., E. Matsubara, et al. (2005). "Glass-liquid transition in a less-stable metallic glass." Physical Review B **72**(5): 052201.

Inoue, A., T. Nakamura, et al. (1992). "Mg-Cu-Y bulk amorphous alloys with high tensile strength produced by a high-pressure die casting method." Materials Transactions, JIM(Japan) **33**(10): 937-945.

Inoue, A., T. Negishi, et al. (1998). "High packing density of Zr-and Pd-based bulk amorphous alloys." Materials Transactions, JIM(Japan) **39**(2): 318-321.

Inoue, A., B. Shen, et al. (2006). "Developments and applications of bulk glassy alloys in late transition metal base system." Materials transactions **47**(5): 1275-1285.

Inoue, C. S. a. A. (2010). Bulk Metallic Glasses, CRC Press, Taylor & Francis Group.

Jakse, N., O. Lebacq, et al. (2004). "Ab Initio Molecular-Dynamics Simulations of Short-Range Order in Liquid $Al_{80}Mn_{20}$ and $Al_{80}Ni_{20}$ Alloys." Physical Review Letters **93**(20): 207801.

Janssen, M., J. Zuidema, et al. (2004). Fracture Mechanics. Spon Press, New York.

Jiang, W. and M. Atzmon (2003). "The effect of compression and tension on shear-band structure and nanocrystallization in amorphous $Al_{90}Fe_5Gd_5$: a high-resolution transmission electron microscopy study." Acta Materialia **51**(14): 4095-4105.

Jin, H., J. Wen, et al. (2005). "Shear stress induced reduction of glass transition temperature in a bulk metallic glass." Acta Materialia **53**(10): 3013-3020.

Johnson, W. and K. Samwer (2005). "A Universal Criterion for Plastic Yielding of Metallic Glasses with a $(T/T(\mathrm{g}))^{2/3}$ Temperature Dependence." Physical Review Letters **95**(19): 195501.

Kallay, N. (2000). Interfacial dynamics Marcel Dekker, New York.

Kanungo, B., M. Lambert, et al. (2003). "Free volume changes and crack tip deformation in bulk metallic glass alloys and their composites." MRS Proceedings **806** : MM7.1

Karma, A., D. A. Kessler, et al. (2001). "Phase-field model of mode III dynamic fracture." Physical Review Letters **87**(4): 45501.

Karma, A. and A. E. Lobkovsky (2004). "Unsteady crack motion and branching in a phase-field model of brittle fracture." Physical Review Letters **92**(24): 245510.

Kawamoto, M. and K. Ishizaki (1988). "Observation of grain boundary amorphous phase of sintered silicon nitride by Auger electron spectroscopy." Journal of Materials Science Letters **7**(11): 1193-1195.

Kelly, A. and N. H. Macmillan (1986). Strong Solids, Clarendon press, Oxford.

Khonik, V. (2001). "The kinetics of irreversible structural relaxation and rheological behavior of metallic glasses under quasi-static loading." Journal of

Non-crystalline Solids **296**(3): 147-157.

Khonik, V., K. Kitagawa, et al. (2000). "On the determination of the crystallization activation energy of metallic glasses." Journal of Applied Physics **87**(12): 8440.

Khonik, V., Y. P. Mitrofanov, et al. (2009). "Recovery of structural relaxation in aged metallic glass as determined by high-precision in situ shear modulus measurements." Journal of Applied Physics **105**(12): 123521.

Khonik, V. and L. Spivak (1996). "On the nature of low temperature internal friction peaks in metallic glasses." Acta Materialia **44**(1): 367-381.

Kim, J. J., Y. Choi, et al. (2002). "Nanocrystallization during nanoindentation of a bulk amorphous metal alloy at room temperature." Science **295**(5555): 654-657.

Kim, K., J. Das, et al. (2006). "Microscopic deformation mechanism of a Ti66.1Nb$_{13.9}$Ni4.8Cu8Sn$_{7.2}$ nanostructure-dendrite composite." Acta Materialia **54**: 3701-3711.

Kim, Y. C., E. Fleury, et al. (2005). "Origin of the simultaneous improvement of strength and plasticity in Ti-based bulk metallic glass matrix composites." Journal of Materials Research **20**: 2474-2479.

Kissinger, H. E. (1957). "Reaction kinetics in differential thermal analysis." Analytical Chemistry **29**(11): 1702-1706.

Klement, W., R. Willens, et al. (1960). "Non-crystalline structure in solidified gold–silicon alloys." Nature **187**(4740): 869-870

Koba, E., Y. V. Milman, et al. (1994). "Effect of plastic deformation and high pressure working on the structure and microhardness of metallic glasses." Acta Metallurgica **42**(4): 1383-1388.

Ladadwa, I. and H. Teichler (2006). "Low-frequency dynamical heterogeneity in simulated amorphous $Ni_{0.5}Zr_{0.5}$ below its glass temperature: Correlations with cage volume and local order fluctuations." Physical Review E **73**(3): 031501.

Leamy, H., T. Wang, et al. (1972). "Plastic flow and fracture of metallic glass." Metallurgical and Materials Transactions B **3**(3): 699-708.

Lee, J. G., D. G. Lee, et al. (2004). "In-situ microfracture observation of strip-cast Zr-Ti-Cu-Ni-Be bulk metallic glass alloys." Metallurgical and Materials Transactions A **35**(12): 3753-3761.

Lee, M. H. and D. J. Sordelet (2006). "Evidence for adiabatic heating during fracture of W-reinforced metallic glass composites." Applied Physics Letters **88**(26): 261902.

Lee, S. Y., B. Clausen, et al. (2005). "Compressive behavior of wire reinforced bulk metallic glass matrix composites." Materials Science and Engineering: A **399**(1): 128-133.

Leng, Y. and T. Courtney (1989). "Some tensile properties of metal-metallic glass laminates." Journal of Materials Science **24**(6): 2006-2010.

Lewandowski, J. and A. Greer (2005). "Temperature rise at shear bands in metallic glasses." Nature Materials **5**(1): 15-18.

Lewandowski, J., W. Wang, et al. (2005). "Intrinsic plasticity or brittleness of metallic glasses." Philosophical Magazine Letters **85**(2): 77-87.

Li, J., F. Spaepen, et al. (2002). "Nanometre-scale defects in shear bands in a metallic glass." Philosophical Magazine A **82**(13): 2623-2630.

Li, J., Z. L. Wang, et al. (2002). "Characterization of nanometer-scale defects in metallic glasses by quantitative high-resolution transmission electron microscopy." Physical Review B **65**(14): 144201.

Li, Q. K. and M. Li (2006). "Atomic scale characterization of shear bands in an amorphous metal." Applied Physics Letters **88**: 241903.

Liu, L., L. Dai, et al. (2005). "Initiation and propagation of shear bands in Zr-based bulk metallic glass under quasi-static and dynamic shear loadings." Journal of Non-crystalline Solids **351**(40): 3259-3270.

Liu, Y., C. Liu, et al. (2009). "Thermodynamic origins of shear band formation and the universal scaling law of metallic glass strength." Physical Review Letters **103**(6): 65504.

Liu, Y. H., G. Wang, et al. (2007). "Super plastic bulk metallic glasses at room temperature." Science **315**(5817): 1385.

Lowhaphandu, P. and J. Lewandowski (1998). "Fracture toughness and notched toughness of bulk amorphous alloy: Zr-Ti-Ni-Cu-Be." Scripta Materialia **38**(12).

Lu, J. and G. Ravichandran (2003). "Pressure-dependent flow behavior of $Zr_{41.2}Ti_{13.8}Cu_{12.5}Ni_{10}Be_{22.5}$ bulk metallic glass." Journal of Materials Research **18**(9): 2039-2049.

Lu, J., G. Ravichandran, et al. (2003). "Deformation behavior of the $Zr_{41.2}Ti_{13.8}Cu_{12.5}Ni_{10}Be_{22.5}$ bulk metallic glass over a wide range of strain-rates and temperatures." Acta Materialia **51**(12): 3429-3443.

Lu, Z. and C. Liu (2002). "A new glass-forming ability criterion for bulk metallic glasses." Acta Materialia **50**(13): 3501-3512.

Lu, Z., C. Liu, et al. (2004). "Effects of atomic bonding nature and size mismatch on thermal stability and glass-forming ability of bulk metallic glasses." Journal of Non-crystalline Solids **341**(1): 93-100.

Luo, W., H. Sheng, et al. (2004). "Icosahedral short-range order in amorphous alloys." Physical Review Letters **92**(14): 145502.

Malandro, D. L. and D. J. Lacks (1998). "Molecular-level mechanical instabilities and enhanced self-diffusion in flowing liquids." Physical Review Letters **81**(25): 5576-5579.

Malandro, D. L. and D. J. Lacks (1999). "Relationships of shear-induced changes in the potential energy landscape to the mechanical properties of ductile glasses." The Journal of Chemical Physics **110**: 4593-4601.

Marchesoni, F. (1995). "Internal Friction by Pinned Dislocations: Theory of the Bordoni Peak." Physical Review Letters **74**(15): 2973-2976.

Mark, J. E. (2007). Physical properties of polymers handbook, Springer Verlag, New York.

Miracle, D. B. (2004). "A structural model for metallic glasses." Nature Materials **3**(10): 697-702.

Morito, N. and T. Egami (1984). "Internal friction and reversible structural relaxation in the metallic glass $Fe_{32}Ni_{36}Cr_{14}P_{12}B_6$." Acta Metallurgica **32**(4): 603-613.

Murali, P. and U. Ramamurty (2005). "Embrittlement of a bulk metallic glass due to sub-Tg annealing." Acta Materialia **53**(5): 1467-1478.

Nasu, T., K. Nagaoka, et al. (1989). "Positron annihilation in plastically deformed ni-P amorphous alloy." Journal of the Physical Society of Japan **58**: 894.

Nishiyama, N. and A. Inoue (1997). "Flux treated Pd-Cu-Ni-P amorphous alloy having low critical cooling rate." Materials Transactions, JIM(Japan) **38**(5): 464-472.

Nishiyama, N., K. Takenaka, et al. (2006). "$Pd_{30}Pt_{17.5}Cu_{32.5}P_{20}$ alloy with low critical cooling rate of 0.067K/s." Applied Physics Letters **88**(12): 121908.

Nowick, A. S. and B. S. Berry (1972). Anelastic relaxation in crystalline solids, Academic Press, New York.

Oikawa, H., J. Koike, et al. (1997). "Effects of grain boundary amorphous phase on high-temperature ductility in alumina polycrystals." Materials Science and Engineering A **234-236**: 529-532.

Pérez-Sáez, R., V. Recarte, et al. (1998). "Anelastic contributions and transformed volume fraction during thermoelastic martensitic transformations." Physical Review B **57**(10): 5684.

Park, E. and D. Kim (2005). "Design of bulk metallic glasses with high glass forming ability and enhancement of plasticity in metallic glass matrix composites: A review." Metals and Materials International **11**(1): 19-27.

Park, E., J. Kyeong, et al. (2007). "Enhanced glass forming ability and plasticity in Mg-based bulk metallic glasses." Materials Science and Engineering A **449**: 225-229.

Park, J., H. Lim, et al. (2006). "Fracture behavior of bulk metallic glass/metal laminate composites." Materials Science and Engineering: A **417**(1): 239-242.

Pekarskaya, E., C. Kim, et al. (2001). "In situ transmission electron microscopy studies of shear bands in a bulk metallic glass based composite." Journal of Materials Research **16**(09): 2513-2518.

Peker, A. and W. Johnson (1993). "A highly processable metallic glass: $Zr_{41.2}Ti_{13.8}Cu_{12.5}Ni_{10.0}Be_{22.5}$." Applied Physics Letters **63**(17): 2342-2344.

Perez-Saez, R., V. Recarte, et al. (2000). "Analysis of the internal friction spectra during martensitic transformation by a new temperature rate method." Journal of Alloys and Compounds **310**(1-2): 334-338.

Ponnambalam, V., S. J. Poon, et al. (2004). "Fe-based bulk metallic glasses with diameter thickness larger than one centimeter." Journal of Materials Research **19**(5): 1320-1323.

Qiu, K., A. Wang, et al. (2002). "Mechanical properties of tungsten fiber reinforced ZrAlNiCuSi metallic glass matrix composite." Intermetallics **10**(11-12): 1283-1288.

Raghavan, R., P. Murali, et al. (2006). "Ductile to brittle transition in the $Zr_{41.25}Ti_{13.75}Cu_{12.5}Ni_{10}Be_{22.5}$ bulk metallic glass." Intermetallics **14**(8-9): 1051-1054.

Ravichandran, G. and A. Molinari (2005). "Analysis of shear banding in metallic glasses under bending." Acta Materialia **53**(15): 4087-4095.

Schroers, J. and W. L. Johnson (2004). "Ductile bulk metallic glass." Physical Review Letters **93**(25): 255506.

Schroers, J. and W. L. Johnson (2004). "Highly processable bulk metallic glass-forming alloys in the Pt–Co–Ni–Cu–P system." Applied Physics Letters **84**: 3666.

Schroers, J., B. Lohwongwatana, et al. (2005). "Gold based bulk metallic glass." Applied Physics Letters **87**(6): 061912.

Schuh, C. A., T. C. Hufnagel, et al. (2007). "Mechanical behavior of amorphous alloys." Acta Materialia **55**(12): 4067-4109.

Schuh, C. A. and A. C. Lund (2003). "Atomistic basis for the plastic yield criterion of metallic glass." Nature Materials **2**(7): 449-452.

Seop Kim, H., H. Kato, et al. (2004). "Finite element analysis of compressive deformation of bulk metallic glasses." Acta Materialia **52**(13): 3813-3823.

Shen, Y. and G. Zheng (2010). "Modeling of shear band multiplication and interaction in metallic glass matrix composites." Scripta Materialia **63**(2): 181-184.

Sheng, H., W. Luo, et al. (2006). "Atomic packing and short-to-medium-range order in metallic glasses." Nature **439**(7075): 419-425.

Sheng, W. (2005). "Evaluation on the reliability of criterions for glass-forming ability of bulk metallic glasses." Journal of Materials Science **40**(18): 5061-5066.

Shi, L. (1986). "Dislocation-like defects in an amorphous Lennard-Jones solid."

Materials Science and Engineering **81**: 509-514.

Shimizu, F., S. Ogata, et al. (2007). "Theory of shear banding in metallic glasses and molecular dynamics calculations." Materials Transactions **48**(11): 2923-2927.

Slipenyuk, A. and J. Eckert (2004). "Correlation between enthalpy change and free volume reduction during structural relaxation of $Zr_{55}Cu_{30}Al_{10}Ni_5$ metallic glass." Scripta Materialia **50**(1): 39-44.

Song, S. and T. Nieh (2009). "Flow serration and shear-band viscosity during inhomogeneous deformation of a Zr-based bulk metallic glass." Intermetallics **17**(9): 762-767.

Spaepen, F. (1977). "A microscopic mechanism for steady state inhomogeneous flow in metallic glasses." Acta Metallurgica **25**(4): 407-415.

Spaepen, F. (2006). "Must shear bands be hot." Nature Material **5**: 7-8.

Stillinger, F. H. (1995). "A topographic view of supercooled liquids and glass formation." Science **267**(5206): 1935-1939.

Suh, D., R. H. Dauskardt, et al. (2003). "Temperature dependence of positron annihilation in a Zr-Ti-Ni-Cu-Be bulk metallic glass." Journal of materials research **18**(9): 2021-2024.

Sun, G., G. Chen, et al. (2007). "Comparison of microstructures and properties of Zr-based bulk metallic glass composites with dendritic and spherical bcc phase precipitates." Intermetallics **15**(5-6): 632-634.

Takeuchi, S. and K. Edagawa (2011). "Atomistic simulation and modeling of localized shear deformation in metallic glasses." Progress in Materials Science

56(6): 785–816

Thamburaja, P. and R. Ekambaram (2007). "Coupled thermo-mechanical modelling of bulk-metallic glasses: theory, finite-element simulations and experimental verification." Journal of the Mechanics and Physics of Solids **55**(6): 1236-1273.

Turnbull, D. and M. H. Cohen (1961). "Free-volume model of the amorphous phase: glass transition." The Journal of Chemical Physics **34**: 120.

Turnbull, D. and M. H. Cohen (1970). "On the free-volume model of the liquid-glass transition." The Journal of Chemical Physics **52**(6): 3038.

Tyagi, S. and A. Lord (1979). "Internal friction and shear modulus of certain metallic glasses." Journal of Non-crystalline Solids **30**(3): 273-283.

Underhill-Lee, M. and A. Wolfenden (1992). "Some mechanical properties of a laminated metallic glass-epoxy composite." Journal of Materials Science Letters **11**(1): 13-14.

Vereshchagin, M. and O. Ostrikov (2003). "Dislocation model of polysynthetic shear bands in amorphous materials." Journal of Applied Mechanics and Technical Physics **44**(3): 438-441.

Wada, T., M. Kinaka, et al. (2006). "Effect of volume fraction and geometry of pores on mechanical properties of porous bulk glassy $Pd_{42.5}Cu_{30}Ni_{7.5}P_{20}$ alloys." Journal of Materials Research **21**(4): 1041-1047.

Wales, D. J. (2001). "A microscopic basis for the global appearance of energy landscapes." Science **293**(5537): 2067-2070.

Wales, D. J. (2003). Energy landscapes, Cambridge University Press, Cambridge.

Wang, Q., J. Pelletier, et al. (2005). "Mechanical properties over the glass transition of $Zr_{41.2}Ti_{13.8}Cu_{12.5}Ni_{10}Be_{22.5}$ bulk metallic glass." Journal of Non-crystalline Solids **351**(27-29): 2224-2231.

Wang, W. (2005). "Elastic moduli and behaviors of metallic glasses." Journal of Non-crystalline Solids **351**(16): 1481-1485.

Wang, W. H. (2006). "Correlations between elastic moduli and properties in bulk metallic glasses." Journal of Applied Physics **99**: 093506.

Wang, W. H. (2011). "Correlation between relaxations and plastic deformation, and elastic model of flow in metallic glasses and glass-forming liquids." Journal of Applied Physics **110**: 053521.

Wang, X. and Q. Fang (2001). "Low-frequency internal friction study of oxide-ion conductor $La_2Mo_2O_9$." Journal of Physics: Condensed Matter **13**: 1641.

Wang, Y., J. Li, et al. (2007). "Ductile crystalline–amorphous nanolaminates." Proceedings of the National Academy of Sciences **104**(27): 11155-11160.

Waniuk, T., J. Schroers, et al. (2003). "Timescales of crystallization and viscous flow of the bulk glass-forming Zr-Ti-Ni-Cu-Be alloys." Physical Review B **67**(18): 184203.

Waniuk, T. A., J. Schroers, et al. (2001). "Critical cooling rate and thermal stability of Zr–Ti–Cu–Ni–Be alloys." Applied Physics Letters **78**: 1213.

Wright, W. J., T. Hufnagel, et al. (2003). "Free volume coalescence and void formation in shear bands in metallic glass." Journal of Applied Physics **93**:

1432.

Xi, X., D. Zhao, et al. (2005). "Fracture of brittle metallic glasses: brittleness or plasticity." Physical Review Letters **94**(12): 125510.

Xie, S. and E. P. George (2008). "Hardness and shear band evolution in bulk metallic glasses after plastic deformation and annealing." Acta Materialia **56**(18): 5202-5213.

Xu, D., B. Lohwongwatana, et al. (2004). "Bulk metallic glass formation in binary Cu-rich alloy series-$Cu_{100-x}Zr_x$ (x= 34, 36, 38.2, 40 at.%) and mechanical properties of bulk Cu64Zr36 glass." Acta Materialia **52**(9): 2621-2624.

Xu, Y. K., H. Ma, et al. (2005). "Mg-based bulk metallic glass composites with plasticity and gigapascal strength." Acta Materialia **53**(6): 1857-1866.

Yang, B., P. Liaw, et al. (2004). "In-situ thermographic observation of mechanical damage in bulk-metallic glasses during fatigue and tensile experiments." Intermetallics **12**(10-11): 1265-1274.

Yoo, B. G., K. W. Park, et al. (2009). "Role of free volume in strain softening of as-cast and annealed bulk metallic glass." Journal of Materials Research **24**(4): 1405-1416.

Yu, P., H. Bai, et al. (2007). "Pressure effects on mechanical properties of bulk metallic glass." Applied Physics Letters **90**(5): 051906.

Zhang, B., F. Q. Zu, et al. (2002). "Internal friction behaviours in $Zr_{57}Al_{10}Ni_{12.4}Cu_{15.6}Nb_5$ bulk metallic glass." Journal of Physics: Condensed Matter **14**: 7461.

Zhang, J., P. Fung, et al. (1995). "Dissipation function of the first-order phase transformation in solids via internal-friction measurements." Physical Review B **52**(1): 268-277.

Zhang, Q., H. Zhang, et al. (2003). "Bulk metallic glass formation of Cu–Zr–Ti–Sn alloys." Scripta Materialia **49**(4): 273-278.

Zhang, Y., W. Wang, et al. (2006). "Making metallic glasses plastic by control of residual stress." Nature Materials **5**(11): 857-860.

Zhang, Z., H. Zhang, et al. (2005). "Effect of aspect ratio on the compressive deformation and fracture behaviour of Zr-based bulk metallic glass." Philosophical Magazine Letters **85**(10): 513-521.

Zheng, G. (2011). "Application of phase-field modeling to deformation of metallic glasses." Current Opinion in Solid State and Materials Science **15**(3):116-124

Zheng, G. and M. Li (2009). "Mesoscopic theory of shear banding and crack propagation in metallic glasses." Physical Review B **80**(10): 104201.

Zheng, G. and Y. Shen (2010). "Simulation of crack propagation in fiber-reinforced bulk metallic glasses." International Journal of Solids and Structures **47**(2): 320-329.

Zhou, F., X. Liao, et al. (2003). "Microstructural evolution during recovery and recrystallization of a nanocrystalline Al-Mg alloy prepared by cryogenic ball milling." Acta Materialia **51**(10): 2777-2791.

Zhu, A., G. Shiflet, et al. (2010). "Unified approach to atomic transport phenomena in metallic glasses from the bond deficiency perspective." Physical Review B

81(22): 224209.